Gravitational wave physics and astronomy in the nascent era

Makoto Arimoto[1], Hideki Asada[2], Michael L. Cherry[3], Michiko S. Fujii[4], Yasushi Fukazawa[5], Akira Harada[6], Kazuhiro Hayama[7], Takashi Hosokawa[8], Kunihito Ioka[9], Yoichi Itoh[10], Nobuyuki Kanda[11,12], Koji S. Kawabata[13], Kyohei Kawaguchi[6], Nobuyuki Kawai[14], Tsutomu Kobayashi[15], Kazunori Kohri[16], Yusuke Koshio[17,18], Kei Kotake[7], Jun Kumamoto[4], Masahiro N. Machida[19], Hideo Matsufuru[20], Tatehiro Mihara[21], Masaki Mori[13], Tomoki Morokuma[22], Shinji Mukohyama[9,18], Hiroyuki Nakano[23], Tatsuya Narikawa[6], Hitoshi Negoro[24], Atsushi Nishizawa[25], Takayuki Ohgami[26], Kazuyuki Omukai[27], Takanori Sakamoto[28], Shigeyuki Sako[21], Mahito Sasada[13], Yuichiro Sekiguchi[29], Motoko Serino[27], Jiro Soda[30], Satoshi Sugita[27], Kohsuke Sumiyoshi[31], Hajime Susa[25], Teruaki Suyama[13], Hirotaka Takahashi[32,33], Kazuya Takahashi[9], Tomoya Takiwaki[34], Takahiro Tanaka[8,9,*], Masaomi Tanaka[26], Ataru Tanikawa[35], Nozomu Tominaga[25,17], Nami Uchikata[6], Yousuke Utsumi[36], Mark R. Vagins[18], Kei Yamada[8], Michitoshi Yoshida[37]

[1]*Faculty of Mathematics and Physics, Institute of Science and Engineering, Kanazawa University, Kakuma, Kanazawa, Ishikawa 920-1192, Japan*
[2]*Graduate School of Science and Technology, Hirosaki University, Aomori 036-8561, Japan*
[3]*Department of Physics and Astronomy, Louisiana State University, 202 Nicholson Hall, Baton Rouge, Louisiana 70803, USA*
[4]*Department of Astronomy, Graduate School of Science, The University of Tokyo, 7-3-1 Hongo, Bunkyo-ku, Tokyo 113-0033, Japan*
[5]*Department of Physics, Hiroshima University, 1-3-1 Kagamiyama, Higashi-Hiroshima, Hiroshima 739-8526, Japan*
[6]*Institute for Cosmic Ray Research, The University of Tokyo, 5-1-5 Kashiwanoha, Kashiwa, Chiba 277-8582, Japan*
[7]*Department of Applied Physics, Research Institute of Explosive Stellar Phenomena, Fukuoka University, 8-19-1, Jonan, Nanakuma, Fukuoka 814-0180, Japan*
[8]*Graduate School of Science, Kyoto University, Kyoto 606-8502, Japan*
[9]*Center for Gravitational Physics, Yukawa Institute for Theoretical Physics, Kyoto University, 606-8502, Kyoto, Japan*
[10]*Nishi-harima Astronomical Observatory, Center for Astronomy, University of Hyogo, 407-2 Nishi-gaichi, Sayo, Hyogo 679-5313, Japan*
[11]*Department of Physics, Osaka City University, Osaka, Osaka, 558-8585, Japan*
[12]*Nambu Yoichiro Institute of Theoretical and Experimental Physics, Osaka City University, Osaka, Osaka, 558-8585, Japan*
[13]*Hiroshima Astrophysical Science Center, Hiroshima University, 1-3-1 Kagamiyama, Higashi-Hiroshima, Hiroshima 739-8526, Japan*
[14]*Department of Physics, Tokyo Institute of Technology, 2-12-1 Ookayama, Meguro-ku, Tokyo 152-8551, Japan*
[15]*Department of Physics, Rikkyo University, Toshima, Tokyo 171-8501, Japan*
[16]*KEK and Sokendai, 1-1 Oho, Tsukuba 305-0801, Japan*
[17]*Department of Physics, Okayama University, Okayama, Okayama 700-8530, Japan*
[18]*Kavli Institute for the Physics and Mathematics of the Universe (WPI), The University of Tokyo Institutes for Advanced Study, University of Tokyo, Kashiwa, Chiba 277-8583, Japan*
[19]*Department of Earth and Planetary Sciences, Faculty of Sciences, Kyushu University, Nishi, Fukuoka 819-0395, Japan*
[20]*High Energy Accelerator Research Organization (KEK), Oho 1-1, Tsukuba 305-0801, Japan*

[21]*MAXI team, Institute of Physical and Chemical Research (RIKEN), 2-1, Hirosawa, Wako, Saitama 351-0198, Japan*

[22]*Institute of Astronomy, Graduate School of Science, The University of Tokyo, 2-21-1, Osawa, Mitaka, Tokyo 181-0015, Japan*

[23]*Faculty of Law, Ryukoku University, 67 Fukakusa Tsukamoto-cho, Fushimi-ku, Kyoto 612-8577, Japan*

[24]*Department of Physics, Nihon University, 1-8 Kanda-Surugadai, Chiyoda-ku, Tokyo, 101-8308, Japan*

[25]*Research Center for the Early Universe (RESCEU), School of Science, The University of Tokyo, Tokyo 113-0033, Japan*

[26]*Department of Physics, Faculty of Science and Engineering, Konan University, 8-9-1 Okamoto, Kobe, Hyogo 658-8501, Japan*

[27]*Astronomical Institute, Graduate School of Science, Tohoku University, Aoba, Sendai 980-8578, Japan*

[28]*College of Science and Engineering, Department of Physics and Mathematics, Aoyama Gakuin University, 5-10-1 Fuchinobe, Chuo-ku, Sagamihara, Kanagawa 252-5258, Japan*

[29]*Department of Physics, Faculty of Science, Toho University, 2-2-1 Miyama, Funabashi, Chiba 274-8510, Japan*

[30]*Department of Physics, Kobe University, Kobe 657-8501, Japan*

[31]*National Institute of Technology, Numazu College, Ooka 3600, Numazu, Shizuoka 410-8501, Japan*

[32]*Research Center for Space Science, Advanced Research Laboratories, Tokyo City University, 8-15-1, Todoroki, Setagaya, Tokyo 158-0082, Japan*

[33]*Department of Information and Management Systems Engineering, Nagaoka University of Technology, Niigata 940-2188, Japan*

[34]*Division of Science, National Astronomical Observatory of Japan, 2-21-1, Osawa, Mitaka, Tokyo 181-8588, Japan*

[35]*Department of Earth Science and Astronomy, College of Arts and Sciences, The University of Tokyo, 3-8-1 Komaba, Meguro-ku, Tokyo 153-8902, Japan*

[36]*Kavli Institute for Particle Astrophysics and Cosmology, SLAC National Accelerator Laboratory, Stanford University, 2575 Sand Hill Road, Menlo Park, CA 94025, USA*

[37]*Subaru Telescope, National Astronomical Observatory of Japan, 650 North A'ohoku Place, Hilo, Hawaii 96720, USA*

*E-mail: tanaka@yukawa.kyoto-u.ac.jp

....
The detections of gravitational waves (GW) by the LIGO/Virgo collaborations provide various possibilities for both physics and astronomy. We are quite sure that GW observations will develop a lot, both in precision and in number, thanks to the continuous work on the improvement of detectors, including the expected new detector, KAGRA, and the planned detector, LIGO-India. On this occasion, we review the fundamental outcomes and prospects of gravitational wave physics and astronomy. We survey the development, focusing on representative sources of gravitational waves: binary black holes, binary neutron stars, and supernovae. We also summarize the role of gravitational wave observations as a probe of new physics.
....

Subject Index   E02, E30, F33

Contents   PAGE

1. Introduction

1.1. *Gravitational waves from binary black holes*

The first gravitational wave (GW) event from a binary black hole (BBH), GW150914, discovered by the LIGO/Virgo collaboration, brought us many surprises [1]. Regarding binary neutron star (BNS) coalescences, it was believed that there was little uncertainty in estimating their event rate compared with the case of BBHs. Even for BNS coalescences, the uncertainty in the estimated event rate was expected to be about one order of magnitude. On the other hand, although it is conceivable that BBHs should exist in our universe, the estimation of the GW event rate had no observational support, different from the case of BNSs. Hence, BBHs were not considered to be a promising GW source. It was somewhat surprising that such a system was the first directly detected GW source. However, it was even more surprising that those black holes (BHs) were heavier than many people expected: each component BH has a mass about $30\,M_{\odot}$. The masses of BH candidates found so far by electromagnetic observations is estimated to be at most about $20\,M_{\odot}$ [2]. Although there were some candidate objects that did not contradict having heavier masses within the observational error, there is no object that can be said to be about $30\,M_{\odot}$. The observation of GWs has changed our understanding of the mass distribution of BHs in the universe [3,4]. Since then, the number of BBH observations officially announced by the LIGO/Virgo collaborations has been increasing (see Table 1) [5]. Not all of them are massive BHs, but the observations that have followed indicate that the first GW event, GW150914, was not so special.

As a result of this discovery, how those BBHs detected by GWs were formed in the history of the universe has become one of the great mysteries of astrophysics. A variety of BBH formation scenarios have been proposed [6]. The most promising candidate for the formation channel would be binary interaction between heavy-star binaries formed from gases with a low metallicity. Even for this leading scenario there are various uncertainties: the binary formation rate from the gas cloud, stellar evolution including mass-loss processes, binary interaction to form close binaries, formation process of BHs, and so on. Binary evolution can be so complex, changing its orbital radii and eccentricity. Therefore, it is a theoretical challenge to predict the distributions of BH masses, orbital separation, and eccentricity at the formation of a BH binary to compare with observations.

Table 1. Observing terms of LIGO/Virgo detectors. Detectors: H1 at Hanford, Washington; L1 at Livingston, Louisiana; V1 at Cascina, Italy.

	Observation period	Detectors	Events reported
O1	Sep 2015 to Jan 2016	H1, L1	3 BBHs
O2	Nov 2016 to Sep 2017	H1, L1	3 BBHs
O2	Aug 2017	H1, L1, V1	4 BBHs, 1 BNS
O3a	Apr 2019 to Sep 2019	H1, L1, V1	many BBHs, 1 BNS
O3b	Nov 2019 to Apr 2020	H1, L1, V1	N/A

As alternative scenarios, we can think of the formation of BH binaries in star clusters [7] and their formation in the primordial universe [8]. Many variants of these scenarios can be thought of. In the future, as the details of the theoretical model become better understood, and as GW observations accumulate information about the event rate, the mass and distance distributions, the distribution of BH spins, and so on, we will be able to identify the contributions from respective formation channels of BBHs.

1.2. Gravitational waves from binary neutron stars

The first GW event from a BNS merger, GW170817, observed on August 17, 2017, marked a splendid opening for GW astronomy [9]. BNS coalescence was counted as a guaranteed GW source. The discovery was followed by simultaneous observation of gamma-ray bursts, identification of the electromagnetic counterpart by optical and infrared telescopes [10], long-term follow-up observations by radio waves and X-rays, and detection of apparent superluminal motion [11,12]. How BNS coalescence proceeds was revealed to be something close to what was theoretically predicted. In the study of BNS coalescence, weak gravity approximation is no longer appropriate. Hence, numerical relativity is an indispensable research tool, with knowledge of the equation of state for high-density nuclear matter. At the same time, various radiation fields, photons and neutrinos, originating from high-density matter must be solved, and magnetic fields can also play an important role in the simulations. Therefore, combining various techniques for numerical simulation is required. In the case of GW170817, from its optical and infrared light curves it is thought that the ejecta mass was about $0.05\,M_\odot$ and part of it possessed high neutron excess, resulting in the production of a significant amount of r-process elements. The amounts of r-process elements produced may be sufficient to explain almost all such elements in the universe. In addition, numerical simulations show that the merged binary becomes a massive neutron star (NS) supported by rotation, and the material stripped around it forms a disk. The simultaneous (1.7 s after the coalescence time) observation of a short gamma-ray burst (SGRB) indicates the connection between SGRBs and BNS coalescence. Although the observed SGRB was extraordinarily weak, this can be understood because the SGRB jet was not pointing along our line of sight [13,14]. This interpretation gained strong support because apparent superluminal motion was observed by radio waves [11,12]. The detection of apparent superluminal motion is also strong evidence for a relativistic jet having been launched. In addition, the GW observations of this event also provided restrictions on the equation of state of dense nuclear matter, mostly from the constraint on the tidal deformability of the NSs just before the coalescence [9]. Here again, numerical relativity techniques played an important role. It is also an important theoretical challenge to derive the equation of state that can be compared with phenomena from first principles of quantum chromodynamics. High-energy gamma-rays, neutrinos, and cosmic rays were not detected in GW170817 [15–18], although BNS mergers and SGRBs are considered to be sources of these particles [19–22]. We do not discuss these multi-messenger signals further in this review.

1.3. Gravitational waves from supernovae

Although GWs from supernovae have not yet been detected, they are important targets of gravitational wave observations. After more than half a century of continuing efforts, ever since the seminal work by Colgate and White [23], theory and neutrino radiation-hydrodynamics simulations of core-collapse supernovae (CCSNe) are now converging to a point that multi-dimensional (multi-D) hydrodynamics instabilities play a key role in the neutrino mechanism [24], the scenario most favored to trigger explosions. In fact, self-consistent simulations in three spatial dimensions (3D) now report shock

revival of the stalled bounce shock into explosion by the multi-D neutrino mechanism (see Refs. [25–28] for reviews).

From observational point of view, mounting evidence from multi-wavelength electromagnetic (EM) wave observations (such as blast/ejecta morphologies, line profiles, polarizations) are pointing toward CCSNe being generally aspherical (e.g., Refs. [29,30] and references therein). Nevertheless, these EM signals are secondary as a probe into supernova inner workings, providing information only after a shock break-out from the massive stars. On the other hand, GWs from CCSNe are direct observables, which imprint live information of the central engine. Furthermore, coincident detection of CCSN neutrinos with GWs is important not only for significantly enhancing the detectability of the GWs (e.g., Ref. [31]), but also for unraveling the hydrodynamics evolution from the onset of core collapse toward the formation of compact objects (neutron stars and black holes; see Ref. [32] for a review). Current estimates of CCSN rates in the Milky Way predict one event every $\sim 40 \pm 10$ yr [33]. While rare, they provide a unique opportunity to study CCSNe using a full set of multi-messenger observables including GWs, neutrinos, and nuclear gamma-rays [34].

1.4.   Test of general relativity

The direct detection of GWs has opened a new window for tests of general relativity (GR). In order to detect GW signals, we need theoretical predictions of the GW waveform in advance. In the more complex theory of gravitation that extends GR, theoretically predicting the waveform is more difficult. Our current knowledge of the waveform in modified gravity is limited, but some possible deviations in the waveform from GR have been predicted. GW observations so far have not suggested any deviation from GR [35]. However, the lack of deviation itself can have important physical meaning. Besides constraints on the deviation in the waveform, an important constraint was also derived from the speed of propagation of GWs, i.e., from the detection of a short gamma-ray burst associated with the GW170817 event at a distance of about 40 Mpc. The fractional deviation of the propagation speed of GWs from that of light is less than $\sim 10^{-15}$ [36], which excludes various possible extensions of GR [37,38,40–43].

GWs from binaries can be used as the standard siren [44], providing an alternative method for measuring the cosmic expansion history. GW170817 has already given us an estimate of the Hubble constant [45,46]; we do not discuss any further the aspects of testing cosmological models using GWs in this review.

1.5.   Organization of this article

In this review paper we give an overview of the vast area of newly developing gravitational wave physics and astronomy mentioned above. The paper is organized as follows. In Sects. 2, 3, and 4 we focus on three major sources of gravitational waves: BBHs, BNSs, and SNe. We discuss various topics arising from the detection of gravitational waves, including the future prospects. In Sect. 5 we focus more the new physics examined by using GWs as a probe, including the testing of gravity and the implications for dark matter physics. Section 6 is devoted to a short conclusion.

2.   Binary black holes

2.1.   Gravitational waves from binary black holes

LIGO/Virgo have reported GWs from BBH mergers as a result of the O1 and O2 observing runs [5] in what is called the "Gravitational-Wave Transient Catalog," GWTC-1. The best fit parameters for these binaries are listed in Table 2. We have large errors in the parameter estimation, especially for

Table 2. BBH merger events observed during LIGO/Virgo O1 and O2. We show only the median values for the individual masses m_1 and m_2, chirp mass $\mathcal{M}$, effective spin χ_{eff}, final BH mass M_{fi}, and its angular momentum parameter a_{fi}. These numbers are in the source frame. The estimated distance in Mpc and the redshift z are also shown. The 90% credible intervals were reported in Table III of Ref. [5].

Event	$m_1/M_\odot$	$m_2/M_\odot$	$\mathcal{M}/M_\odot$	χ_{eff}	$M_{\text{fi}}/M_\odot$	a_{fi}	Distance (Mpc,z)
GW150914	35.6	30.6	28.6	−0.01	63.1	0.69	430, 0.09
GW151012	23.2	13.6	15.2	0.05	35.7	0.67	1060, 0.20
GW151226	13.7	7.7	8.9	0.18	20.5	0.74	440, 0.09
GW170104	30.8	20.0	21.4	−0.04	49.1	0.66	960, 0.19
GW170608	11.0	7.6	7.9	0.03	17.8	0.69	320, 0.07
GW170729	50.2	34.0	35.4	0.37	80.3	0.81	2750, 0.48
GW170809	35.0	23.8	24.9	0.08	56.4	0.70	990, 0.20
GW170814	30.6	25.2	24.1	0.07	53.4	0.72	580, 0.12
GW170818	35.4	26.7	26.5	−0.09	59.8	0.67	1020, 0.20
GW170823	39.5	29.0	29.2	0.09	65.6	0.71	1850, 0.34

the individual masses and the effective spin parameter, because the signal-to-noise ratios (SNRs) are not very high. There are results reported by alternative searches. One of them reports other candidate GW events [47].

The mass and spin distributions obtained are summarized in Fig. 1. The chirp mass is defined by

$$\mathcal{M} = \mu^{3/5} M^{2/5}, \tag{1}$$

with $M = m_1 + m_2$ and $\mu = m_1 m_2/M$, where m_1 and m_2 are the component masses. The effective spin parameter is defined by

$$\chi_{\text{eff}} = \frac{1}{M} \left(\frac{\boldsymbol{S}_1}{m_1} + \frac{\boldsymbol{S}_2}{m_2} \right) \cdot \hat{\boldsymbol{L}}, \tag{2}$$

where $\boldsymbol{S}_1$ and $\boldsymbol{S}_2$ are the spin angular momentum vectors of the respective bodies and $\hat{\boldsymbol{L}}$ is the unit vector pointing at the direction of the orbital angular momentum of the binary.

The event rate reported by the LIGO/Virgo Collaborations ranges from 9.7 to 101 Gpc^{-3} yr^{-1} for BBH mergers. The masses of the observed BHs are relatively large compared with the stellar-mass BH candidates found by X-ray observations (see, e.g., Ref. [2] and references therein). The origin of BBHs is an important new issue of debate raised by the GW observations. A promising formation path is through the stellar evolution of low-metallicity stars, which is the main topic of Sect. 2.2. There are various formation channels, and the main focus is whether or not the stellar dynamics in the star cluster plays a crucial role. An alternative is the formation of BH binaries in the early universe, which is the so-called primordial BH scenario. The formation process of primordial BH binaries is discussed in Sect. 5.2.

2.2. Theoretical study of binary black hole formation

Mergers of BBHs are the dominant sources of gravitational waves. Currently, two evolutionary pathways are envisaged as origins of BBHs. First is the so-called in situ BBH formation scenario, where massive star binaries are formed and each member star becomes a BH after stellar evolution. Second is the so-called ex situ scenario, where single stars formed in a dense star cluster become BHs
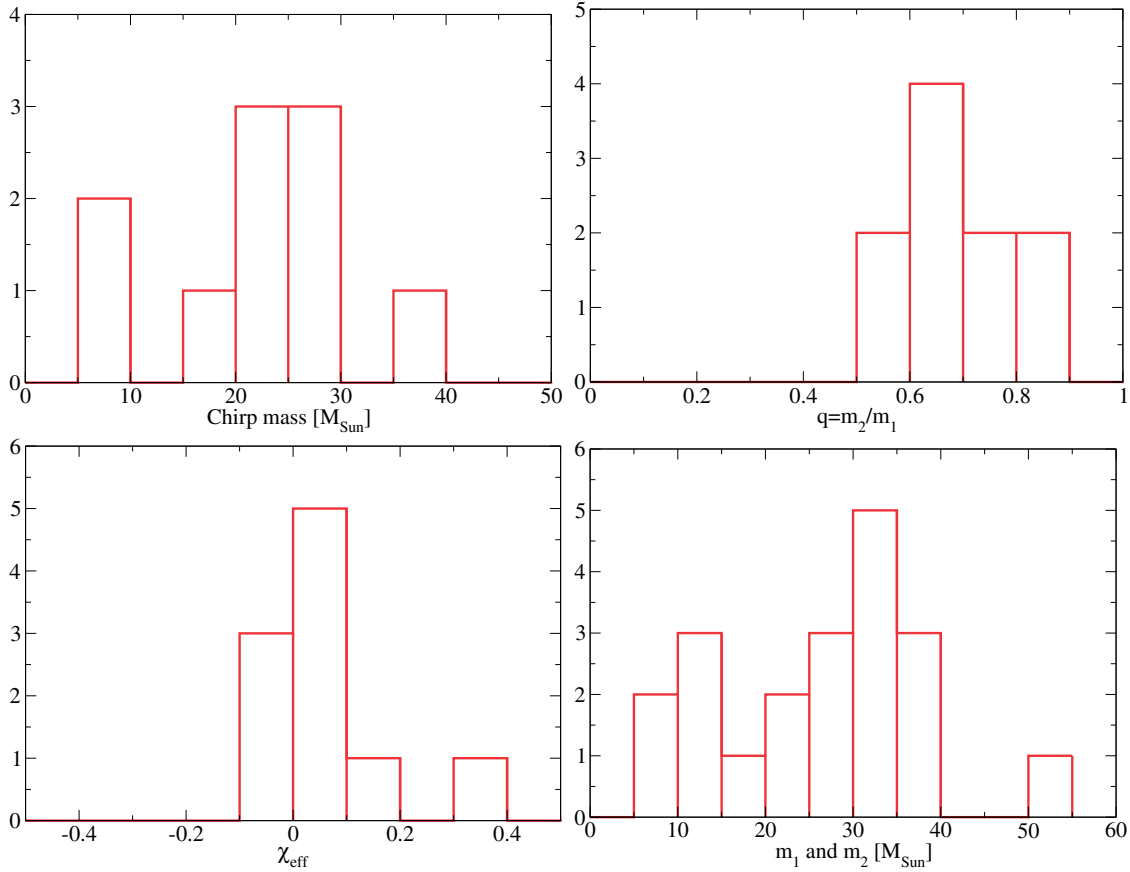
Fig. 1. Distribution of the median values of the chirp mass $\mathcal{M}$, mass ratio $q = m_2/m_1$, effective spin χ_{eff}, and individual masses of BBHs (which are redundant, though) observed during LIGO/Virgo O1 and O2. It should be noted that there are large errors in the current observations. Even for the chirp mass, which is the most sensitive parameter in the GW waveform of BBH mergers, the 90% credible interval gives $\lesssim$20% difference in the estimation.

after stellar evolution, and those BHs become binaries as a result of dynamical interaction. Here, we describe our current understanding of each of these scenarios.

2.2.1. Formation of isolated stellar binaries

Binary star formation at low metallicities   While massive stellar binaries are possible astrophysical progenitors of BH–BH binaries that finally merge, their formation process is still uncertain. In particular, a major focus is put on the formation of such systems at low metallicities, $Z \lesssim 0.1 \, Z_\odot$, which are required to yield massive ($\simeq$ a few $\times 10 \, M_\odot$) BHs avoiding significant mass loss during stellar evolution. Observations suggest that a large fraction of massive stars are born in binaries in the solar neighborhood. Some of them are in very tight systems with separations of only $\lesssim 0.1$ au, and are possible candidates that finally evolve into BH binaries that merge within the Hubble time. On the other hand, since the delay time until the BBH merger is potentially as long as the Hubble timescale, depending on the initial separation, some of the progenitor stars may have been born in the early universe. Therefore, our goal is to elucidate the formation process of massive and tight binary stars in a variety of low-metallicity environments, including the local and early universe.

A straightforward method which ultimately leads us to the goal is to directly follow the evolution with numerical simulations. One of the key processes is the gas gravitational fragmentation that
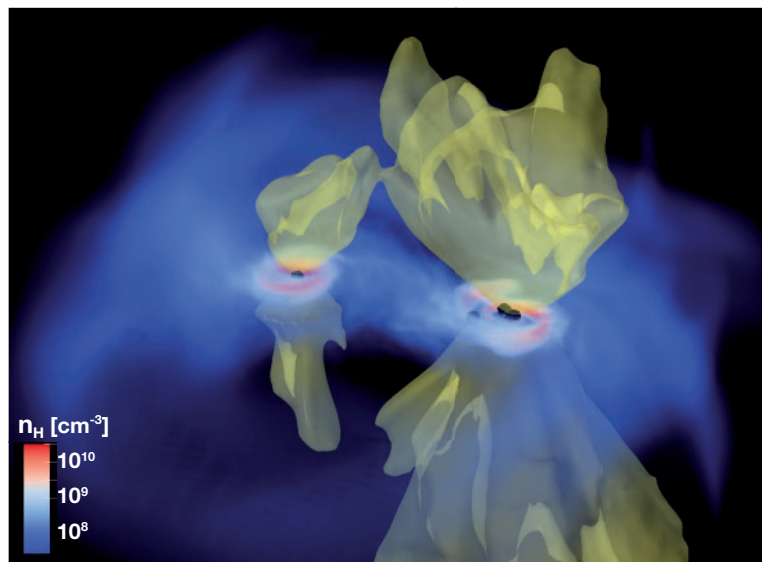
Fig. 2. An example of the latest 3D radiation-hydrodynamics simulations of primordial star formation, in which the metallicity is exactly zero [48], showing a snapshot at the epoch when massive protostars in a binary system accrete gas under radiative feedback. Presented are the volume-rendered 3D distribution of the mass density, together with ionization fronts (yellow surfaces) and protostars (black dots).

potentially leads to multiple stars, some of which form binaries. Magnetic fields, if any, should be important because they transfer the angular momentum of the gas, affecting the orbital evolution of newly forming binaries. Stellar radiative feedback is also critical to determining how massive binaries finally appear, halting mass accretion onto the stars [49–51]. We consequently need to solve the interplay between gas dynamics, magnetic fields, and radiative fields in full 3D, spatially resolving a very wide dynamic range. Ultimately, integrating the evolution over $\sim$Myr is required to cover the whole evolution of the star formation process. Although this is still challenging, recent studies are advancing to incorporate the above processes as much as possible with limited computational resources.

For instance, Fig. 2 shows a snapshot of our recent 3D radiation hydrodynamic simulations using the adaptive mesh refinement code SFUMATO [48]. In this particular case, we follow the long-term ($\sim$0.1 Myr) evolution in the protostellar accretion stage of primordial star formation. We see a multiple stellar system including a massive binary system that has appeared after the disk fragmentation in the earlier stage. The double bipolar H II regions are growing from the two massive stars that are still accreting the surrounding gas under the radiative feedback. Although this provides a glimpse of binary formation in the early universe, the newborn binary has a large separation: the two massive stars exciting the bipolar H II regions are separated by more than 10^3 au. The formation process of massive and tight binaries, some of which should evolve into gravitational wave sources, is yet to be revealed. Obviously, further studies and simulations are necessary to explain how such systems are formed. We describe our recent studies and future prospects in what follows.

Role of magnetic fields in close binary formation   Observations of nearby star-forming regions indicate that a large fraction of stars are members of binary systems [52], and the binary frequency is even higher for high-mass stars than for low-mass ones [53]. Theoretically, numerical simulations have shown that a binary stellar system forms as a result of fragmentation of a molecular cloud core
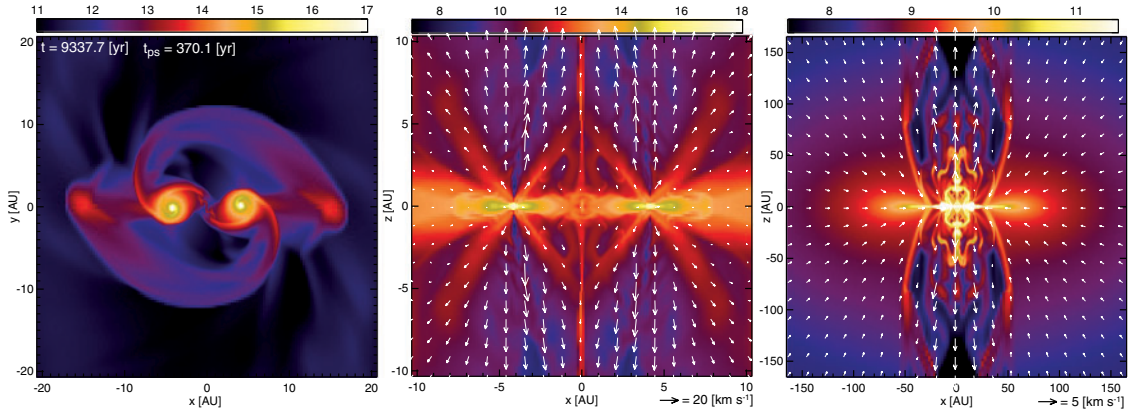
Fig. 3. Proto-binary formation in MHD simulation. Shown are density (color) and velocity (arrows; middle and right panels) distributions on the $z = 0$ (left) and $y = 0$ (middle and right) planes at three different spatial scales. The elapsed time after the onset of the prestellar cloud, t, and that after protostar formation, t_{ps}, are described in the left panel.

during gravitational collapse [54]. In rapidly rotating and gravitationally unstable cores, fragmentation occurs more easily [55,56] and the accretion rate is higher after the protostars are formed. The rotation velocity increases, and the cloud becomes disk-like during the collapse owing to angular momentum conservation. This promotes fragmentation and subsequent binary formation.

According to numerical simulations, the binary separation continues to increase with time as a parcel of gas with larger angular momentum falls onto the central region or proto-binary system at later times [54,57], and the outcome is a wide binary system with a separation typically $\gg 100$ au. In contrast, observationally high-mass stars tend to be in close binary systems with separation 1–10 au [52]. This discrepancy between theory and observation can be circumvented if we take non-ideal magnetohydrodynamics (MHD) effects into account.

Recent non-ideal MHD simulations for present-day star formation showed that the excess angular momentum is transported from the proto-binary system by magnetic braking and by outflow launching; as a consequence, the close binary system can be formed in a highly unstable magnetized cloud. Figure 3 is a snapshot of a proto-binary system in an example of such a simulation (Y. Saiki and M. N. Machida, Astrophys. J. Lett., submitted). In the figure, we can see that a powerful jet is driven by each of the protostars. The separation of the binary system is about 10 au at this epoch. On the equatorial plane, both circumstellar and circumbinary disks can be confirmed (the left panel of Fig. 3). Two cavity-like structures created by the jets are seen in the middle panel of Fig. 3. The velocities of the jets driven by the protostars exceed $100\,\text{km}\,\text{s}^{-1}$. Those high-velocity components are enclosed by the low-velocity outflow of $\sim 10\,\text{km}\,\text{s}^{-1}$ driven by the circumbinary disk. The angular momentum of the binary system is extracted from the system both by the large-scale wide-angle outflows and small-scale collimated jets. The binary jet/outflow structure is also reported from recent ALMA observations [58].

Stellar system formed from metal-free gas   Next, we see the nature of theh first stellar systems formed from the primordial gas and discuss the possible formation of the first star binaries. The collapse of a slightly gravitationally unstable gas cloud ($n_{\text{H}} = 1.4 \times 10^4\,\text{cm}^{-3}$ and $T = 200\,\text{K}$) is simulated by smoothed-particle hydrodynamics. Armed with an elaborate sink particle creation scheme and using the barotropic equation of state precalculated by a one-zone model, we succeeded
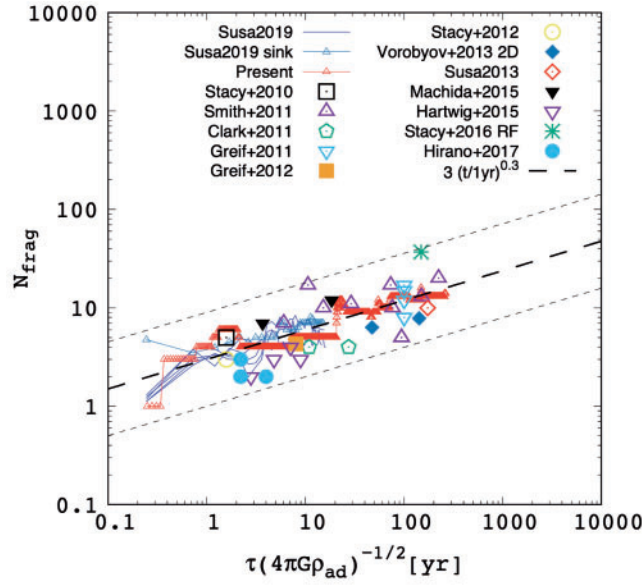
Fig. 4. Number of fragments in a first star-forming cloud as function of the scaled time. We assume ρ_{ad} is 2×10^{-5} (g cm^{-3}), above which the gas behaves adiabatically. The red line with small triangles denotes the present result, and the thin lines correspond to our previous result [59]. Results in the literature [60–70] are also shown.

in extending the time integration up to 25 000 yr in the accretion phase, ~17 times longer than the previous calculation [59].

Figure 4 shows the number of fragments, i.e. sinks, as functions of the scaled time normalized by the free-fall time at the density $n_{th} = 10^{15}\,\text{cm}^{-3}$, above which the temperature rises adiabatically. The results can be scaled using the scaled time according to the scale-free nature of gravity [59]. Note that the integration time of the present simulation is also the longest so far in terms of the scaled time. We can see a simple trend that the number of fragments is proportional to the elapsed time after the central density exceeds n_{th}. This trend was known previously [59], but we now confirm that the relation holds even after a 10 times longer integration time, although the simulation was only performed for one particular realization. This result is also generally consistent with results of other simulations in the literature.

Several systems of binaries are identified in this cluster. Figure 5 shows the time evolution of their separations. The different colors correspond to different pairs of binaries. The members of the binaries easily change as a result of close encounters/mergers with other stars. The thick red curve at the top of the panel shows the typical size of this cluster, which grows in proportion to the elapsed time after the first protostar formation, as predicted by the conservation of angular momentum and the gas distribution at the end of the collapse phase. On the other hand, the binary separations also grow when the binary systems acquire angular momentum as a result of gas accretion, which is, however, counterbalanced by the effect of encounters with other stars that make the binary tighter. Hence, the separations are kept rather constant during the computation. The separations observed in this particular run are around a few 10s of au, which is too wide to end up with BBHs that coalesce within the Hubble time. In the present simulation, however, we adopt a lower threshold density than the true adiabatic density for computational reasons, and the actual binary separation should be scaled from our nominal value. After the scaling, the time should be 100 times shorter and the separation ~70 times less. Thus, our binary separation corresponds to a few times 0.1 au after scaling, although
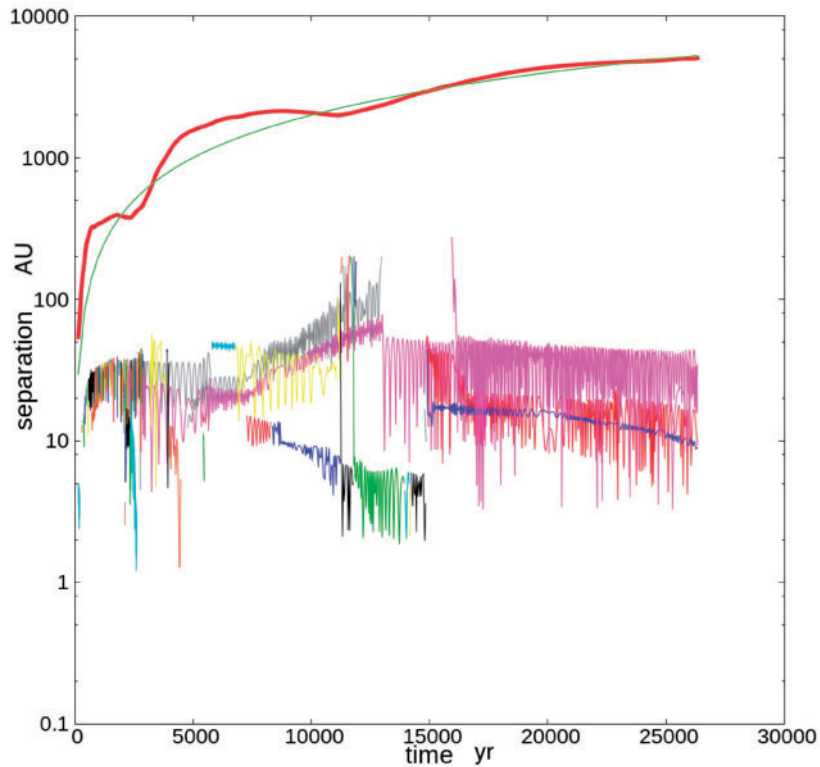
Fig. 5. The separations of binaries identified in the present simulation as functions of time. Different colors denote different binaries. The thick red solid curve shows the mean square average of the distance between the stars and the center of mass of the stellar system, while the thin green curve shows the distance in proportion to the elapsed time since the first sink formation.

the integrated time is only 250 yr. If this separation is kept constant for another ∼5000 yr when the surrounding gas is swept away by the radiative feedback, these binaries could be progenitors of the merging BBHs observed in gravitational waves.

To draw firm conclusions about the nature of the stellar systems formed, we need to extend the numerical simulation in time until the radiative feedback from the protostar terminates the accretion to the system at several thousand years after the formation of the first protostar. We should also consider the effects of turbulence and magnetic fields. In fact, the presence of a coherent magnetic field in the primordial environment induces a strong magnetic braking effect [71], leading to less fragmentation in the accretion disk. Also, recent simulations predict more fragmentation in cases with strong turbulence. These are issues to be addressed in the future.

2.2.2.   Binary black hole formation by dynamical interactions in dense star clusters
Binary black holes formed in star clusters   Dense star clusters are one of the promising formation sites of BBHs. In particular, globular clusters (GCs) are expected to be a source of BBHs merging within the Hubble time. Most current studies on BBH formation in GCs use the Monte Carlo method [7,72] and suggest a local merger rate density of ∼5 Gpc^{-3} yr^{-1} [72,73]. They also predict that BBHs formed in GCs have several distinct features from those formed under isolated environments. The GC-originated BBHs have more isotropic spin–orbit misalignment angles [74]. Some of those BBHs may contain massive (∼100 $M_\odot$) BHs in the so-called "pair-instability mass gap" [75], or may have finite eccentricities at a GW frequency of ∼10 Hz [76,77]. Such Monte Carlo simulations, however,

need careful calibration of some parameters from comparison with N-body results [78,79]. On the other hand, direct N-body simulations with a realistic number of particles (i.e. $N \sim 10^6$) are still numerically too expensive with a cost of N^2 and with a very small binary orbital period compared with the GC lifetime. As a result, there is currently only a single example of million-body runs, performed using a GPU cluster [80], although the situation may change in the near future through adoption of tree-direct hybrid methods [81,82] and novel schemes for binary integration [83].

On the other hand, open clusters (OCs) have not been expected to produce such tight BBHs because they are less massive and less dense compared with GCs. From the mass function of star clusters, however, there are a hundred times more OCs than GCs. Therefore, we thought it might be interesting to examine seriously the formation rate of BBHs in OCs.

We performed a series of N-body simulations of OCs using the direct N-body code NBODY6++GPU, which includes both stellar and binary evolution models [84]. As an initial condition, we adopted the Plummer model [85] with a total mass of $2.5 \times 10^3 \, M_\odot$ with 0.1 solar metallicity. We calculated 360 realizations per a given set of the parameters and obtained $\sim$1 BBH per cluster on average. The merger time of the BBHs due to gravitational wave emission is given as a function of the semi-major axis (a) and eccentricity (e) of BBHs [86]. In Fig. 6, the distributions of a and e of BBHs formed in the simulations are shown. We can see that most of the BBHs are distributed in the red-colored region (Region 3), corresponding to those dynamically formed, and the characteristic value of their semi-major axis is set by the condition that the potential depth of binaries is of the order of that of the cluster. Owing to the shallow potential depth of OCs, their separation is too large for BBHs to merge within the Hubble time. On the other hand, we found some BBHs that can merge within the Hubble time in the blue-colored region (Region 1), in which the BBHs have very low eccentricity and small semi-major axis. These are formed via binary stellar evolution such as stable and unstable mass transfer. Some of them experience a dynamical encounter after the binary stellar evolution and have large eccentricity (yellow-colored, Region 2). The three formation channels above are summarized in Fig. 6.

In a GC, more BBHs are dynamically formed and, owing to the deeper potential well, they tend to have a smaller semi-major axis and some of them merge within the Hubble time. On the other hand, in open clusters, the major channel for BBH mergers is different: a binary consisting of two massive main-sequence (MS) stars forms first and becomes tight as a result of the binary stellar evolution. If this separation is kept until BBHs are formed after the stellar lifetime, they can merge within the Hubble time.

From our results, we can estimate the merger rate of BBHs formed in OCs 10 Gyr ago to be 0.3 yr^{-1} Gpc^{-3} [87]. This value corresponds to 20%–50% of those formed in GCs [73]. This means that BBHs formed in OCs contribute to GW events much more than previously expected.

We also repeated similar simulations but with different metallicities, ranging from zero to one solar metallicity. Using the BBH formation rate and distribution of their orbital parameters, and assuming cosmic metallicity evolution with some dispersion [88] and a cosmic star formation rate density [89], we can estimate the merger rate of BBHs formed in OCs in the present universe by summing the contributions from all OCs. The estimated event rate is $\sim$70 yr^{-1} Gpc^{-3} [90], comparable to that estimated from LIGO/Virgo O2 and O3, $64.0^{+73.5}_{-33.0}$ yr^{-1} Gpc^{-3} [91].

Our simulations also give a prediction of the BH–MS binary distribution observable with Gaia [92]. In the next data release of Gaia (Gaia DR3), binaries will be included. Using the results of our simulations, we estimated that $\sim$10 BH–MS binaries would be detectable with Gaia [93], even if we assume relatively stringent observational constraints [94]. In contrast to BH–MS binaries formed in
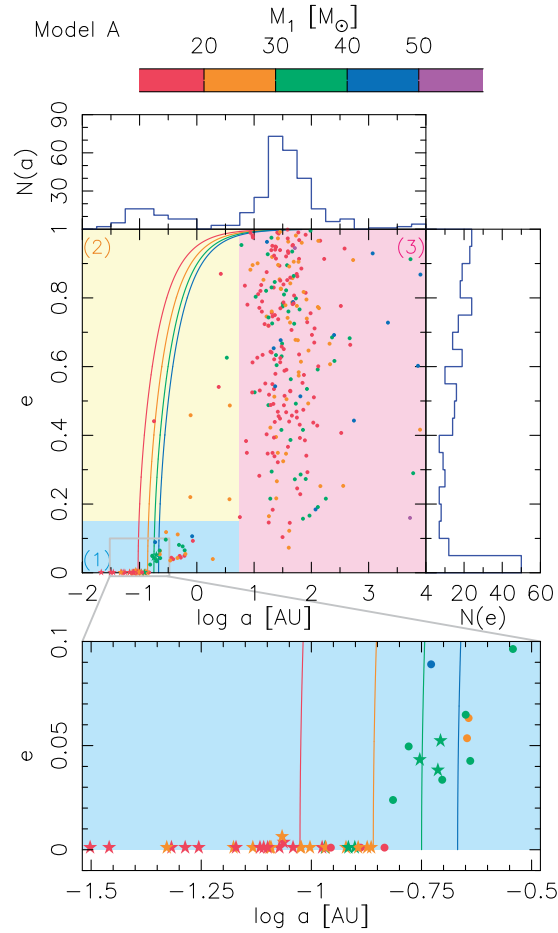
Fig. 6. Semi-major axis (*a*) and eccentricity (*e*) distribution of BBHs obtained from our simulations (from Fig. 1 of [87]). The star symbols show BBHs with a merger time less than 10 Gyr. The colors of the symbols indicate the primary mass (M_1) of the BBHs. The colored background indicates classification depending on the formation mechanisms illustrated in Fig. 7. The colored curves show the relation between *a* and *e* to give $t_{GW} = 10$ Gyr for BBHs with masses of 15, 25, 35, and 45 $M_\odot$ (red, yellow, green, and blue).

galactic fields, those formed in OCs would have a smaller mass for the MS companion ($< 5 M_\odot$), a longer orbital period (> 1 yr), and a higher eccentricity (> 0.1).

Binary population synthesis model for extremely low-metallicity stars   Binary population synthesis (BPS) is a powerful tool for predicting merger rates of BBHs formed in galactic fields (see, e.g., Ref. [95]). Coupled with star cluster simulations, BPS can also predict the merger rate of BBHs formed in dense stellar clusters (see, e.g., Ref. [73]). So far, most studies have focused only on BBHs formed under Pop I and II environments ($0.01 \lesssim Z/Z_\odot \lesssim 1$). On the other hand, it has been suggested that Pop III-originated BBHs have features distinct from Pop I/II-originated BBHs [96]. Thus, it is important to bridge the metallicity gap (i.e. $0 < Z/Z_\odot \lesssim 0.01$) in order to elucidate the origins of merging BBHs. Hereafter, we call stars in this metallicity gap "extreme metal-poor" (EMP) stars. In order to bridge the metallicity gap, we have made a table of the evolutionary tracks of stars with $-8 \leq \log(Z/Z_\odot) \leq -2$. Note that there has been no evolution track computation for EMP stars before. We compiled these evolutionary tracks as a set of fitting formulae, and incorporated them into BSE and NBODY6 (Refs. [97,98], respectively). The BSE code is based on several BPS
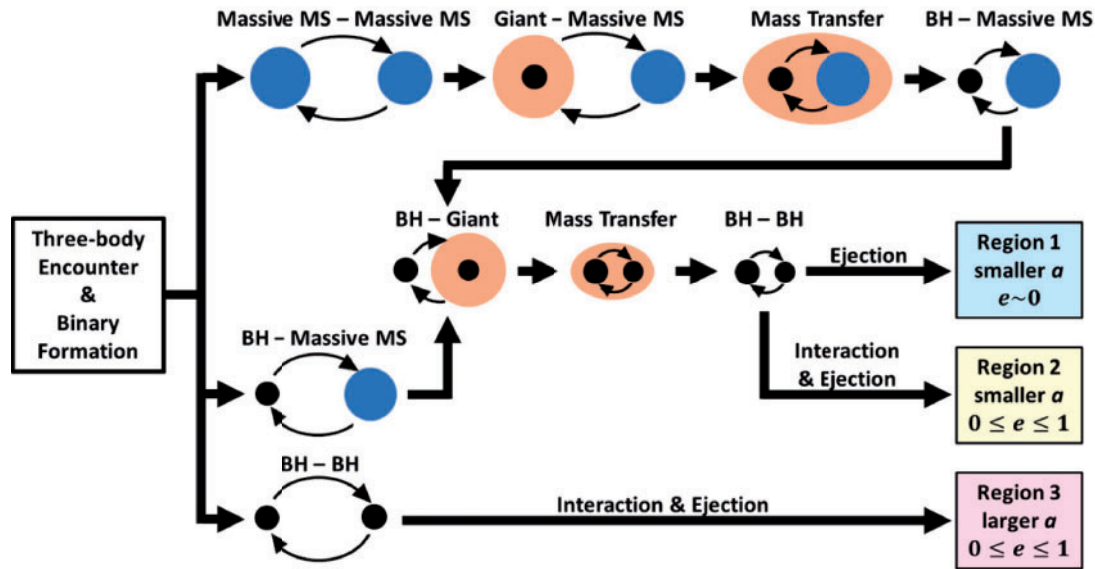
Fig. 7. Schematic figure of the formation processes of three different types of BBHs. (From Fig. 3 of Ref. [87].)

calculations (see, e.g., Refs. [95,96]), and the `NBODY6` code and its derivatives are widely used for obtaining BBH merger rates in dense star clusters [87,99–104]. Here, we describe these fitting formulae briefly (see Ref. [105] for details).

We first make stellar evolution models as a reference for fitting formulae by means of one-dimensional (1D) simulation, for which we use the `HOSHI` code [106–109]. We follow the time evolution of stars with $8 \leq M/M_\odot \leq 160$ for $-8 \leq \log(Z/Z_\odot) \leq -2$. We start the calculation from zero-age main-sequence (ZAMS) and stop at the carbon-ignition time. We do not include stellar wind mass loss. We take into account the post-carbon-ignition evolution (e.g. supernova) and stellar wind mass loss as post-processing. This is the same as in the `BSE` and `NBODY6` codes incorporating the evolution of Pop I/II stars. The evolution of EMP stars differs from that of Pop I/II in the following respects: neither the Hertzsprung-gap (HG) nor the blue-loop phase exists, and the envelope of massive ($M \sim 20 M_\odot$) stars remains radiative until the ends of their lives. This has a significant impact on binary evolution, such as the mass accretion rate in the Roche-lobe overflow phase, and the occurrence of post-MS mergers and common envelope evolution.

We use the above stellar evolution models as a reference, and make a fitting formula for EMP stars. Figure 8 shows stellar evolution on the Hertzsprung–Russell diagram in the cases of $\log(Z/Z_\odot) = -5$ and -8 for comparison with the results obtained from 1D calculations and the fitting formulae. Note that the stellar evolution in this figure is terminated at the carbon-ignition time, and stellar wind mass loss is not taken into account. The tracks by fitting formulae show good agreement with those by 1D calculations, with the maximum deviation less than 20%. This error is satisfactory for BPS and star cluster simulations coupled with BPS, considering the large uncertainties coming from uncertainties in tidal interaction, common envelope evolution, stellar wind mass loss, natal kicks of neutron stars and black holes, supernova mass loss including pair instability, pulsational pair instability supernovae, and so on.

2.2.3. Outlook
To distinguish the possible formation channels described above, we need further statistical constraints with increasing numbers of BBHs identified by GW detections. For instance, binary population synthesis models predict that Pop III progenitor stars provide characteristic features in the resulting
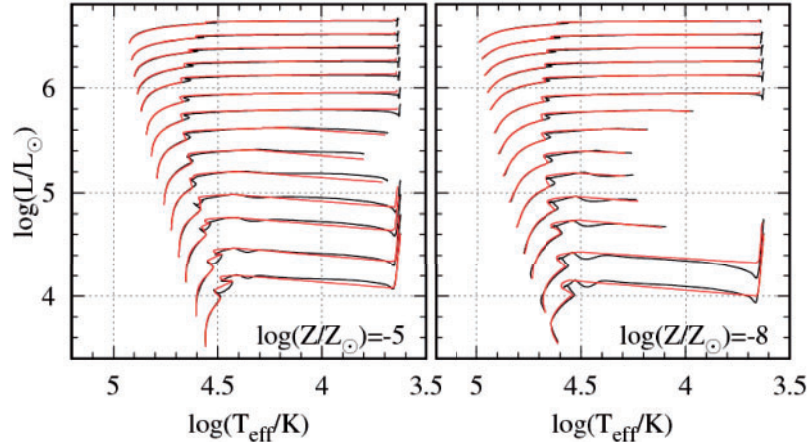
Fig. 8. Hertzsprung–Russell diagram for comparison between stellar evolution models (black) and fitting formulae (red). The stellar evolution in this figure ends at the carbon-ignition time, and stellar wind mass loss is not taken into account.

chirp-mass distributions. A most prominent feature is a peak around $30\,M_\odot$ [96], which may still be consistent with the latest LIGO/Virgo O3a results. Future GW observations will impose more constraints on other properties of BBHs, such as mass ratio, separation, spin, eccentricity, etc. Maturing both in situ and ex situ formation channels is indispensable for understanding the origins of BBHs, making full use of the observational constraints.

3.   Binary neutron stars

3.1.   *Exploring NS physics*

3.1.1.   *BNS waveform modeling based on numerical relativity simulations*

GWs from BNSs contain rich information on the NSs. In particular, the tidal deformability of NSs has been proposed as one of the most promising quantities related to the equation of state (EOS) that can be extracted from GW observation [110–125]. The tidal deformability λ is defined through $Q_{ij} = -\lambda E_{ij}$, where Q_{ij} and E_{ij} are the induced quadrupole moment and the external tidal field, respectively. The tidal deformability can also be written in terms of the radius of the neutron star, R, and its Love number, k_2, as $\lambda = 2k_2R^5$. Therefore, the behavior of λ depends on the inner structure of an NS, its EOS. For example, for soft (stiff) EOSs, the radius of an NS is small (large), and therefore the NS is less (more) deformed, i.e. λ takes a small (large) value. The simultaneous measurement of the mass and the tidal deformability of NSs provides a substantial constraint on the equation of state of nuclear matter, which remains poorly understood [126,148].

To extract the tidal deformability of NSs from the observed signals, an accurate theoretical waveform template is crucial. For this purpose, many efforts have been made to model the gravitational waveforms of an NS merger in the past few decades. Waveforms including linear-order tidal effects are derived by post-Newtonian (PN) calculation for the early inspiral stage [116,123]. Furthermore, waveforms employing the *effective one-body* (EOB) formalism are derived to incorporate higher-order PN effects [110–114,127–131]. However, these waveform models are not accurate enough for the estimation of the tidal deformability due to the significant systematic error of the unknown higher-order PN terms [115,118,124,125]. Furthermore, the tidal correction to the waveforms is derived based on the PN calculation, which is only valid in the regime where the orbital separation

is sufficiently large. Since the tidal effect is most significant just before the merger, it is necessary to examine the accuracy of these waveform models.

Numerical relativity (NR) simulation is the only method that predicts the tidal effects in a regime where the nonlinear effect of hydrodynamics should be taken into account in the framework of general relativity [127,132–141]. The recent progress in numerical techniques and computational resources enabled us to perform high-precision NR simulations for BNS mergers and to generate waveforms with systematic errors sufficiently small for GW data analysis.

In our recent work [139,142,143] we performed NR simulations for NS–NS mergers, systematically varying the mass and the tidal deformability of NSs: six and four models that cover the symmetric mass ratio, η, in the range 0.247–0.25 and a binary with total mass ≈ 2.7 and $2.5\,M_\odot$, respectively, and five different EOSs which cover the binary tidal deformability in the range $\sim$300–1900. Here, the binary tidal deformability, $\tilde{\Lambda}$, is defined by

$$\tilde{\Lambda} = \frac{8}{13} \left[\left(1 + 7\eta - 31\eta^2\right)(\Lambda_1 + \Lambda_2) \sqrt{1 - 4\eta} \left(1 + 9\eta - 11\eta^2\right)(\Lambda_1 - \Lambda_2) \right], \qquad (3)$$

where $\Lambda_i = \lambda_i / m_i^5$ $(i = 1, 2)$ are the tidal deformability of each individual star (note that $m_1 < m_2$). In this work the waveforms from NS–NS mergers for more than 15 inspiral orbits were obtained for a wide range of binary parameters.

We carefully estimated the error budgets of the waveforms obtained by NR simulations. In our NR simulation code, the field equations are solved under discretization. We found that the error due to the finite grid resolution is the largest of the error sources in the numerical simulation. To estimate the error due to the finite grid resolution, we performed simulations with various grid resolutions and checked the convergence property of the obtained waveform data. We found that the phase error of the waveforms is of sub-radian order [139,142,143].

Employing the obtained high-precision NR waveforms, we examined the validity of the analytical waveform models for NS binaries. We showed that the latest tidal-EOB (SEOBNRv2T [128,131]) waveforms can be accurate even up to $\sim$3 ms before the onset of merger [139] (see Fig. 9 for an example). However, the phase difference between the tidal-EOB waveforms and the NR results is still larger than $\sim$1 rad after two NSs come into contact for the case that the NS radii are larger than $\sim$13 km. This finding indicates that further improvement of the waveform model is needed to suppress the systematic error in the measurement of the tidal deformability.

For this purpose, we developed a phenomenological model for GWs from inspiraling NSs based on our high-precision NR simulations. Our phenomenological waveform model is derived in the frequency domain, as in the Phenom series for binary black holes [144], for convenience in data analysis. We decompose a frequency-domain gravitational waveform, $\tilde{h}(f)$, into the frequency-domain amplitude, $A(f)$, and phase, $\Psi(f)$, with an ambiguity in the origin of the phase, by

$$\tilde{h}(f) = A(f)\,e^{-i\Psi(f)}, \qquad (4)$$

and we define the corrections of the NS tidal deformation to GW amplitude and phase, respectively, by

$$A_{\text{tidal}}(f) = A(f) - A_{\text{BBH}}(f), \qquad (5)$$

$$\Psi_{\text{tidal}}(f) = \Psi(f) - \Psi_{\text{BBH}}(f). \qquad (6)$$
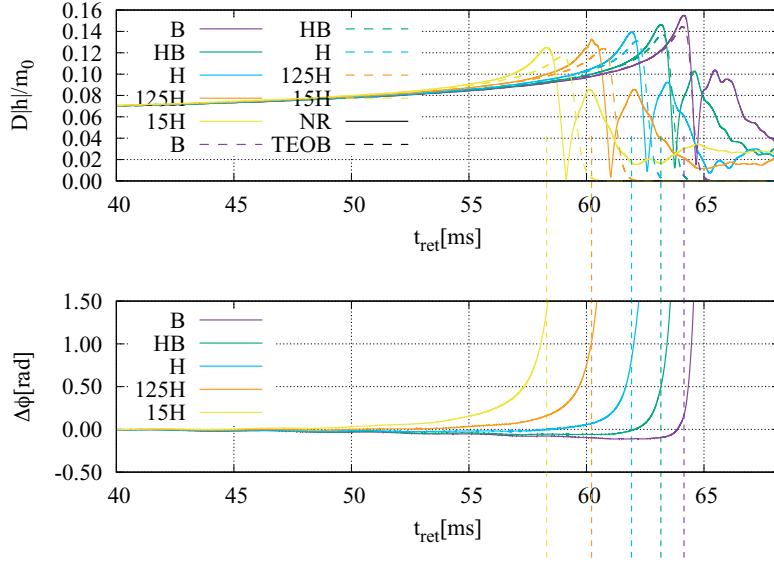
Fig. 9. Comparison between NR and SEOBNRv2T waveforms for the models with a total mass of $\sim 2.5\,M_\odot$ and symmetric mass ratio of 0.247. The top and bottom panels show the amplitudes of the NR and SEOBNRv2T waveforms and the phase difference between them, respectively. Here, D and m_0 denote the distance to the source and the total mass of the binary. The vertical dashed lines are the peak amplitude time when the GW amplitude reaches a peak in each model.

Here, $A_{\mathrm{BBH}}(f)$ and $\Psi_{\mathrm{BBH}}(f)$ are the GW amplitude and phase of a binary black hole with the same mass as the BNS (hereafter referred to as the point-particle parts). In this work, we employ the SEOBNRv2 waveforms [145] as the fiducial point-particle part of GWs.

For the tidal part phase and amplitude of our phenomenological waveform model we employ the following function forms motivated by the 2.5 PN order post-Newtonian formula [114,138] for the tidal-part amplitude and phase correction:

$$\Psi^{\mathrm{tidal}} = \frac{3}{128\eta}\left[-\frac{39}{2}\tilde{\Lambda}(1 + a\tilde{\Lambda}^{2/3}x^p)\right]x^{5/2}\left(1 + \frac{3115}{1248}x - \pi x^{3/2} + \frac{28024205}{3302208}x^2 - \frac{4283}{1092}\pi x^{5/2}\right) \tag{7}$$

for the phase correction, and

$$A^{\mathrm{tidal}} = \sqrt{\frac{5\pi\eta}{24}}\frac{m_0^2}{D_{\mathrm{eff}}}\tilde{\Lambda}x^{-7/4}\left(-\frac{27}{16}x^5 - \frac{449}{64}x^6 - bx^q\right) \tag{8}$$

for the amplitude correction. Here, a, p, b, and q are the free parameters of the models.

Since our NR waveforms only contain the waveforms with frequency larger than $\sim 400\,\mathrm{Hz}$, they are too short to calibrate the phenomenological waveform model by themselves. Thus, for this purpose, we construct hybrid waveforms employing our NR waveforms and the EOB waveforms of Refs. [128,131] (SEOBNRv2T) as the high- and low-frequency parts, respectively, and use them to calibrate the phenomenological waveform model. Hybridization of the waveforms is performed in the time domain by the procedure described in Refs. [138,142].

To focus on the inspiral-phase waveform and to avoid contamination from post-merger waveforms, which would have large uncertainties, we restrict the GW frequency range to 10–1000 Hz. The fitting parameters are determined by employing the hybrid waveforms with the largest values of binary tidal
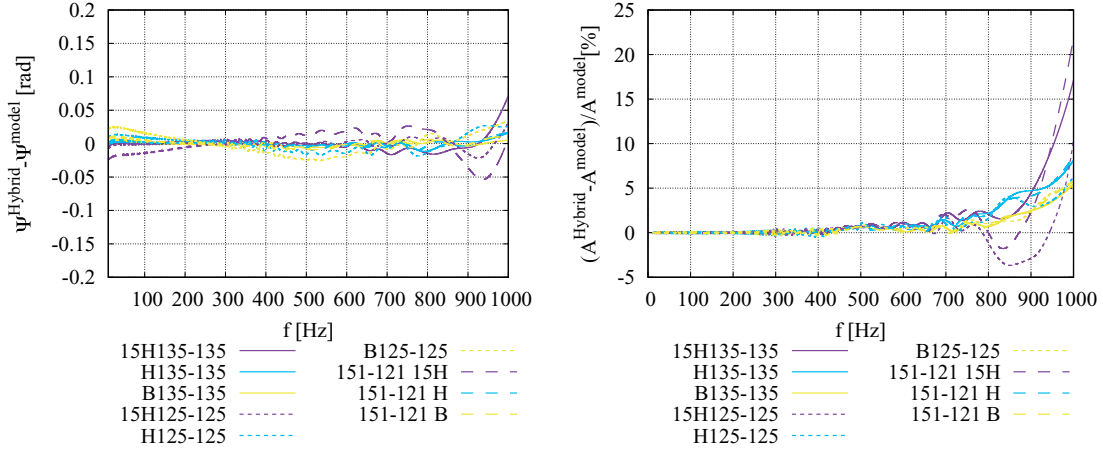
Fig. 10. (Left) Difference in the tidal-part phase between the hybrid waveforms and our analytical model for the various binary configurations (see Refs. [139,142] for the details of the models). Phase differences are plotted after alignment in the frequency range 10–1000 Hz. (Right) Relative amplitude difference between the hybrid waveforms and our analytical model.

deformability in the models studied in this work. By performing a least-squares fit with respect to the phase difference and relative amplitude difference, we obtained $a = 12.55$, $p = 4.240$, $b = 4251$, and $q = 7.890$. Employing these parameters, we find that the phase and amplitude corrections to the frequency domain waveforms are reproduced within 0.1 rad and 25% for all the binary configurations studied in this work (see Fig. 10).

To validate our phenomenological waveform model more quantitatively from the data analysis viewpoint, we calculate the mismatch between the our waveform models and the hybrid waveforms, $\bar{F}$, defined by

$$\bar{F} = 1 - \max_{\phi_0, t_0} \frac{\left(\tilde{h}_1 \mid \tilde{h}_2 e^{2\pi i f t_0 + i\phi_0}\right)}{||\tilde{h}_1|| \, ||\tilde{h}_2||}, \tag{9}$$

where $(\cdot \mid \cdot)$ and $|| \cdot ||$ are defined by

$$\left(\tilde{h}_1 \mid \tilde{h}_2\right) = 4\mathrm{Re}\left[\int_{f_{\min}}^{f_{\max}} \frac{\tilde{h}_1(f)\,\tilde{h}_2^*(f)}{S_{\mathrm{n}}(f)} df\right], \qquad \rho = ||\tilde{h}|| = \sqrt{\left(\tilde{h} \mid \tilde{h}\right)}. \tag{10}$$

Here, S_{n} denotes the one-sided noise spectrum density of the detector, and we employ the noise spectrum density of the `ZERO_DETUNED_HIGH_POWER` configuration of advanced LIGO [146] for it. We found that the mismatch between our phenomenological waveform model and the hybrid waveforms is always within 10^{-5} [142,143].

Gravitational waveform models for BNSs based on NR waveforms are also derived in Refs. [134, 135] in a similar manner. The main difference between our and their work is the difference of the NR waveforms and the tidal-EOB waveforms used for the model calibration. Figure 11 compares our tidal phase correction model and those of Refs. [134,135] normalized by the leading-order PN term (see also Refs. [135,147]). Figure 11 shows that the models agree with each other within 10%–20% for 10–1000 Hz. Indeed, the models give consistent results for the current detector sensitivity, as shown in the next subsection (see also Ref. [135]).
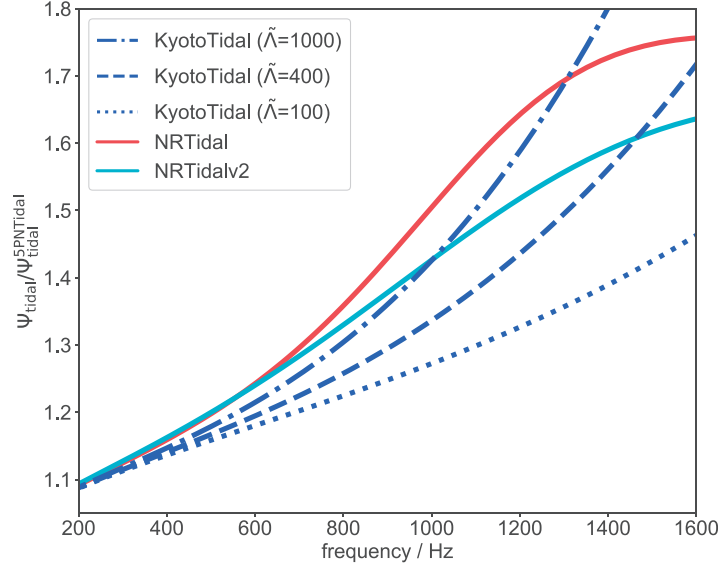
Fig. 11. Tidal phase in the frequency domain normalized by the leading Newtonian (relative 5PN order) tidal phase formula. Our analytical model (referred to as `KyotoTidal`) assuming $\tilde{\Lambda} = 1000$ (dot-dashed, blue), 400 (dashed, blue), and 100 (dotted, blue), the `NRTidal` model (solid, red [134]), and the `NRTidalv2` model (solid, cyan [135]) are shown in the plot. Note that latter two models are independent of $\tilde{\Lambda}$ when normalized by the leading tidal phase.

3.1.2. *Measuring tidal deformability from GWs*

As mentioned above, NSs provide unique laboratories for studying the properties of ultra-dense matter. To constrain the EOS of NSs effectively, we need accurate waveform models for the data analysis. We assume that the waveform of the GWs can be decomposed into the point-particle, spin, and tidal parts. The point-particle and the spin parts are the same as for the BBH case; on the other hand, the tidal part is that of the BNS case because of the matter effects of NSs. The standard waveform, the so-called `TaylorF2` (hereafter `TF2`), is derived by the PN approximation [151]. The point-particle [152,153] and spin parts [154–156] are calculated up to the 3.5PN order, while the effect of the tidal part (let us call it `PNTidal`) enters from the 5PN order, calculated up to the 7.5 PN order [114]. Since the tidal effects become important at the late inspiral stage where the PN approximation becomes invalid, we need better waveform models to accurately estimate tidal deformability.

Dietrich et al. [134,135] (`NRTidal`) and Kawaguchi et al. [142] (`KyotoTidal`) independently constructed new waveform models in which the tidal part is improved by calibration using NR waveforms. In `KyotoTidal`, nonlinear effects of $\tilde{\Lambda}$ are taken into account. The lack of point-particle and spin parts beyond the 4PN order also bias the measurement of binary quantities. Kawaguchi et al. have also constructed higher PN order correction terms of the point-particle part by fitting the `SEOBNRv2` waveform model [145,157], so-called `TF2+`. Here, `TF2+_KyotoTidal` is calibrated in the frequency range 10–1000 Hz, because they focused on the inspiral phase to avoid the uncertainties in the post-merger phase. Several studies have also derived constraints on the NS EOS via measuring tidal deformability from GW170817 [158–168].

Narikawa et al. separately analyzed the GW data of a binary–neutron star merger, GW170817, from the Advanced LIGO twin detectors [169]. They found that the posterior probability distributions of the binary tidal deformability for the Hanford and Livingston detectors are distinctively different, as
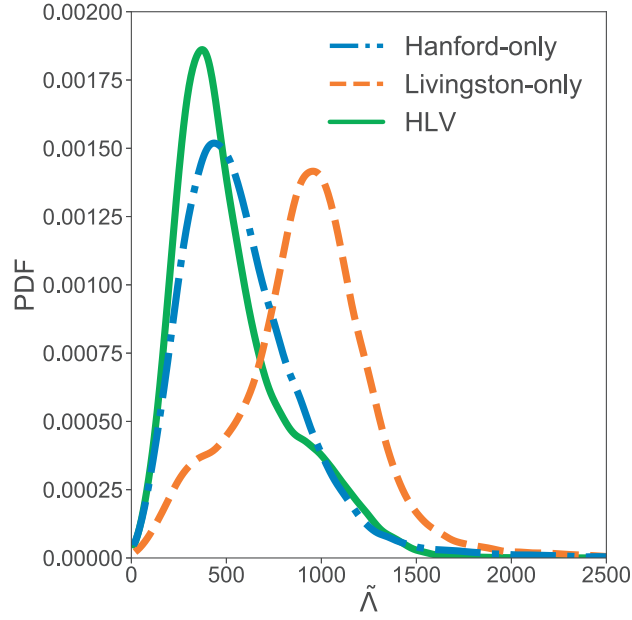
Fig. 12. Marginalized posterior probability distribution of binary tidal deformability, $\tilde{\Lambda}$, for GW170817, derived by data of different detectors with $f_{max} = 2048$ Hz. (Reprinted with permission from Ref. [169]. © 2017, American Physical Society.)

shown in Fig. 12. They suggested that the difference between the detectors cannot be understood by statistical error alone, since only the posterior with the Livingston detector does not change smoothly as the upper cutoff frequency increases. Their findings suggest that further research into the noise properties in the high-frequency region of the Livingston data is needed to extract information on the tidal deformability of GW170817. Narikawa et al. also found that there is a difference in the estimates of $\tilde{\Lambda}$ for GW170817 between NR-calibrated waveform models (KyotoTidal and NRTidalv2) as shown in Fig. 13 [147]. Here, NRTidalv2 model is an upgrade of the NRTidal model [135]. The order of peak values of $\tilde{\Lambda}$ for the different waveform models in Fig. 13 can be understood by the difference in the magnitude of the tidal phase at around $\tilde{\Lambda} \approx 600$–$900$ shown in Fig. 11. However, the difference is smaller than the statistical error.

The second BNS merger event, GW190425, was observed during O3a [170]. The total mass of the system was about $3.4\,M_\odot$, which is larger than the total mass of any other known BNS system. Since the LIGO Hanford detector was offline at the time of the event, parameter estimation was performed using the data from the LIGO Livingston and Virgo detectors. An EOS with large tidal deformability, $\tilde{\Lambda} > 1100$, was disfavored, which is consistent with the several analyses done for GW170817. For the low-spin prior (component spin is enforced as $\chi_{1,2} \sim U[-0.05, 0.05]$), the 90% upper limit of GW190425 becomes much smaller than that of GW170817, $\tilde{\Lambda} \leq 600$. Since the total mass of the system was large, the possibility of a BH–NS system is discussed in Ref. [170].

3.2. Association of a short-duration gamma-ray burst

3.2.1. High-energy observations

The observations of GW170817 by high-energy instruments, *Fermi*, *MAXI*, *Swift*, *CALET*, and *Chandra*, are reviewed in this subsection.
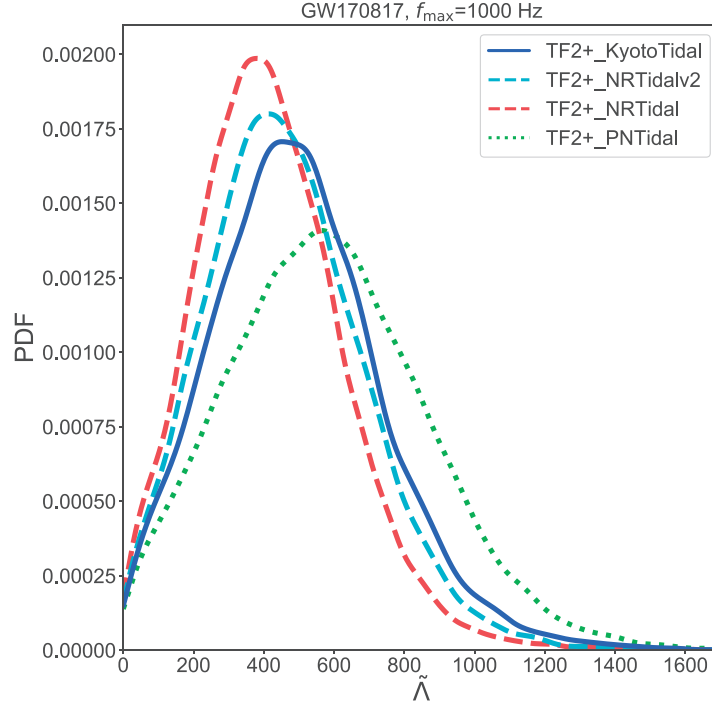
Fig. 13. Marginalized posterior PDFs of binary tidal deformability, $\tilde{\Lambda}$, for GW170817, estimated by different waveform models for $f_{max} = 1000\,\mathrm{Hz}$.

Fermi On August 17, 2017, at 12:41:06.5 (UTC), hard X-ray emission from GRB 170817A triggered the *Fermi* Gamma-ray Burst Monitor (GBM, with a coverage of 8 keV–40 MeV; [171]) near the detection limit [172]. The emission with a short hard pulse and a soft tail lasted for $\sim$2 s, as shown in Fig. 14. From the obtained time duration, this GRB is classified as a short GRB. Also, the SPectrometer on board the *INTEGRAL* Anti-Coincidence Shield (SPI-ACS) detected a hard pulse completely coincident with the *Fermi*/GBM one [173].

Amazingly, the binary coalescence detected by the Laser Interferometer Gravitational-wave Observatory (LIGO) occurred $\sim$1.7 s before the *Fermi*/GBM trigger [9], and the sky position determined by the LIGO GW observation is consistent with the *Fermi*/GBM one. The gamma-ray spectrum for the initial hard pulse is well fitted by a power-law function with a photon index of $\alpha = -1.6 \pm 0.4$ and an exponential cutoff at $E_{peak} = 185 \pm 62$ keV. For the soft tail emission, a blackbody with $k_B T = 10.3 \pm 1.5$ keV represents the spectrum well. The fluence over the total duration is $\sim 3 \times 10^{-7}$ erg cm^{-2}, which falls in the $\sim$50th percentile of the fluence distribution obtained by *Fermi*/GBM [172]. Assuming a distance to the host galaxy NGC 4993 of 43 Mpc, the isotropic equivalent energy and peak luminosity in the 1 keV–10 MeV band are $\sim 3 \times 10^{46}$ erg and $\sim 2 \times 10^{47}$ erg s^{-1}, respectively, which are by 3–6 orders of magnitude smaller than those of other short GRBs detected by *Fermi*/GBM. The observed features for GRB 170817A would suggest that the hard X-ray emission came from a jet misaligned with the observer (i.e. an off-axis jet).

The higher-energy gamma-ray observation of GRB 170817A by the *Fermi* Large Area Telescope (LAT [174]) covering the 0.1–300 GeV band was unfortunately not available due to entering the South Atlantic Anomaly at the merger time [17]. *Fermi*/LAT resumed scientific operation $\sim 10^3$ s
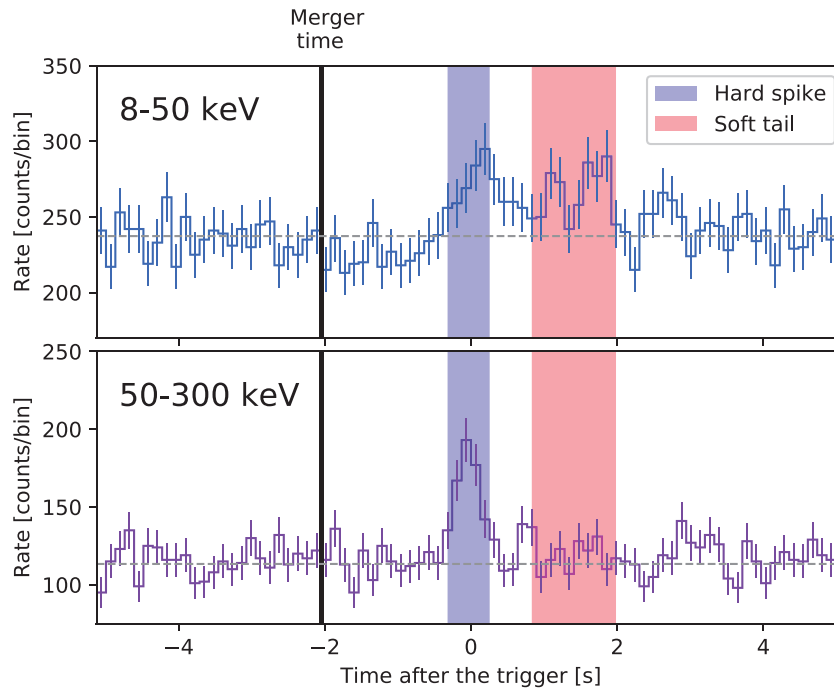
Fig. 14. Light curve of GRB 170817A detected by GBM in the 8–50 keV and 50–300 keV bands. The emission consists of a hard pulse and a weak soft tail. The vertical solid line represents the time of the binary neutron star merger. The horizontal dashed line represents the averaged background level.

after the merger time and put a flux upper limit of 4.5×10^{-10} erg cm^{-2} s^{-1} (95% confidence level) in the 0.1–1 GeV band using the initial 1000 s observation after the resumption of operation.

Motivated by study of GRB 170817A, investigation of previous short GRBs with a similar signature has been performed [175–178]. In particular, the nearby short GRB 150101B detected by *Fermi*/GBM ($z = 0.134$ [179]), which could accompany the kilonova and the off-axis jet emission suggested by the optical and X-ray observations [176], has a hard spike and a soft tail. Thus, the two-component signature could be a common feature for short GRBs [175]. The isotropic equivalent energy and luminosity in the 1 keV–10 MeV band are $\sim 2 \times 10^{49}$ erg and $\sim 4 \times 10^{50}$ erg s^{-1}, respectively, which are in the fiducial range of short GRBs. One possible interpretation for these phenomena suggests that GRB 150101B could originate from a more on-axis jet than GRB 170817A.

MAXI Monitor of All-sky X-ray Image (*MAXI* [180]) is an instrument for monitoring the X-ray sky that was launched in 2009 and has been observing from the International Space Station (ISS). Because *MAXI* does not have a moving mechanism and is mounted on the ISS, we cannot actively control the pointing direction. The orbital period of the ISS is 92 min, and thus an X-ray source is usually observed once in the same period. Since *MAXI* covers about 85% of the sky every orbit, the source activity can trace back to the time before the event.

In studying X-ray counterparts of GW events, we use the Gas Slit Camera (GSC [181]), which consists of 12 position-sensitive proportional counters. Six of them cover a $3° \times 160°$ field of view (FOV) toward the horizontal direction, and the others provide a zenithal FOV with the same dimension. These FOVs move as the ISS rotates. A scan observation (transit) for a point source lasts 40–150 s depending on the source position in the FOV [182].
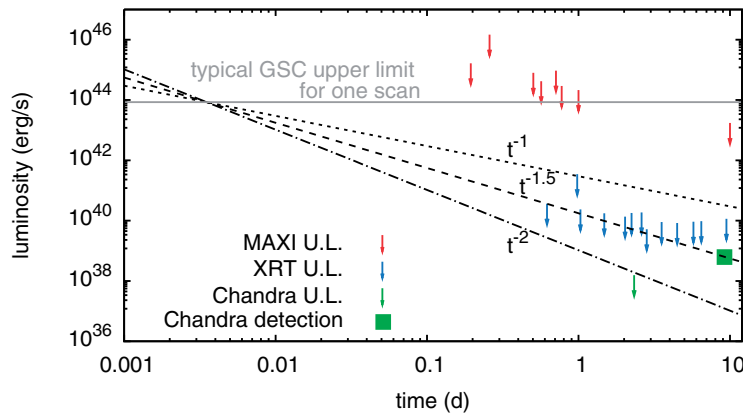
Fig. 15. The observed luminosity and upper limits of the X-ray counterpart of GW170817 in early time. *MAXI* upper limits are based on the results of Ref. [183]. The first six points are for each scan transit and the last two are for one-day and ten-day observations. The data from *Swift* XRT and *Chandra* are converted to the luminosity at 2–10 keV assuming the spectral parameters in their original papers [184,185]. The dotted, dashed, and dash-dotted lines are models for luminosity L as a function of the time t, $L \propto t^\alpha$, with $\alpha = -1$, -1.5, and -2, respectively. The horizontal gray line is a typical GSC upper limit for one scan transit, scaled to the distance of GW170817 (40 Mpc).

The effective area of the GSC for a source changes with time linearly like a triangle. For a source with constant flux (or that can be assumed as constant in a scan transit), we calculate an average flux by dividing the source count by the effective exposure, that is, the sum of the effective area over the time.

For GW170817, *MAXI* did not detect the X-ray emission. The upper limits are summarized in Ref. [183]. Figure 15 shows the luminosity and upper limits for early (< 10 days) X-ray afterglows [184,185] in the case of GW170817. The position of the EM counterpart lay at the gap between the horizontal and the zenithal cameras for the first three orbits and the first scan started after 4.7 hours. Moreover, the first three observations were incomplete and the upper limits were 1–2 orders of magnitude higher than usual. However, it is important to mention that this was the earliest observation of the X-ray counterpart of a GW event.

Although the observation start time was late in this case, if *MAXI*'s observation started ∼100 s after the trigger, *MAXI* could observe an X-ray afterglow equivalent to the level observed by Swift at several hours after the trigger.

The best lesson of the observation of GW170817 was that it is important to continuously observe the sky as long as possible. In O3 we have increased the observation efficiency to reduce the gap in observations.

Swift　The Neil Gehrels *Swift* Observatory [186] consists of three scientific instruments. The Burst Alert Telescope (BAT [187]) is a wide-field-of-view telescope monitoring about 1/6 of the sky in the 15–150 keV band. The X-ray Telescope (XRT [188]) is an X-ray telescope covering the energy range in the 0.3–10 keV band over a 24′ field of view. The UV-Optical Telescope (UVOT [189]) observes the wavelength range of 170–600 nm over a 17′ field of view.

At the merger time of GW170817, the error region of GW170817 was occulted by the Earth and not visible by BAT [184,190]. Therefore, no useful information can be derived from the BAT data. The XRT and UVOT started their observations about an hour after the merger time around the center of the *Fermi* GBM error region (∼1° radius). After the localization information became available

from LIGO and Virgo at 4.8 hr after the merger time, *Swift* started a series of 120 s observations at the positions of known galaxies inside the 33.6 deg^2 error region of the GW detectors. No new X-ray sources ($\geq 10^{-12}$ erg cm^{-2} s^{-1}) were found during those observations [184].

Swift started the observations at the position of the optical transient of GW170817 about 14.4 hr after the merger time. Although the XRT found no X-ray from the position of the transient, the UVOT detected a fast-decaying UV emission which is interpreted as the blue kilonova associated with GW170817. The non-detection of X-rays at the early phase by XRT is a crucial difference in a typical short GRB afterglow which is dominated by an on-axis emission [184].

CALET   The Calorimetric Electron Telescope (*CALET* [191,192]) is a scientific instrument on board the ISS. The *CALET* Gamma-ray Burst Monitor (CGBM [193]) uses two different detectors and is capable of observing emissions from 7 keV to 1 MeV—Hard X-ray Monitor (HXM), ~60° field of view from the boresight—and from 40 keV to 20 MeV—Soft Gamma-ray Monitor (SGM), ~110° field of view from the boresight. No significant emission was observed by CGBM at the time of the merger of GW170817. The 90% upper limit is 1.3×10^{-7} erg cm^{-2} s^{-1} in the 10–1000 keV band, assuming no shielding by the structure of the ISS [36].

In addition, the main *CALET* instrument, the high-energy calorimeter (CAL), observes gamma-rays from ~1 GeV up to 10 TeV with a field of view of nearly 2 sr. The field of view of CAL did not include the location of GW170817 at the time of the merger. A search for delayed emission over the two-month period following the event resulted in 90% C.L. upper limits on the energy flux of 1.2×10^{-10} erg cm^{-2} s^{-1} for gamma-rays above 1 GeV and 4.0×10^{-10} erg cm^{-2} s^{-1} above 10 GeV [194].

Chandra   The *Chandra* X-ray Observatory, which provides the best sensitivity in X-ray for a point source, was first targeted at the optical transient of GW170817 2.2 d after the merger time. Although no X-ray emission was detected in this first visit, *Chandra* detected significant X-ray emission on the second visit at 8.9 d after the merger in isotropic luminosity of 9×10^{38} erg s^{-1} at a distance of 40 Mpc [195].

According to the year-long monitoring observations by *Chandra*, the X-ray flux continued to increase up to ~160 d after the merger time with a power-law index of 0.9 [196,197]. After the peak, the flux showed a decline with a power-law index of ~ -2 (Fig. 16). There is a hint of an X-ray flaring feature around 155 d after the merger time [198]. *Chandra* has been collecting data up to 2.5 yr after the merger and continues monitoring. This unique X-ray light curve behavior along with the radio data will be discussed in the following section.

3.2.2.   Theoretical interpretation
The GW event GW170817 [9] and the associated short GRB 170817A [36,172,173] have provided, for the first time, clear evidence for a relativistic jet from a binary neutron star merger observed from off-axis (as shown schematically in Fig. 17). The observations also show that the jet is structured, excluding a top-hat distribution of energy and Lorentz factor of the jet. We also discuss the current issues concerning the exact structure of the jet, the origin of the gamma-ray emission, and future prospects.

Evidence of an off-axis jet   The afterglow observations of GW170817A verify the existence of a relativistic jet: the superluminal motion of the radio image indicates a relativistic collimated
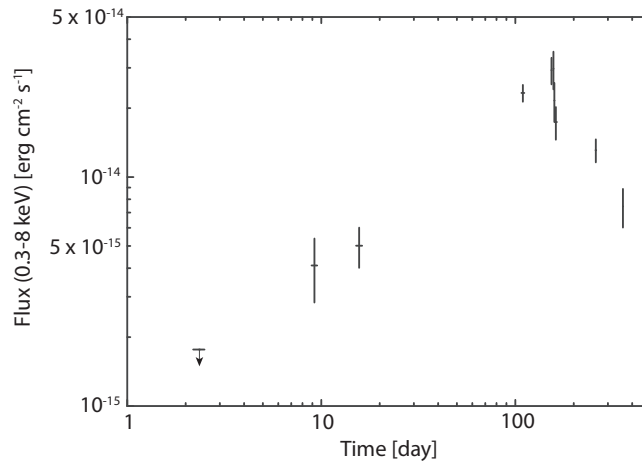
Fig. 16. The X-ray light curve of the counterpart of GW170817 observed by *Chandra*. The source count-rates are converted to unabsorbed flux in the 0.3–8 keV band using the Galactic absorption column $N_{\rm H} = 7.6 \times 10^{20}$ cm^{-2} and a photon index of 1.59 [197].
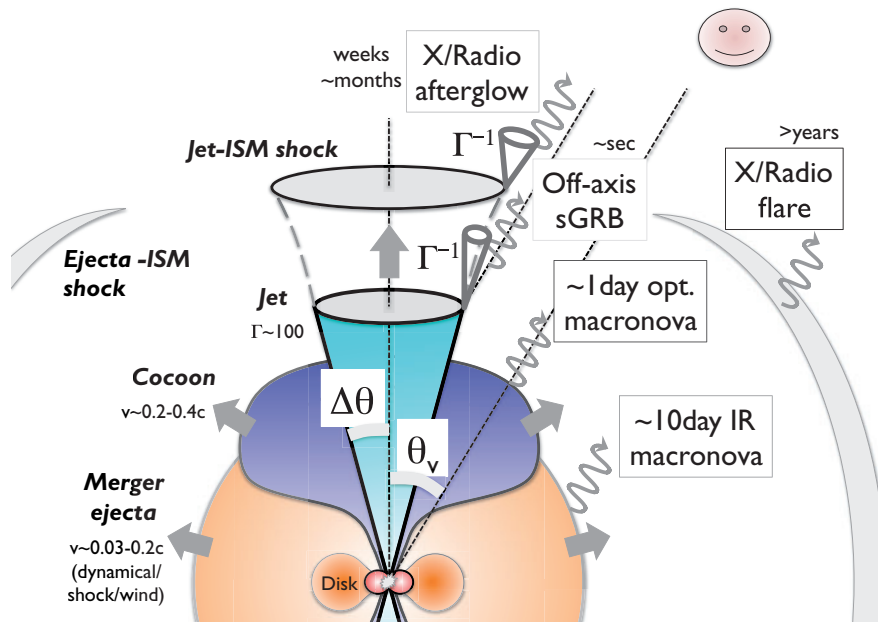
Fig. 17. Electromagnetic counterparts associated with the off-axis jet from the short GRB 170817A (from Fig. 1 of Ref. [13]).

source [11,12] and the closure relation between the spectral index and the light curve slope after the luminosity peak is consistent with the standard afterglow model of a relativistic jet [197,199,200], excluding a failed-jet scenario that the jet is choked by the ejecta from the neutron star merger [201–203].

The jet should be strong enough to successfully break out of the merger ejecta in this event [204,205]. The breakout time since the jet launch ($t = t_0$) is approximately estimated as

$$t_{\rm b} - t_0 \sim 0.17\,{\rm s}\left(\frac{t_0 - t_{\rm m}}{0.1\,{\rm s}}\right)^{1/2}\left(\frac{L_{\rm iso,0}}{10^{51}\,{\rm erg\,s^{-1}}}\right)^{-1/2} + 0.078\,{\rm s}\left(\frac{L_{\rm iso,0}}{10^{51}\,{\rm erg\,s^{-1}}}\right)^{-1}, \qquad (11)$$
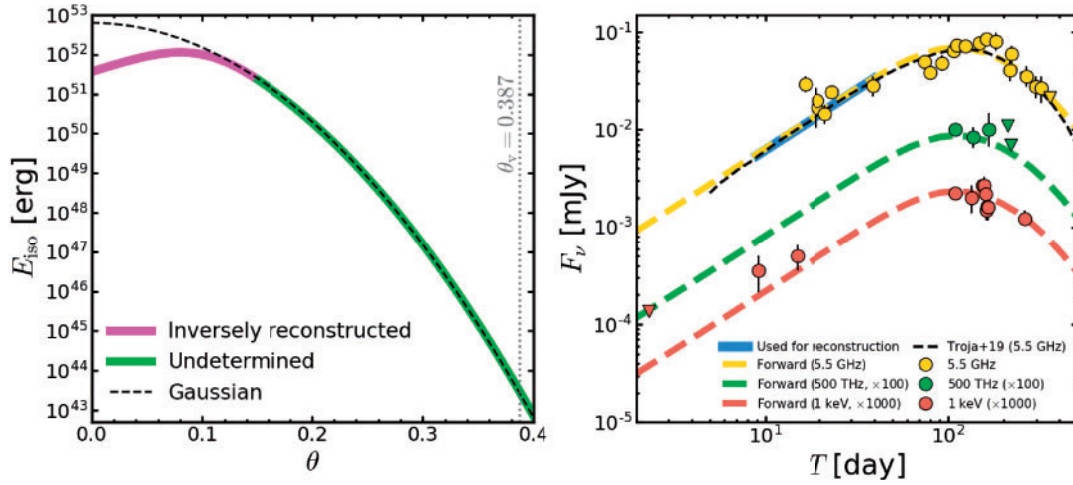
Fig. 18. Left: Examples of jet structure that are consistent with the afterglow observations of GRB 170817A: a hollow-cone (magenta line) and Gaussian jet (dashed line). The green region is not in principle determined by the current data. Right: The corresponding light curves for a hollow-cone (thick dashed lines) and Gaussian jet (thin dashed line) with the data. The blue line is used for the inverse reconstruction (modifying Fig. 8 of Ref. [216]).

where $L_{\rm iso,0}$ is the isotropic luminosity at the base of the jet and $t_0 - t_{\rm m}$ is the time delay of the jet launch since the merger (modifying Eq. (32) of Ref. [206]). Here, the second term is necessary for this event because the ejecta expansion velocity is comparable to the jet head velocity, in contrast to collapsars with a static envelope. In order to have the short GRB 170817A $\sim$1.7 s after the merger, the jet luminosity should be large enough, $L_{\rm iso,0} \gtrsim 3 \times 10^{49}\,{\rm erg\,s^{-1}}$, and the delay time should be short enough, $t_0 - t_{\rm m} \lesssim 1.3\,{\rm s}$ [206].

The observed isotropic energy of the gamma-ray emission is very small, several orders of magnitude smaller than typical [36,172,173]. Therefore the jet should be off-axis for a reasonable radiative efficiency [13,14]. An off-axis observer receives photons emitted outside the relativistic beaming cone, and the apparent energy of the off-axis jet becomes faint (see also below).

Diverse jet structures The afterglow observations, in particular the slowly rising light curves from radio to X-ray, are not consistent with a top-hat jet [207], but indicate a structured jet [12,197,200,208–213]. These are the first confirmation of the previous suspicion that realistic GRB jets are structured [214,215].

However, there remains confusion about the jet structure as different authors give different structures, such as Gaussian [197,200,210] and power-law profiles [12,208] (see Fig. 1 of Ref. [13]). These structures are obtained by assuming a functional form of the jet structure with model parameters, and adjusting the parameters through fitting the theoretical light curves to the observations.

We instead invented a novel method to determine the functional form of the jet structure itself [216]. This method solves an inverse problem, uniquely reconstructing a jet structure from a given off-axis GRB afterglow, by integrating an ordinary differential equation which is formulated based on the standard theory of GRB afterglows. Applying the inversion method to GRB 170817A, we clarified that the current observational errors still allow various jet structures, discovering the by-product that a hollow-cone jet is also consistent with the observations, as shown in Fig. 18.
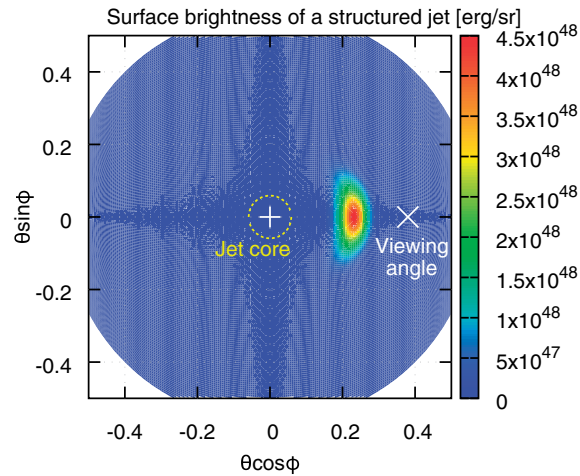
Fig. 19. The surface brightness distribution of the prompt emission from a Gaussian jet (from Fig. 3 of Ref. [14]).

An important caveat is that the current afterglow observations only constrain the jet core (magenta in Fig. 18), not in principle the outer jet structure (green; which is crucial for the gamma-ray emission, as discussed below). Early afterglow observations are required to obtain the outer jet structure [216].

The origin of the jet structure is still unclear. First, the jet may have intrinsic structure from the beginning of the launch. Second, the jet may be structured during the propagation if the outer part loads baryons from the ejecta. Third, the cocoon component (the collided jet and ejecta) may contribute to the outer structure since part of the cocoon is relativistic due to partial mixing of the baryons. Early macronova/kilonova observations are important for probing the cocoon, which has crucial information on the jet.

Origin of the gamma-ray emission   Prompt gamma-ray emission such as GRB 170817A generally comes from an off-center jet, neither the jet core nor the line of sight but the middle, as in Fig. 19 [14], given a jet structure with a rapidly decaying tail as in Fig. 18. This is because the emission from the jet core is suppressed by the relativistic de-beaming, while the line-of-sight emission becomes too faint to dominate the off-axis emission from the inner jet. The off-center emission seemingly solves the puzzle that the observed prompt spectrum is inconsistent with the spectral Amati relation [217,218] (because the off-center emission is different from the usually observed jet core) and causes the compactness problem [219,220] (because the off-centre jet is much less energetic and much closer to the line of sight than the jet core).

The off-center structure still has large uncertainties because it is not constrained by the observed afterglows (as shown by the green region in Fig. 18). Whether it is a jet or a cocoon is also unknown. The observed gamma-rays might be jet emission scattered by the cocoon [221]. Future observations of off-axis events will reveal the jet structure, where roughly ~10% events are expected to be brighter at smaller viewing angles than GRB 170817A.

3.3.   Optical/infrared counterparts and heavy element nucleosynthesis

The origin of the elements in the universe is a subject of interest in astronomy and astrophysics. In particular, the origin of the elements synthesized by rapid neutron capture, the so-called *r*-process,

is a long-standing unsolved problem. Theoretically, NS mergers are one of the promising candidate sites for *r*-process nucleosynthesis [222–230]. However, there has been no observational evidence of *r*-process in NS mergers.

When NS mergers occur, a small fraction of the mass of NSs is ejected into interstellar space [227,229,231–234]. In the ejected material, *r*-process nucleosynthesis is expected to take place. Then, we expect optical and infrared emission powered by the radioactive decay of freshly synthesized nuclei [235–240]. This phenomenon is called "kilonova" or "macronova" (here we call it kilonova). In other words, if we can detect kilonova after detection of GWs from an NS merger, we can test *r*-process nucleosynthesis in the NS merge.

The event rate of NS mergers can be measured from GW observations. The ejection of *r*-process elements per event can be estimated from electromagnetic (optical/infrared) observations. Therefore, from these multi-messenger observations we can study the production rate of *r*-process elements by NS mergers and test whether NS mergers can be the origin of the *r*-process elements in the universe.

To achieve observations of kilonova, we coordinated with the Japanese collaboration for Gravitational wave ElectroMagnetic follow-up (J-GEM, Sect. 3.3.1). Thanks to this observational network, we succeeded in observations of the electromagnetic counterpart of GW170817 (Sect. 3.3.2). By combining our state-of-art numerical simulations (Sect. 3.3.3), we advanced our knowledge of the physics of NS mergers and the origin of *r*-process elements in the universe.

3.3.1. *J-GEM*

J-GEM is a network of optical, infrared, and radio telescopes for EM follow-up observations of GW sources. Figure 20 shows a summary of the J-GEM telescopes. The roles of the optical telescopes can be divided into two categories: wide-field surveys (Kiso, MOA-II, and Subaru Hyper Suprime-Cam (HSC)), and galaxy-targeted surveys (other telescopes). For more details of each telescope, see Ref. [241]. J-GEM signed a memorandum of understanding with the LIGO/Virgo collaborations in 2014, and started to receive GW detection alerts from the first observing run of Advanced LIGO (O1).

We demonstrated coordinated observations using this observing network for the first GW source, GW150914 (BBH, [1]). Within 4 d of the GW detection (2 d from the initial alert), a $\sim$24 deg^2 area had been observed with the Kiso Schmidt telescopes. Within 6–7 d of the GW detection, 18 nearby galaxies were observed with the B&C 61 cm telescope. Although no EM counterpart has been identified, this was the first attempt at multi-messenger observations of GW sources [241].

A more intensive observing campaign was performed for the second GW source, GW151226 (BBH, [242]). For this event, 238 nearby galaxies were observed by galaxy-targeted surveys [243], which is a great improvement compared with the observations of GW150914. Also, the Kiso Schmidt and MOA-II telescopes covered 778 deg^2 and 145 deg^2 areas, respectively [243]. Furthermore, Subaru/HSC covered a 63.5 deg^2 area with unprecedented sensitivity (limiting magnitudes of 24.6 and 23.8 for the *i* and *z* bands, respectively [244]). The total area covered by the wide-field surveys was 986.5 deg^2, which corresponds to $\sim$29% of the probability map of GW151226. It is worth emphasizing that the sensitivity of Subaru/HSC observations was deep enough to detect expected kilonova emission even at about 200 Mpc, which is about the design sensitivity of Advanced LIGO, Advanced Virgo, and KAGRA.

Subaru/HSC is one of the most powerful wide-field imagers: its field of view (1.8 deg^2) is the largest among the 8–10 m-class telescopes. Table 3 summarizes our follow-up observations using
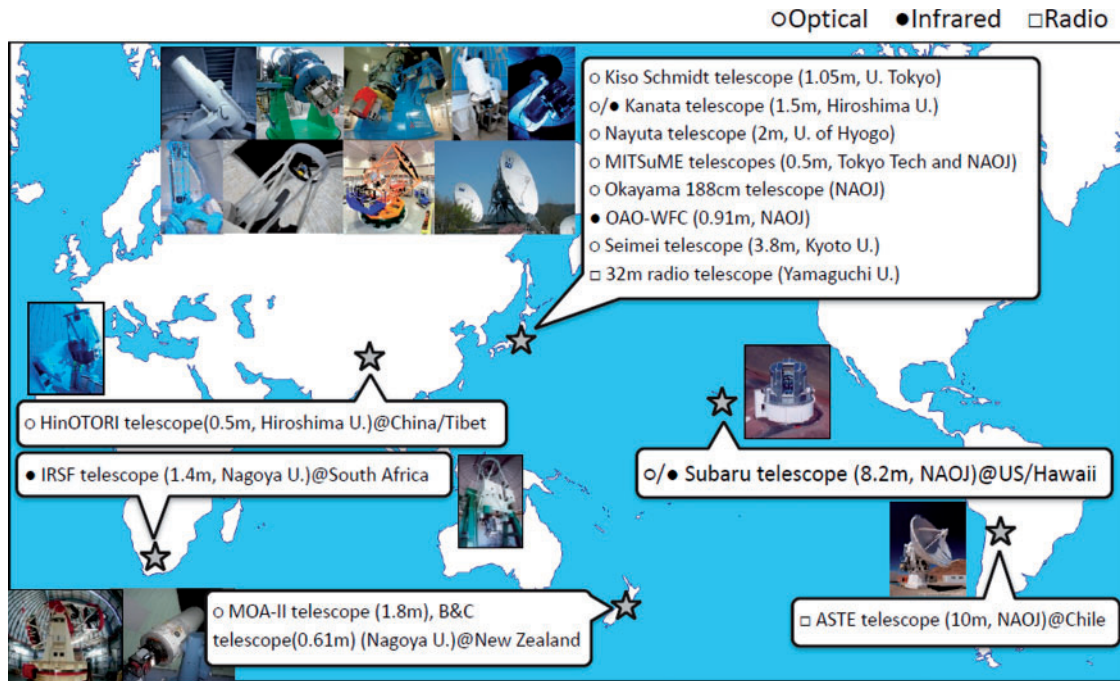
Fig. 20. Optical, infrared, and radio telescopes in the J-GEM network.

Subaru/HSC. Details of follow-up observations of S190510g are presented in T. Ohgami et al., Proc. Astron. Soc. Japan (submitted).

3.3.2. GW170817

The first GW detection from an NS merger was achieved for GW170817 [9]. The detection triggered EM follow-up observations covering the entire wavelength range [10]. Thanks to observations with three GW detectors, the position of the GW source was localized to $\sim30\,\mathrm{deg}^2$. In optical/infrared wavelengths, a counterpart AT2017gfo was identified by several groups [245–267].

We performed a wide-field survey using Subaru/HSC, covering $23.6\,\mathrm{deg}^2$ [264]. The observations recovered the detection of AT2017gfo. Furthermore, thanks to the wide coverage and good sensitivity, we statistically ruled out other transients in the localization area being associated with GW170817, or in other words, we concluded that AT2017gfo is the most likely counterpart.

Intensive optical and infrared observations of AT2017gfo were performed in the framework of the J-GEM network [266] (see Fig. 21). Observations with Subaru/HSC showed that the z-band brightness quickly declined. On the other hand, observations with IRSF/SIRIUS showed that the near-infrared light curves evolved more slowly. This is fully consistent with the expected behavior of kilonova.

Using radiative transfer simulations, we found that the observed light curves can be explained by $\sim0.03\,M_\odot$ of ejecta including lanthanide elements, which have a high opacity [268]. Also, the blue optical component, revealed by observations with Subaru/HSC, B&C/Tripol5, and MOA-II/MOA-cam3, requires an ejecta component with a smaller fraction of lanthanide. Since the estimated total ejecta mass is higher than the expected ejection by the first dynamical ejection from an NS merger, we concluded that the observed signals are mainly produced by post-merger mass ejection.

Table 3. Subaru/HSC observations for GW sources.

Target	Type	Disc. date (UUT)	Obs. date (UT)	Filter	Area (deg^2)	Prob. (%)	Lim. mag
GW151226	BBH	2015-12-26	2016-01-07	HSC-i	63.1	12	24.4
			2016-01-07	HSC-z	63.3	12	24.0
			2016-01-13	HSC-i2	63.1	12	24.4
			2016-01-13	HSC-z	63.2	12	24.0
			2016-02-06	HSC-i2	65.0	12	24.5
			2016-02-06	HSC-z	65.0	12	24.0
G275404[1]	BH–NS	2017-02-25	2017-02-27	HSC-z	26.0	0.5	23.2
GW170814	BBH	2017-08-14	2017-08-16	HSC-Y	32.5	35	22.2
			2017-08-17	HSC-Y	32.6	35	22.2
GW170817	BNS	2017-08-17	2017-08-18	HSC-z	26.2	61	21.7
			2017-08-19	HSC-z	27.3	61	21.6
S190510g	BNS[2]	2019-05-10	2019-05-10	HSC-Y	118.8	1.1	22.9
S191216ap	BBH[3]	2019-12-16	2019-12-20	HSC-z	2.3	0.035	25.2
S200224ca	BBH	2020-02-24	2020-02-25	HSC-r2	57.8	80.8	25.3
				HSC-z	57.8	80.8	23.6
			2020-02-28	HSC-r2	57.8	80.8	24.6
				HSC-z	57.8	80.8	23.2
			2020-03-23	HSC-r2	57.8	80.8	25.5
				HSC-z	57.8	80.8	23.8

[1] Detected with low-latency pipeline but not recovered with the offline analysis.
[2] Initially reported as BNS with a high probability but could be terrestrial noise.
[3] Initially reported as Mas Gap object but later classified as BBH.

3.3.3. Advances in theoretical models

The observed properties of AT2017gfo are consistent with expectations from numerical relativity simulations [269]. In particular, to have an ejecta component with a moderate lanthanide fraction, at least the temporary presence of a hypermassive neutron star is suggested. If the merger results in a prompt collapse to a BH, there is no source of neutrino radiation, and thus almost all the ejecta are expected to be lanthanide-rich, which is not consistent with the observations. In this way, numerical relativity simulations play a crucial role in connecting the initial conditions estimated from GWs (mass and mass ratio) with the final outcome of kilonova.

Mass ejection from NS mergers can be roughly divided into two phases: (i) dynamical mass ejection mainly by the tidal force and shock interaction in the dynamical timescale, and (2) subsequent post-merger mass ejection from the accretion torus. Observations of GW170817/AT2017gfo highlighted the importance of post-merger mass ejection from NS mergers. However, detailed simulations have been difficult. We have performed long-term general relativistic neutrino radiation hydrodynamics simulations by taking into account the effects of viscosity [270]. We found that post-merger ejecta ($> 10^{-2} M_\odot$) dominate over the dynamical ejecta ($< 10^{-2} M_\odot$). Thanks to the inclusion of neutrino transfer, we could also provide the distribution of the electron fraction in the ejecta. We showed that the
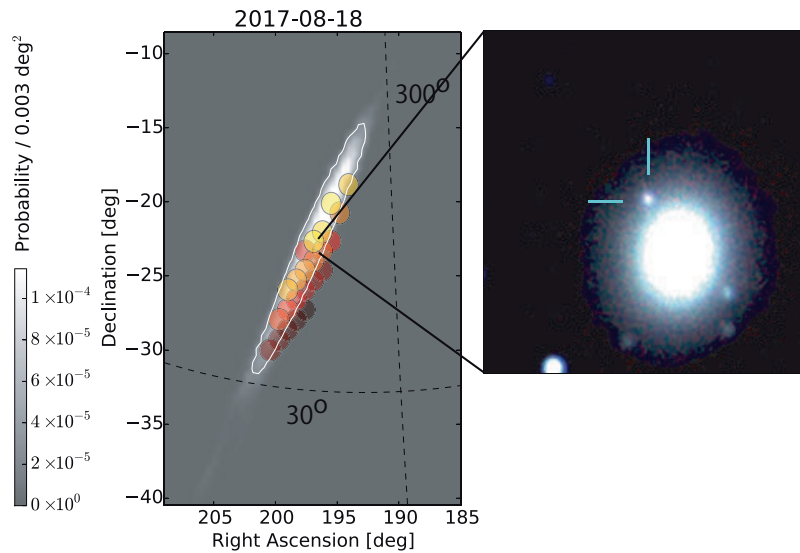
Fig. 21.   Left: Localization map of GW170817 and Subaru/HSC pointing [264]. Right: Three-color image of the counterpart of GW170817 [266].
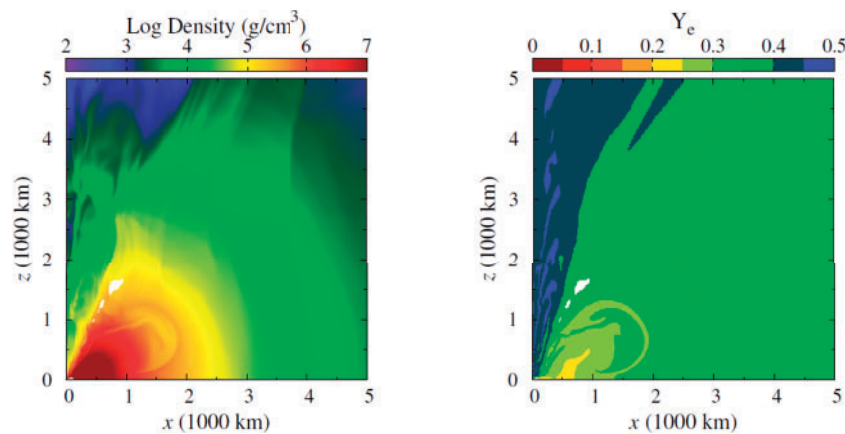
Fig. 22.   Density distribution and electron fraction distribution in the post-merger ejecta, obtained by viscous radiation hydrodynamics simulations [270].

ejecta have a high electron fraction (> 0.25), which means that post-merger ejecta is lanthanide-poor (Fig. 22).

Depending on the mass and mass ratio of the NS merger, various ejecta components with different properties (mass, velocity, and electron fractions) are expected. Therefore, it is important to study the observable outcome using the results of numerical relativity. We performed multi-dimensional radiative transfer simulations by consistently taking the interplay of multiple ejecta components into account [271]. We showed that AT2017gfo can be naturally explained by the geometry predicted by numerical relativity simulations (Fig. 23).

We then extended our radiative transfer simulations for various initial conditions. Using the updated atomic data [272], Ref. [273] showed that the properties of kilonova would be diverse, depending mainly on the total mass of the system. Since these were multi-dimensional simulations, we could also predict the variety of the luminosity for different viewing angles. It was shown that optical emission
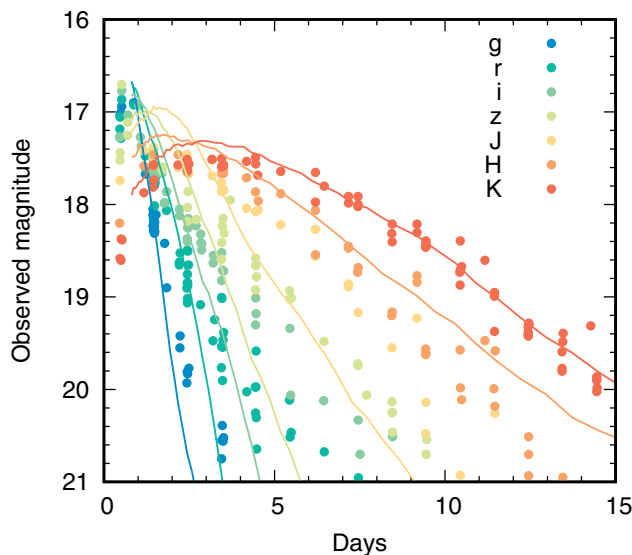
Fig. 23. Multi-color light curves of GW170817/AT2017gfo (circles) compared with the results of two-dimensional radiative transfer simulations (solid lines) [271,273].

is greatly suppressed when NS merger is observed from the equatorial plane, while infrared emission is almost unchanged. These simulations will be useful to facilitate future EM follow-up observations.

3.3.4. Future prospects

Our observational and theoretical results indicate that NS mergers synthesize a wide range of *r*-process elements. With the current estimate of the event rate and mass ejection, NS merger can explain the total amount of *r*-process elements in our Galaxy [3,4]. However, the event rate is still largely uncertain. Also, we still do not fully understand whether or not mass ejection is universal. Variation in mass ejection and nucleosynthesis are expected from the numerical simulations. Therefore, it is important to observe more NS mergers to accurately derive the event rate and to obtain a general picture of mass ejection and nucleosynthesis.

The sensitivity of GW detectors are still improving. In the third observing run (O3), the typical sensitivity corresponds to a range of NS merger up to 130 Mpc (LIGO Livingstone), 110 Mpc (LIGO Hanford), or 45 Mpc (Virgo). Thanks to these high sensitivities, two reliable GW events including at least one NS have been reported. However, due to the poor positional localization or large distances, no EM counterpart has been identified. We refer the reader to Ref. [274] for our observing effort in O3 The situation will be improved when the sensitivity of Virgo becomes comparable. Furthermore, when KAGRA joins the network with a comparable sensitivity, positional localization will be greatly improved (down to a few $\deg^2$ for signals such as GW150914 [275]).

Figure 24 shows the expected event number per year as a function of distance. Once the sensitivities of all the GW detectors reach $\sim$200 Mpc, we expect $>$ 10 events every year. Kilonova associated with such events is expected to be faint, $\sim$22 mag in optical within 2–3 d of the merger. Therefore, observations with Subaru/HSC will play an important role. Also, deep near-infrared imaging and spectroscopic observations with large-aperture telescopes, such as Subaru, Keck, Gemini, and the upcoming TAO 6.5 m telescope [276], will be important for firm identification of kilonova. Such multi-wavelength observations will provide us with unique information on *r*-process nucleosynthesis.
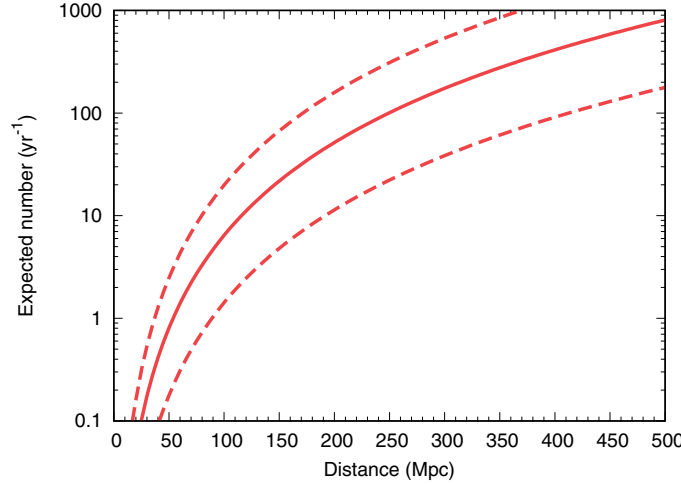
Fig. 24. Expected number of NS mergers as a function of distance assuming the event rate estimated from the O2 run [5]. The dashed lines show the range for the 90% confidence level.

4. Supernovae

4.1. GW signatures from core-collapse supernovae

4.1.1. CCSN GW signatures

Unlike the GW signals from compact binary coalescence, where a template-based search is best suited (see, e.g., Ref. [277]), gravitational waveforms from CCSNe are essentially of a stochastic nature. This is because the waveforms are affected by turbulence in the post-bounce core, which is governed by multi-dimensional nonlinear hydrodynamics. In order to clarify the GW emission mechanisms, extensive numerical simulations have been performed in different contexts (see, e.g., Refs. [278–285], and Ref. [286] for a review). For canonical supernova progenitors [287], core rotation is generally too slow to affect the dynamics [288,289]. For such progenitors, GW emission takes place in the post-bounce phase, which is characterized by prompt convection, neutrino-driven convection, proto-neutron star (PNS) convection, the standing accretion shock instability (SASI) [290], and the $g(/f)$-mode oscillation of the PNS [285,291–295].

The most generic GW emission feature seen in recent self-consistent 3D CCSN models is from PNS oscillation [296–299]. The characteristic GW frequency increases almost monotonically with time due to accumulating accretion to the PNS, and ranges from $\sim$100 to 1000 Hz. On the other hand, the typical frequency of SASI-induced GW signals is concentrated in the lower frequency range of $\sim$100 to 260 Hz and persists when SASI dominates over neutrino-driven convection [297–300]. The detection of these distinct GW features is considered as the key to inferring which one is more predominant in a pre-explosion supernova core, i.e. neutrino-driven convection or SASI [297].

Shown in Fig. 25 is an example waveform taken from a 3D CCSN simulation in Ref. [298]. For the model, the hydrodynamics evolution is self-consistently followed in full GR, starting from the onset of core collapse for a 15 $M_\odot$ star [301], through core bounce, up to $\sim$350 ms after bounce. Consistent with the outcomes from recent 3D models [297,299], the hydrodynamic evolution and the associated GW waveform are characterized by a prompt convection phase shortly after bounce ($T_{\rm pb} \lesssim 20$ ms, with $T_{\rm pb}$ the post-bounce time, shown simply as "time" in Fig. 25), then the linear (or quiescent) phase, which is followed by the non-linear phase ($T_{\rm pb} \gtrsim 140$ ms) when vigorous SASI activity (as well as growing GW amplitudes) was observed for the model (see Ref. [298] for more details). The
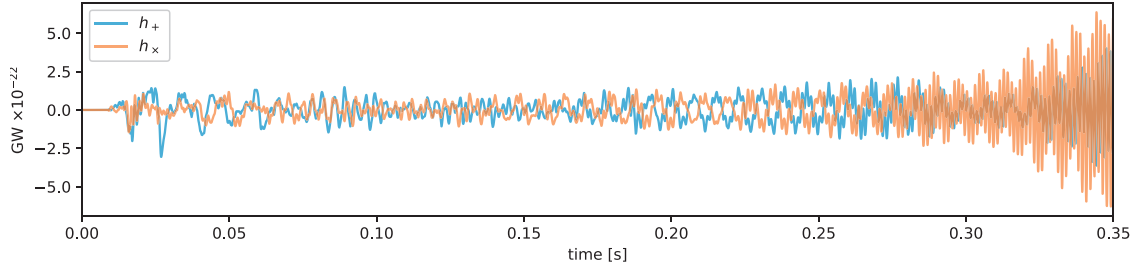
Fig. 25. An example gravitational waveform of the + (blue line) and × (orange line) mode from a 3D GR CCSN model of a $15\,M_\odot$ star (model SFHx in Ref. [298]). The time is measured after core bounce ($t = 0$). A source distance of 10 kpc is assumed. The waveform was extracted via a standard quadrupole formula with GR corrections [283]. Since the waveform is weakly dependent on the source orientation, an unbiased direction is chosen (e.g. from the north pole ($(\theta, \phi) = (0, 0)$)). This figure is taken from Ref. [302].

dominance of SASI over neutrino-driven convection persists over $140\,\mathrm{ms} \lesssim T_{\mathrm{pb}} \lesssim 300\,\mathrm{ms}$, after which neutrino-driven convection dominates over SASI.

In order to discuss the detectability of CCSN GW signals (as in Fig. 25), previous studies have traditionally relied on GW spectrogram analysis, aiming to specify the GW feature by the excess power in the time–frequency domain (by taking the square norm of the short-time Fourier transform). However, spectrogram analysis has a trade-off relation between the time and frequency resolution, leading to limited time–frequency localization. Because of this drawback, some features could have been potentially overlooked in previous spectrogram analysis in the context of CCSN GWs. Recent developments in time–frequency analysis (TFA) have yielded various time–frequency representation alternatives to the spectrogram. In particular, quadratic time–frequency representations, such as the Wigner–Ville distribution and its modified forms, enable us to perform high-resolution TFA [303–305].

Recently, the S-method utilizing the Wigner–Ville distribution was applied in Ref. [302] and successfully extracted several key (CCSN) GW features in the time–frequency domain (left panel of Fig. 26, where the waveform of Fig. 25 was used). In comparison with conventional TFA based on the Fourier transform (e.g. Fig. 1 in Ref. [298]), the S-method significantly improves the sharpness of the modes. Furthermore, by defining the instantaneous frequency (IF) of the excess in the time–frequency domain (corresponding to the bright-color regions in the left panel of Fig. 26; see Ref. [302] for more details), five modes (A B, C, $C^{\#}$, and D; see the right panel of Fig. 26) were identified.

Mode A in the right panel of Fig. 26 corresponds to the PNS $g(/f)$-mode oscillation, which is excited in the vicinity of the PNS surface by downflows and/or directly originates from the deceleration of infalling convective plumes [295]. Modes B and C are quasi-static modes, in the sense that these two modes barely change with time in the time–frequency domain. Mode B ($f_{\mathrm{B}} \sim 130\,\mathrm{Hz}$) originates from SASI; its frequency is twice the SASI frequency ($f_{\mathrm{SASI}} \sim 65\,\mathrm{Hz}$) because of the quadrupole nature of the GW emission (see also Ref. [300]). Mode D is an overtone of mode B ($f_{\mathrm{D}} \approx 2f_{\mathrm{B}}$), which most likely comes from the PNS core oscillation (see Fig. 8 in Ref. [302]). Mode C intersects with mode A at $T_{\mathrm{pb}} \sim 180\,\mathrm{ms}$, after which this mode is denoted as $C^{\#}$. Although yet to be investigated in detail, modes C and $C^{\#}$ are likely to arise in the innermost region ($\sim 10\,\mathrm{km}$) [306]. Note that the typical frequency of SASI-induced GWs is in the range ~ 100–$260\,\mathrm{Hz}$ (e.g. modes B and D in the left panel of Fig. 26), which is in the best sensitivity range of the currently running interferometers. For a Galactic event, the SNR of the GW signals predicted in the most recent 3D CCSN models was estimated in the range ~ 4–10 for Advanced LIGO [297]. With the third-generation detectors on line
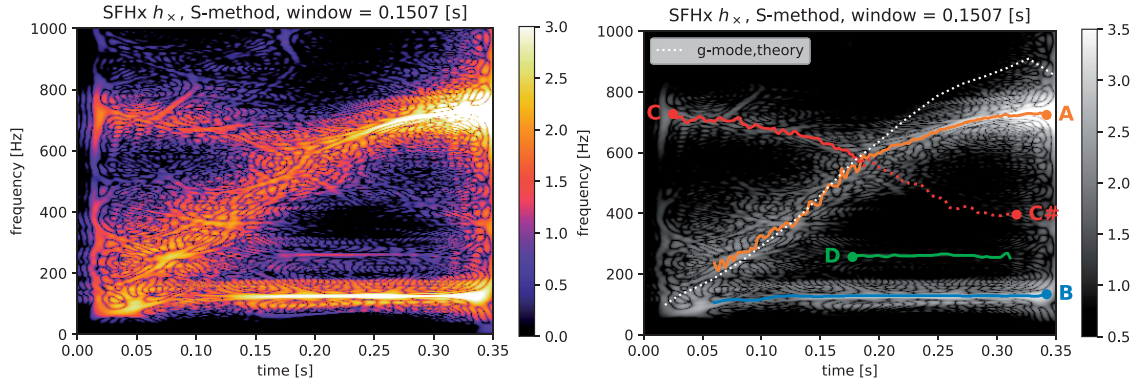
Fig. 26. The left panel is the time–frequency representation of the sample waveform (Fig. 25), extracted by the S-method. The right panel shows the GW mode identification of the spectrogram based on the instantaneous frequency identification method via the S-method (see Ref. [302] for more details). In the right panel, the white dashed line represents the theoretical prediction of the peak GW frequency of the PNS *g*-mode oscillation [295]. Note that the deviation of mode A from the white dashed line (especially in the later post-bounce phase) was previously observed in the literature [285,297]. These figures are taken from Ref. [302].

(e.g. Cosmic Explorer and the Einstein Telescope), these signals would never be missed for CCSN events throughout the Milky Way.

4.1.2. *Circular polarization of CCSN GWs*

Recently, yet another GW feature has been reported: the circular polarization of CCSN GWs. The importance of detecting GW circular polarization was first pointed out in Ref. [307] in the context of rapidly rotating core collapse. More recently, Ref. [308] presented analysis of GW circular polarization using results from the core collapse of a non-rotating $15\,M_\odot$ star [298], the waveform of which is shown in Fig. 25.

Figure 27 visualizes the time evolution of the GW circular polarization (CP) in the models SFHx (left panel) and TM1 (right panel) from Ref. [308]. Note that SFHx [309] and TM1 denote the nuclear EOS employed in the 3D GR simulation [298]. The key difference is that the softer EOS (SFHx) makes the PNS radius and the shock radius at the shock-stall more compact than TM1. This leads to much stronger SASI activity for SFHx compared to TM1.

In fact, one can see a clearer polarization signature for SFHx (left panel of Fig. 27) characterized by the bigger GW amplitude with the right-handed (red line) and left-handed modes (blue line) than for TM1 (right panel). Note that in each panel the two SASI-dominant phases of SFHx are colored red or blue (see also the bottom panels of Fig. 1 in Ref. [308]). The non-axisymmetric flows associated with spiral SASI give rise to the circular polarization. Before $T_{\rm pb} \sim 140\,{\rm ms}$, the CP is small because the SASI activity is still weak. But, after $T_{\rm pb} \sim 140\,{\rm ms}$, when the (spiral) SASI activity begins to be vigorous [298], the right-handed CP first emerges, followed by the left-handed CP (the blue line) until $T_{\rm pb} \sim 320\,{\rm ms}$, after which neutrino-driven convection dominates over SASI.

To explore the detectability of CP, Monte Carlo simulations of coherent network analysis [310] were performed for the signal reconstruction, where the network of LIGO Hanford, LIGO Livingston, VIRGO, and KAGRA was considered. They reported enhancement of the SNR of the GW circular polarization ($\mathrm{SNR_{CP}}$) relative to that of the GW signal itself ($\mathrm{SNR_{TF}}$). Although this is likely because the Gaussian noise has a small component for the circular polarization, more detailed analysis is
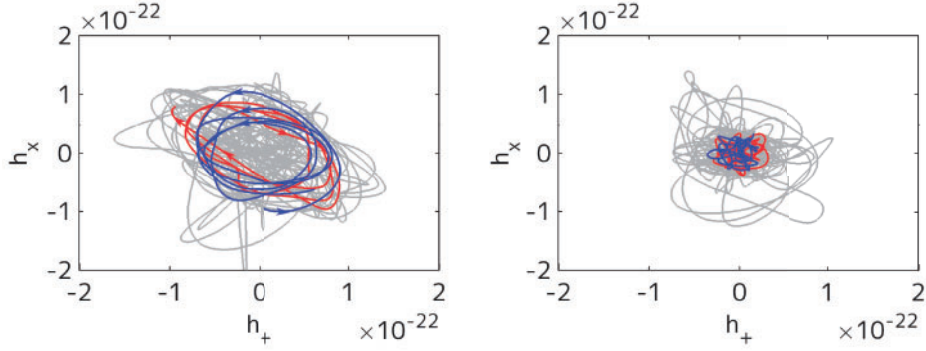
Fig. 27. Trajectories of GW circular polarization on the h_+–$h_\times$ plane of models SFHx (left panel) and TM1 (right panel) of 3D GR simulations using different equations of state (see text). The two characteristic epochs with right-handed (140 ms $\lesssim T_{pb} \lesssim$ 200 ms) and left-handed (220 ms $\lesssim T_{pb} \lesssim$ 320 ms) polarization are highlighted with red and blue colors. The gray line denotes the whole trajectory during the simulation time. The source distance is assumed at 10 kpc. These figures are taken from Ref. [308].

required to draw a robust conclusion as to whether or not GW CP could provide a new probe to clarify CCSN inner workings such as SASI and PNS oscillations (see Ref. [308] for more detail).

4.1.3. Rapid rotation: GW and neutrino signals from an exploding $27\,M_\odot$ star

Rapid rotation in the iron core (with an initial rotation frequency typically greater than 0.5 rad s^{-1}) leads to significant rotational flattening of the collapsing and bouncing core, which produces a time-dependent quadrupole (or higher) GW emission (see, e.g., Ref. [311] for a review). For the bounce signals to have a strong and characteristic signature, the iron core must rotate rapidly enough.[1] The GW frequency associated with rapidly rotating collapse and bounce is in the range $\sim$600–1000 Hz [278]. A current estimate based on a coherent network analysis using predictions from a set of 3D models shows that these GW signals could be detectable up to $\sim$20 kpc for the most rapidly rotating model [310]; see also Refs. [313,314].

Figure 28 shows the neutrino and GW signals [315] obtained in a 3D core-collapse supernova simulation of a rapidly rotating $27\,M_\odot$ star that is exploding due to the growth of the so-called low-T/$|W|$ instability [288]. The time modulation seen in the left panel corresponds to the neutrino lighthouse effect where the spinning of strong neutrino emission regions around the rotational axis leads to quasi-periodic modulation in the neutrino signal. Depending on the observer's viewing angle, the time modulation will be clearly detectable in IceCube and the future Hyper-Kamiokande. The GW emission is also anisotropic where the GW signal is emitted, as previously identified (see Ref. [286] for a review), most strongly toward the equator at rotating core collapse and bounce, and the non-axisymmetric instabilities in the post-bounce phase lead to stronger GW emission toward the spin axis. The right panel of Fig. 28 shows that these GW signals can be a target of LIGO-class detectors for a Galactic event. The origin of the post-bounce GW emission (e.g. the bar-mode ($m = 2$) deformation of the PNS due to the low T/$|W|$ instability) naturally explains why the peak GW frequency is about twice the neutrino modulation frequency. These results demonstrate that the

---

[1] Although rapid rotation and the strong magnetic fields in the core are attracting great attention as the key to solving the dynamics of collapsars and magnetars, one should keep in mind that recent stellar evolution calculations predict that such extreme conditions can be realized only in a special case [312] ($\lesssim$1% of the massive star population).
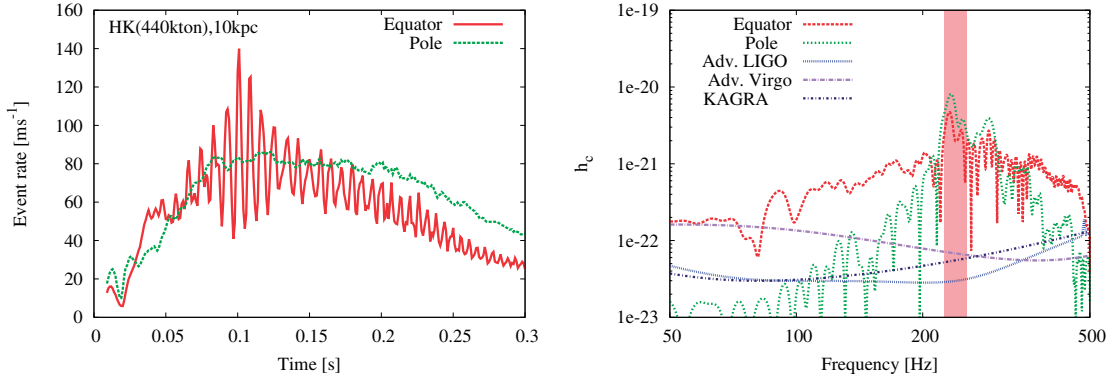
Fig. 28. The left panel shows detection rates of $\bar{\nu}_e$ at 10 kpc for a rapidly rotating $27\,M_\odot$ model as a function of time after bounce [315]. The red and green lines correspond to the event rates (per 1 ms bin) for an observer along the equator and the pole (e.g. parallel to the rotation axis), respectively. A quasi-periodic modulation (red line) corresponds to ~ 120 Hz (red lines) seen for the observer along the equator. The right panel shows characteristic GW spectra relative to the sensitivity curves of Advanced LIGO, Advanced Virgo [316], and KAGRA [317]. The peak GW frequency (the vertical red band) is about twice the neutrino modulation frequency.

simultaneous detection of rotation-induced neutrino and GW signatures could provide a smoking-gun signature of a rapidly rotating PNS at the birth (see also Refs. [318,319]).

4.1.4.   *Hydrodynamics and GW signals from a BH-forming massive star*

Successful observations of GWs from BBHs by the LIGO and VIRGO collaborations are now posing a new challenge: what is the origin of the massive BHs? One of the most plausible scenarios is binary stellar evolution in a low-metallicity environment (see Ref. [6] for a review). It has been proposed that two massive stars in the approximate range of 40 to $100\,M_\odot$ lead to the formation of a massive helium core after experiencing the Roche-lobe overflow and common envelope phase (see, e.g., Refs. [320–322] and the references therein). The gravitational collapse of the massive core ($\sim 30\,M_\odot$) could account for some of the relevant BH mass ranges (at least at the high-mass end) in GW events, although the formation path to the massive core and further to the BH is still very uncertain due to the complexity of binary evolution and the fallback dynamics [323].

In order to clarify the BH formation process, one requires 3D GR neutrino radiation-hydrodynamics core-collapse simulations of such massive stars. Due to the high numerical cost, most previous studies with BH formation have been done assuming spherical symmetry (1D; see Refs. [25,27] and the references therein). In the context of multi-dimensional simulations with multi-energy neutrino transport, Ref. [324] reported one- and two-dimensional (2D) core-collapse simulations of a solar-metallicity $40\,M_\odot$ star using a two-flavor IDSA scheme [325] and post-Newtonian gravity to include GR effects. More recently, a BH-forming 3D GR simulation of a zero-metallicity $40\,M_\odot$ star with an approximate neutrino transport (FMT) scheme was reported in Ref. [326]. It is only recently that the first 3D GR simulation (using a $70\,M_\odot$ star [327]) with detailed neutrino transport [328] following the dynamics up to BH formation was published [329]. In the simulation, the evolution hydrodynamic equations are solved based on the Baumgarte–Shibata–Shapiro–Nakamura formalism [330,331], and the evolution of the neutrino radiation field based on the multi-energy M1 scheme [329]. Casting a helium core of $\sim 31\,M_\odot$, a zero-metallicity $70\,M_\odot$ star was chosen as one possible progenitor candidate for BBHs.
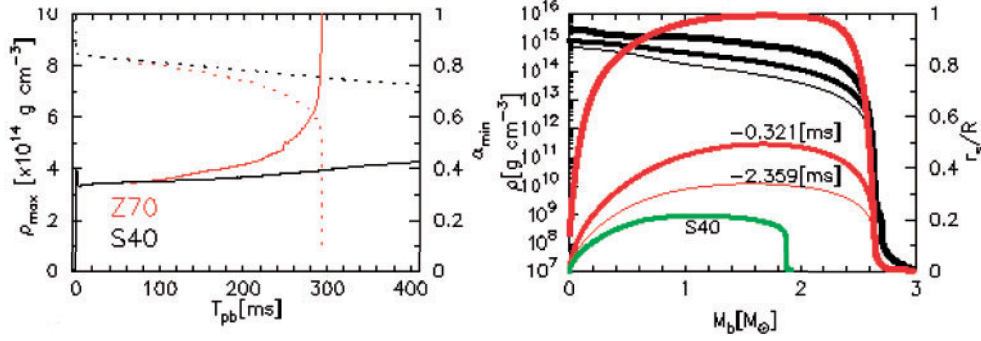
Fig. 29. The left panel shows the time evolution of the maximum rest-mass density (solid line) and minimum lapse function (dotted line) for a $70\,M_\odot$ star (denoted as Z70, red line) and a $40\,M_\odot$ star (S40, black line). The right panel shows angle-averaged profiles of the (rest-mass) density (black line) and the ratio r_s/R (red lines, see text) for Z70 as a function of the enclosed baryon mass for three representative time slices near the final simulation time. The -0.321 and -2.359 ms labels denote the time before the final simulation time ($T_{\rm fin} = 293$ ms after bounce). The green line corresponds to r_s/R for S40. These figures are from Ref. [329].

The left panel of Fig. 29 shows the temporal evolution of the maximum density $\rho_{\rm max}$ (solid lines) and the minimum lapse $\alpha_{\rm min}$ (dotted lines) for the $70\,M_\odot$ star (denoted as Z70, red line) and the $40\,M_\odot$ star (S40, black line). Note that S40 is shown for comparison with previous results. The compactness parameter of S40 is much smaller ($\xi_{2.5} \sim 0.26$) than that of Z70. The maximum density at bounce ($\rho_{\rm max} \sim 4 \times 10^{14}\,{\rm g\,cm}^{-3}$) is quite similar between Z70 and S40. After bounce, the increase in the maximum density of Z70 (red solid line) is significantly faster than for S40 (black solid line). For both Z70 and S40, the minimum lapse (dotted lines) shows a gradual decrease after bounce. At around $T_{\rm fin} = 293$ ms after bounce, it shows a drastic drop to $\alpha_{\rm min} = 0.0645$ for Z70, indicating that the PNS core starts to collapse rapidly toward BH formation.

The right panel of Fig. 29 explains how $T_{\rm fin}$ is related to the BH formation time. Shown in the panel are the profiles of the (angle-averaged) density (black lines) and a diagnostic to measure BH formation as a function of the enclosed baryon mass $M_{\rm b}$ at some representative snapshots near $T_{\rm fin}$ for Z70 (red lines) and at $T_{\rm pb} = 400$ ms for S40 (green line). As a BH formation diagnostic the ratio of r_s/R is shown, where r_s and R denote the Schwarzschild radius and the radial coordinate, respectively. One can see that the maximum r_s/R is ~ 0.3 at 2.359 ms before $T_{\rm fin}$ (the thin red line labeled "-2.359 [ms]") and rapidly increases with time, approaching unity (precisely, 0.932) at $T_{\rm fin}$ (thickest red line), which was judged as the epoch of BH formation in Ref. [329]. It should be noted that for an unambiguous definition of BH formation, one requires the implementation of a so-called apparent horizon finder [332] in the numerical relativity simulation, which remains as future work.

At the (fiducial) BH formation time, the mass and radius are $M_{\rm b(g),BH} \sim 2.60\,(2.51)\,M_\odot$ and $R_{\rm iso} \sim 4$ km, respectively. By contrast, S40 shows a significantly less compact structure (green line) at the final simulation time ($T_{\rm pb} = 400$ ms). The BH formation should occur much later, possibly when the mass shell at $R(M_{\rm b} = 2.6\,M_\odot) \sim 10^9$ cm accretes to the stalled shock. Using the same EOS (LS220 [333]), this expectation is in line with Ref. [324], which reported BH formation at $T_{\rm pb} \sim 700$ ms, and with Ref. [326], at $T_{\rm pb} \sim 1$ s.

The time evolution of the (angle-averaged) shock radius $R_{\rm s}$, the gain radius $R_{\rm g}$, the ratio of the advection timescale to the neutrino-heating timescale in the gain region $\tau_{\rm adv}/\tau_{\rm heat}$, and the mass in the gain region $M_{\rm gain}$ are presented in Fig. 2 of Ref. [329]. For model Z70, the shock revival was obtained after $T_{\rm pb} \gtrsim 260$ ms. At this time, the maximum temperature in the core becomes as high as $T \sim$
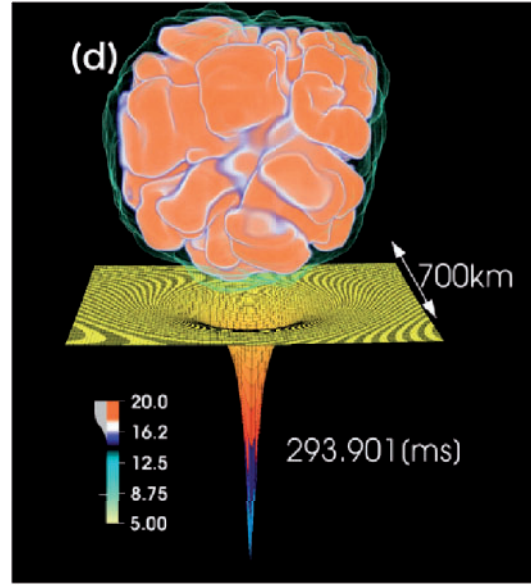
Fig. 30. A snapshot of the entropy distribution (k_B baryon^{-1}) for Z70 at $T_{pb} \sim 294$ ms, just before BH formation [329]. The sheet represents the lapse function (α) on the $z = 0$ plane. This figure is taken from Ref. [329].

100 MeV at a slightly off-center region at $R_{iso} \sim 10$ km (equivalently at $M_b \sim 1.0 \, M_\odot$). Subsequently the high-temperature region propagates outward in the mass coordinate, although spatially inward, due to the continuous mass accretion. The maximum temperature reaches ~ 170 MeV at $R_{iso} \sim 1$ km ($M_b \sim 1.4 \, M_\odot$) just before T_{fin}. In this second collapse phase to the forming BH, the high neutrino emission makes the heating timescale shorter than the competing advection timescale in the gain region. Aided by strong convection behind the shock, the stalled shock is revived at $T_{pb} \gtrsim 260$ ms ($\tau_{adv}/\tau_{heat} \geq 1$). This also results in an increase in the gain mass (see the blue line) due to the shock expansion.

Figure 30 visualizes a 3D hydrodynamics feature near BH formation. During the first ~ 160 ms after bounce, the neutrino heating is still weak and high-entropy bubbles are yet to appear. Only after $T_{pb} \gtrsim 230$ ms is the formation of high-entropy plumes ($s \gtrsim 15 \, k_B$ baryon^{-1}) seen due to the intense neutrino heating from the hot PNS. At this time, the mass in the gain region M_{gain} also starts to increase. Expansion of the (merging) high-entropy plumes is observed, leading to the shock revival. The lapse function shows the steepest drop in the center (see the cusp in the plane of Fig. 30), which corresponds to BH formation. By expanding the shock radius into the spherical harmonics, we find that the deviation of the shock from spherical symmetry (in the low modes, $\ell = 1, 2$) is less than $\sim 2\%$. This clearly indicates that neutrino-driven convection dominates over SASI in this case.

Finally, Fig. 31 shows the GW prediction for the Z70 star. The waveform is extracted along the positive z-axis via the quadrupole formula. The GW amplitude (multiplied by the distance to the source) stays at a small value ($\lesssim 10$ cm) before the shock expansion occurs ($T_{pb} \sim 260$ ms). The strong GW emission thereafter mainly originates from strong convection motion behind the shock. Just before the final simulation time, the GW amplitude reaches ~ 100 cm, though only for a short time. Although more quantitative discussion is apparently needed, a rough estimate shows that the GW signal could be targeted by third-generation GW detectors such as the Einstein Telescope (ET) and the Cosmic Explorer (CE) [430,431] for a source distance of less than ~ 1 Mpc. Regarding the neutrino signals, both electron-type (anti-)neutrinos show a decreasing and plateau trend for $T_{pb} \gtrsim 260$ ms, whereas heavy-lepton neutrinos show a rapid increase in both luminosity and
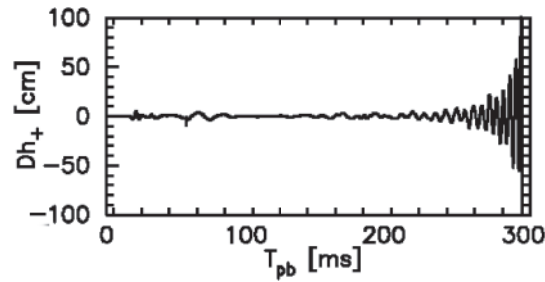
Fig. 31. Gravitational waveform for the BH-forming core collapse of a $70 \, M_\odot$ star. Note that h_+ and D denote the GW amplitude of the $+$ polarization and the distance to the source, respectively.

energy. These features are consistent with those previously identified in 1D full GR simulations with Boltzmann neutrino transport [334], and are due to the rapid contraction of the PNS to the forming BH (see also Refs. [335,336]). The detection of the short-lives (~ 300 ms after bounce) neutrino signals are basically limited to Galactic events (see Ref. [32] for a review). However, further study is needed to clarify the contribution of these BH-forming massive stars to the prediction of diffuse neutrino supernova background (see, e.g., Refs. [337,338]).

4.1.5.   Short summary and future prospects

To summarize, each phase of a CCSN has a range of characteristic GW signatures and GW polarization that can provide diagnostic constraints on the evolution, the physical parameters of the CCSN, and on the explosion hydrodynamics. The GW signatures described in this section commonly appear in the frequency range 100–1000 Hz in recent CCSN simulations. Among them, the PNS oscillatory modes are currently recognized as a model-independent GW signature. The characteristic frequency ($f_p \propto M/R^2$) of the fundamental (f/g) modes is predominantly dependent on the PNS mass (M) and the radius (R) [339]. In order to break the degeneracy, the detection of other eigenmodes (p, w modes) of the PNS oscillations is mandatory. In fact, GW asteroseismology of PNSs has just started [340–342], the outcomes of which should reveal the requirement for the next-generation detectors to detect all of the eigenmodes (presumably extending up to several kHz) for future CCSN events.

SASI-induced GWs for a Galactic supernova source are predicted to be detectable by Advanced LIGO with an SNR in the range ~ 4–10 by the most recent 3D CCSN models [297]. With the third-generation detectors (e.g. Cosmic Explorer and the Einstein Telescope) online, these signals would never be missed for CCSN events throughout the Milky Way. A current estimate of the SNR for GWs from rapidly rotating collapse and bounce based on predictions from a set of 3D models using coherent network analysis shows that these GW signals could be detectable up to ~ 20 kpc for the most rapidly rotating model [310]; see also Refs. [313,314]. See Ref. [343] for a more comprehensive recent review regarding the detectability of CCSN GW signals by future detectors.

After decades of progress, CCSN theory is finally converging, but not without detailed numerical effort and much theoretical sweat. We do have to raise a note of caution, however, that the current numerical results and the associated GW predictions that we have reported here will improve with the next-generation calculations by which more sophistication can be provided not only in the neutrino transport schemes (such as Boltzmann transport [344–346]), but also in the treatment of GR with BH formation. Therefore, we provide here only a snapshot of the moving (long-running) documentary film that records our endeavours to make our dream of "GW astronomy of the next Galactic CCSN" come true.

4.2. Understanding supernovae via neutrino emissions

One of the primary sources of near-field GWs, CCSN explosions are among the most dramatic and important events to take place in the universe. Agents of great destruction—anything within tens of light-years is utterly annihilated by the dying star—they are nevertheless responsible for the existence of life itself, for they (and the collisions of neutron stars they produce) are the sole source of all elements heavier than helium. Therefore, understanding these complex explosive events is necessary if we are to understand why we are here, and why the universe looks the way it does today.

Supernova neutrinos, famously observed from SN1987A, provide a unique and vital probe into the inner dynamics of these events. Released together with GWs during the initial stellar collapse, neutrinos and GWs are both certain to travel through any obscuring dust or gas and remain undiminished upon their arrival at the Earth. Neutrinos also carry information regarding the end state of the star: for explosions within our Galaxy, collapses into neutron stars or black holes, the eventual sources of far-field GWs, can be differentiated via observations of neutrino emissions.

Our goal is to make theory and experiment work together so that we will be ready to make the best possible observations of the next Galactic explosion and maximize our extraction of information concerning the explosion mechanism, progenitor, and nuclear physics ingredients.

In order to both predict and make sense of the neutrino signals from the next explosion in the Milky Way, the world's most advanced supernova numerical simulations are needed. Using nuclear data such as EOS and neutrino reactions, and by solving the 6D Boltzmann equation in 2D/3D, we can provide detailed predictions of the time distribution and energy spectra of supernova neutrinos.

To verify these complex computational models, we will enrich the famous Super-Kamiokande (SK) detector with gadolinium (Gd) salt. Doing so will turn it into the world's most advanced supernova neutrino detector, capable of real-time tagging and identification of individual supernova neutrino interactions with nanosecond-scale time resolution. This will make the diffuse supernova neutrino flux from all past supernova explosions visible for the first time. Starting around the middle of 2020, a gadolinium-loaded SK will collect a steady stream of supernova neutrino data, the first such new data in over 30 years.

The new experimental measurements made possible by gadolinium will then be fed into the theoretical models, testing their predictions using real supernova neutrino data and allowing us to better prepare for the next nearby supernova explosion. The models will be refined as needed and as indicated by the past supernova data. The gadolinium loading of SK will also greatly improve the detector's response to a nearby supernova. Therefore, both experimentally and theoretically, we will be well prepared for it.

4.2.1. SK-Gd

Water Cherenkov detectors such as Kamiokande, IMB, and SK have been used for decades as effective detectors for neutrino interactions and nucleon decay searches. While many important measurements have been made with these very large detectors, a major drawback has been their inability to efficiently detect the presence of thermal neutrons.

If a water Cherenkov detector could be improved to observe the neutrons produced by the inverse beta process ($\bar{\nu}_e p \rightarrow e^+ n$), then backgrounds would be greatly reduced. As a result, supernova neutrinos from explosions 35 000 times more distant than SN1987A could be seen by an improved SK, covering 50% of the entire universe. Perhaps more important for less distant explosions, neutron tagging of inverse beta events would facilitate the deconvolution of a Galactic supernova's various

signals, allowing a much more complete interpretation of the physics of the burst. In coincidence with a GW signal, detailed information concerning the explosion's dynamics would become even more valuable.

The key is to add 0.2% by mass of a soluble gadolinium compound like gadolinium sulfate, $Gd_2(SO_4)_3$, to the water. Doing so will make >90% of the neutrons visible as a consequence of the gamma-rays released by gadolinium's capture of thermalized neutrons. This technique and the various new scientific advances it would make possible were first proposed in the *Physical Review Letters* article "GADZOOKS! Anti-neutrino spectroscopy with large water Cherenkov detectors" [354]. The publication of this paper introduced the concept of gadolinium-enhanced water Cherenkov detectors, a transformational technology with a strong impact on the physics community. It provided a clear and cost-effective path to extending and building on the pioneering Kamioka work of years past.

In order to test this new technology, a dedicated gadolinium research and development facility was built in 2009 in the Kamioka mine near SK. Called EGADS (Evaluating Gadolinium's Action on Detector Systems) [355], it consists of a gadolinium-loaded 200 ton scale model of SK, complete with 240 50 cm photomultiplier tubes, its own DAQ and readout electronics, a novel selective water filtration system, and water transparency evaluation equipment. Based on its successful operation, in 2015 the SK Collaboration formally approved the plan to add gadolinium to SK, designating this new phase of the experiment "SK-Gd." The T2K Collaboration, a long-baseline neutrino oscillation experiment based at J-PARC which uses SK as their far detector, formally approved the gadolinium-loading plan in 2016.

In order to prepare SK for the addition of gadolinium, the detector had to be opened and refurbished for the first time in 12 years. There were four main tasks:

(1) Replace the photomultiplier tubes that had failed (a few hundred out of 13 000) since the previous in-tank refurbishment in 2006.
(2) Fix a small water leak in the SK tank.
(3) Clean any rust and other dirt that had accumulated in the detector since its original completion in 1996.
(4) Install additional water piping to increase the total water flow for increased water purification, and to enable better control of the flow direction in the tank.

This in-tank work, which required over 3000 person-days of effort, was successfully carried out between May 2018 and January 2019. By February 2019 the detector had been refilled with pure water, and was ready for the addition of $Gd_2(SO_4)_3$. After taking the T2K beam schedule into account, the first gadolinium is now expected to go into the tank in mid-2020. By searching for the small but constant diffuse flux of neutrinos produced by all core-collapse explosions since the onset of stellar formation in the early universe, it is expected that by 2022 we will have collected the world's first additional supernova neutrinos since SN1987A.

4.2.2. *Theoretical studies of supernova explosion and neutrino emission*

In the remainder of this section we report on the progress of theoretical study of supernova neutrinos and their detection at SK, with the emphasis on detailed description of neutrino transfer and microphysics. In order to provide a prediction of supernova neutrino detections at SK with gadolinium loading, it was necessary to remove the uncertainties in numerical simulations describing the explosion mechanism and neutrino emission. One of the remaining uncertainties in supernova simulations

is neutrino transfer, which has been routinely treated with approximate methods in multi-dimensional simulations. We performed sophisticated numerical simulations of neutrino-radiation hydrodynamics based on a direct solver of the Boltzmann equation. The first-principle-type calculations enabled us to determine the final outcome of an explosion, provide a solid prediction of neutrino emissions, and evaluate the uncertainties of the microphysics such as the equation of state.

4.2.3.   Boltzmann radiation hydrodynamics simulation of core-collapse supernovae
We have performed several simulations using Boltzmann radiation hydrodynamics code in two and three dimensions. The details of the code are illustrated in Refs. [356–358]. Various nuclear EOSs, progenitor models, and rotational velocities are employed. Here, we show the important features of the obtained results.

First, we examined the effect of the nuclear EOSs [359]. We employed the Lattimer–Swesty (LS) EOS [360] and the Furusawa–Shen (FS) EOS [361]. The former (latter) EOS model employs the soft (hard) nuclear force model and the single nuclear approximation (nuclear statistical equilibrium treatment) for the nuclear composition. The progenitor model was the $11.2\,M_\odot$ progenitor model taken from Ref. [362]. The simulations with the different EOS models showed a significant difference: the LS model shows shock revival while the FS model does not (see the left panel of Fig. 32). A useful quantity for understanding the difference is the timescale ratio, which is defined as $\tau_{\mathrm{adv}}/\tau_{\mathrm{heat}}$, where $\tau_{\mathrm{adv}} := M_{\mathrm{gain}}/\dot{M}$ and $\tau_{\mathrm{heat}} := E_{\mathrm{gain}}/Q_{\mathrm{gain}}$ are the advection timescale and the heating timescale, respectively. The advection timescale is the timescale over which a fluid element flows through the gain region. The heating timescale is the timescale over which a fluid element is heated and becomes gravitationally unbound. The gain region is the region where the neutrino heating exceeds the cooling. Here, M_{gain}, $\dot{M}$, E_{gain}, and Q_{gain} are the mass in the gain region, the mass accretion rate, the total energy including the gravitational binding energy in the gain region, and the net neutrino heating rate in the gain region, respectively. If the timescale ratio exceeds unity, neutrino heating proceeds sufficiently fast and the explosion succeeds. The right panel of Fig. 32 shows that the timescale ratio of the LS model exceeds unity, while that of the FS model does not. Although $\dot{M}$, E_{gain}, and Q_{gain} are similar between the LS and FS models, M_{gain} for the LS model is larger than for the FS model. This is because the turbulence is stronger for the LS model. Indeed, the prompt convection is stronger for the LS model, and it enhances the neutrino-driven convection at the later stage. The stronger prompt convection in the LS model originates from the stronger photodissociation of the accreting nuclei: the accretion flow outside the shock in the LS model contains more heavy nuclei, and hence the energy consumed by the photodissociation of these nuclei is larger for the LS model. Therefore, the proper treatment of the nuclear composition of an EOS is important to assess the influence of EOSs on CCSNe.

Second, we investigated the effect of rotation [363]. The EOS employed and progenitor model were the FS EOS and the $11.2\,M_\odot$ model from Ref. [362]. The rotational velocity profile was the so-called "shellular" rotation profile: $\Omega(r) = 1\,\mathrm{rad\,s^{-1}}/(1 + (r/1000\,\mathrm{km})^2)$. However, the rotational velocity employed is too slow to affect the post-bounce dynamics, even though the velocity is almost the highest according to the current stellar evolution theory [364]: the shock radii and other dynamical features are similar between the rotating and non-rotating models. What is more interesting here is the momentum space distributions of neutrinos. Figure 33 shows the neutrino angular distributions in the laboratory frame outside the shock on the equator. In particular, the distribution of the high-energy neutrinos is tilted to the ϕ-direction. This is because matter rotates and drags the neutrino distribution to the rotational direction. This detailed angular distribution is only accessible by the
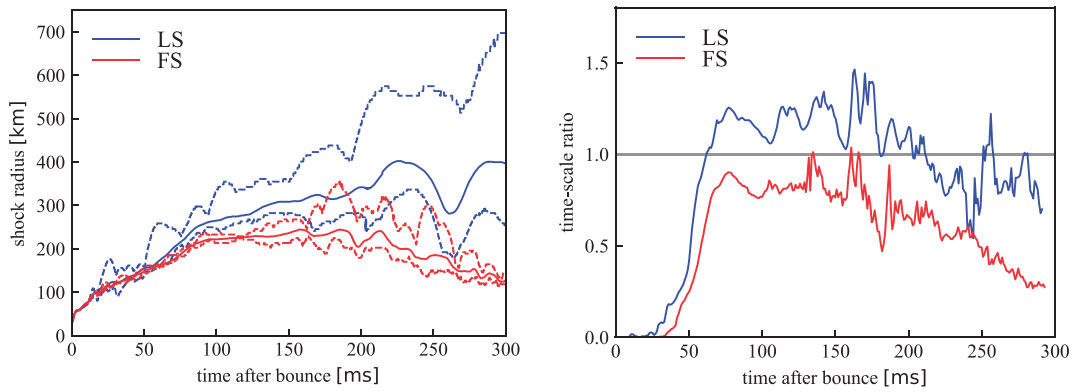
Fig. 32. (Left) The time evolution of the shock radii for the LS (red) and FS (blue) models. The thick solid lines are the angular-averaged shock radii, and the dashed lines show the ranges between the minimum and the maximum shock radii. (Right) The time evolution of the timescale ratio for the LS (red) and FS (blue) models.
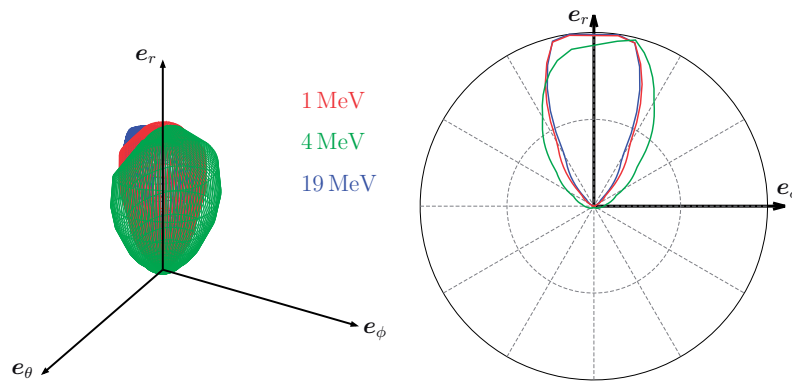
Fig. 33. The angular distributions of neutrinos outside the shock on the equator at 12 ms after bounce. The left panel shows the 3D distributions, and the right panel shows the sections by the r–ϕ plane. The different colors correspond to the different energies, as indicated in the left panel.

Boltzmann solver. Since we have such information, we can assess the accuracy of the M1-closure scheme, one of the approximate neutrino transport methods. The second angular moment of the distribution divided by the zeroth moment is called the Eddington tensor. The M1-closure scheme estimates the Eddington tensor from the energy flux and density of neutrinos. In Fig. 34, we compare the eigenvalues of the Eddington tensor calculated from the distribution function directly and the M1-closure scheme. The largest eigenvalue, or the Eddington factor, is ∼20% larger for the M1-closure scheme. This difference originates from the so-called ray collision between outward and inward rays. If we can get some information about these rays from neighboring matter, we may improve the accuracy of the M1-closure scheme.

Third, we suggested a new mechanism for the PNS kick motion [365]. We performed a core-collapse simulation with the 15 $M_\odot$ model of Ref. [362] and the Togashi–Furusawa (TF) EOS [366], one of the most realistic EOSs. The most interesting feature of this model is the PNS kick. Thanks to the exact treatment of thePNS in our code, the PNS moves with a velocity of $\mathcal{O}(10)$ km s^{-1}. So far, the driving force for PNS motion has been considered to be the gravity of the asymmetric ejecta [367]. However, the driving force observed in our simulation seems to be the recoil of the asymmetric
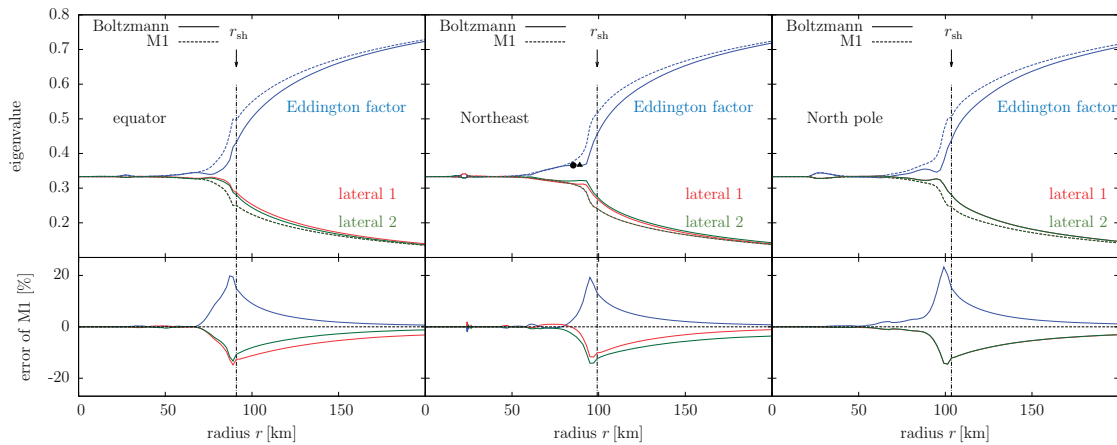
Fig. 34. The eigenvalues of the Eddington tensors calculated from the distribution function (solid) and the M1-closure scheme (dashed) in different directions at 12 ms after bounce. The largest eigenvalue is called the Eddington factor (red), and the other eigenvalues are named lateral 1 and 2 (blue and green). The upper row shows the eigenvalues themselves, while the lower row displays the fractional difference between the solid and dashed lines.

neutrino emission. With the PNS motion, the asymmetric distribution of neutrinos is sustained, and hence the driving force by the neutrinos persists. This result suggests the different mechanism of PNS motion.

Finally, we performed a 3D simulation with the Boltzmann radiation hydrodynamics code. Due to the limited computational resources, the dynamics and the neutrino distributions until ∼20 ms after the core bounce were investigated. With this simulation, a neutrino distribution function with no spatial symmetry was obtained for the first time in the world. This result provides important clues to understanding the behavior of neutrinos in supernovae.

4.2.4. *Light curve of supernova neutrinos*
In order to extract as much information as possible from the detection of supernova neutrinos from future supernovae, it is necessary to prepare templates of neutrino signals by systematically covering the variation of progenitors and microphysics. One such systematic set is the supernova neutrino database provided by Ref. [368]. This data is now routinely used to evaluate event rates at SK, replacing the classic dataset of Ref. [369].

The supernova neutrino database is constructed by combining supernova simulations for the set of progenitors with different masses and metallicities. Numerical general-relativistic neutrino radiation hydrodynamics code under spherical symmetry [370,371], which is a first-principle calculation, is utilized to study the series of phenomena: gravitational collapse, core bounce, formation of central object, shock propagation, and the associated neutrino emission. Numerical code for PNS thermal evolution with flux-limited neutrino diffusion in general relativity [372,373] is utilized to study the neutrino emission from the PNS cooling phase over 20 s. In order to connect the two stages, we take out the profile of the central object from the core-collapse simulation and continue the cooling simulation to simulate shock revival and the ceasing of accretion in the explosion.

We demonstrated the method to extract physics information from neutrino emissions of Galactic supernovae based on the supernova neutrino database and additional simulations [374]. We explored the time profile of neutrino detection events at SK for the set of progenitors with different masses and shock revival time. We provided the basic features of the rise and fall of the neutrino burst to extract

information on the core bounce of massive stars in the early phase within 0.3 s. We also explored the long-term behavior of the neutrino burst over 20 s up to the fading-out phase. We performed additional long simulations of PNS cooling in the case of light and massive neutron stars. We found that SK and Hyper-Kamiokande are able to detect the long-term evolution over 100 s for massive neutron stars in Galactic supernovae. We proposed a method to determine the mass of the central object by plotting the cumulative event number summed from the last event detection in a time-backward manner. These results are used as the basis to prepare for future supernova detections in order to determine the details of supernova mechanism and neutron stars. The dependence of the neutrino signals on the EOS is now in progress with the development of the EOS table for supernova simulations as described below.

4.2.5.   Information on supernova mechanisms from supernova neutrino detectors

The accumulation of predicted supernova neutrino signals will enable us to extract information on supernovae from the detection of neutrino bursts in the future [347,348]. SK will detect $\sim$10 000 neutrino events from supernovae in our Galaxy and provide valuable and unprecedentedly detailed information regarding the supernova mechanism. For nearby explosions, pre-supernova neutrinos from the silicon burning stage just before explosion will be studied by both KamLAND and the newly gadolinium-loaded SK.

Events from the dynamical phase will reveal hydrodynamical instabilities and rotation, augmented by detections at IceCube [315,349]. Observations of events from the cooling phase will clarify the birth of compact objects with mass and radius, which may constrain the EOS of dense matter [374].

Combined detection of GWs and neutrinos at KAGRA and SK would serve to unveil the supernova mechanism by their correlation [31,350]. The planned next generation of big detectors such as DUNE, JUNO, and Hyper-Kamiokande [351,352] with their extended supernova neutrino detection ranges can be expected to provide additional information (see Ref. [353] for further references).

Regarding multi-messenger astronomy, in the case of a Galactic supernova an early alert is possible since neutrinos are generated earlier in the explosion and therefore arrive before the electromagnetic radiation. Such an alert could be generated and disseminated either through large, directional, high-confidence detectors like the gadolinium-loaded SK acting independently to announce a burst, or a network of detectors which detect lower-confidence signals acting in coincidence [353] to reduce the chance of individual false alerts.

4.2.6.   Neutrino bursts from black hole formation

Studying the neutrino burst from black hole formation is an interesting target of SK among the variety of gravitational collapse scenarios of massive stars [375]. In the case of stars more massive than those of ordinary supernovae, 40–50 $M_\odot$ for example, with the intense accretion of matter from outer layers the retreat of the shock wave is inevitable and there is no chance of an explosion. The mass of the central object increases monotonically and attains the maximum mass that can be supported by the EOS. The black hole is formed due to the re-collapse of of the PNS at the critical mass. The neutrino signal in this case has a characteristic signature with a short duration, typically about 1 s, and increasing average energies and luminosities. This is caused by the increasing mass due to the accretion and the associated increase of density and temperature. This type of short neutrino burst can be a hallmark of black hole formation and can be used to constrain the EOS of hot and dense matter [376,377].

The detection of GWs and neutrino bursts from black hole formation may provide information on the central object and the EOS in addition to the case of core-collapse supernovae (see Sect. 4.1). We revealed the characteristic feature in the frequencies of GWs from the dynamical evolution of a PNS toward black hole formation. We analyzed the time evolution of accreting PNSs to determine the fundamental and gravity modes of GWs [378] by utilizing the results of numerical simulations of massive stars with a set of EOSs [375]. The density increase toward the black hole mass leads to a rise of GW frequencies as a function of the average density of the PNS. The ratio of the frequencies of the two modes can be characterized by the compactness of the PNS, therefore giving information on the mass and radius. Moreover, the termination of the neutrino signal can provide the timing of the black hole formation and information on the maximum density through combined analysis of GWs and neutrino signals.

4.2.7. Diffuse supernova neutrino background

Numerical simulations of supernova explosions and black hole formation from various massive stars are essential for detection of the diffuse supernova neutrino background, which is the main target of SK with the gadolinium loading. Numerical simulations of CCSNe in multiple dimensions (see also Sect. 4.1) and black hole formation as discussed above have been applied to provide integrated energy spectra of neutrino emissions from progenitors with a wide range of stellar mass. The features of a neutrino burst depend on the compactness of the massive stars, which in turn determines the accretion rate of matter and affects the neutrino emission. In the wide coverage of massive stars with different compactness, the case of black hole formation contributes to hard energy spectra due to the energetic bursts. Hence, the contribution of black hole formation for large compactness increases the event rates of the diffuse supernova neutrino background. Long-term observation at SK and Hyper-Kamiokande can provide constraints on the critical compactness and the ratio of black hole formation in various stellar collapse scenarios [379].

4.2.8. Equation of state for supernovae and neutron star mergers

The EOS is one of the important ingredients in CCSNe as well as neutron star mergers. It is also one of the remaining uncertainties in nuclear physics to determine the outcome of explosions, the birth of compact objects, and neutrino emission. In addition to the progress in numerical simulations of supernovae, developments in the data table of supernova EOSs for simulations have been made over the decades. One of the popular sets of supernova EOSs is the Shen EOS based on relativistic mean field theory [380–382], which has been applied to provide extended versions of the data table of supernova EOSs [383]. The Shen EOS table is publicly available on the web and has set the standard format for providing thermodynamical quantities for use by numerical simulations. The Shen EOS has been used in the numerical simulations for the supernova neutrino database.

Recently, the Shen EOS has been revised to improve the density dependence of the symmetry energy [384]. This modification was motivated by recent progress in observational data of neutron stars from GW detection and X-ray observations. The symmetry energy of the original Shen EOS, which was determined by fitting to nuclear masses and radii, has been claimed to be rather large as compared with other frameworks. Recent nuclear experiments also provide constraints on the behavior of the symmetry energy and help to improve its description. A new term of density-dependent isovector interaction in the relativistic mean field theory provides a smaller symmetry energy while keeping good properties of symmetric nuclei and matter. It also provides smaller neutron star radii within the observational constraints. The updated Shen EOS is now applied to numerical simulations of

CCSNe and PNS cooling. It has been recently shown that the influence of the updated Shen EOS at high densities mainly appears in the evolution of PNSs when the matter becomes neutron-rich, and remains minor in the dynamics around the core bounce. It will be interesting to see the influence of the full data table of the updated Shen EOS in CCSNe and neutron star mergers.

In addition to revisions of the nuclear interaction, improvements of the supernova EOS of hot and dense matter have been made to describe the mixture of nuclei under nuclear statistical equilibrium [385,386]. There has been recent progress on the construction of EOS tables by microscopic nuclear many-body theories such as the variational method and the Dirac–Brueckner–Hartree–Fock theory [387] (S. Furusawa et al., Prog. Theor. Exp. Phys., in press) based on the nucleon–nucleon interactions, being different from the effective nuclear many-body theories. In addition, the sets of EOS tables with systematic coverage of EOS parameters are under development and will be applied to the study of CCSNe and neutron star mergers. These developments will help the study of neutrino signals and GWs and to probe the dense matter in these astrophysical events.

4.2.9.   Supernova simulations on GPUs
The dynamics of supernovae are described by hydrodynamic equations for dense matter and the Boltzmann equation for neutrino transport under the gravitational effect described by the theory of general relativity. In addition to these coupled equations, data on physics processes such as sets of EOSs and reaction rates for neutrinos need to be implemented in the numerical simulations. Since the neutrino distribution is a function in six dimensions (three dimensions in space and three dimensions in neutrino momentum space), the required computational resources quickly increase with the grid resolution of these degrees of freedom. Therefore, numerical simulations of supernovae tend to challenge large-scale computational techniques and algorithms.

So far, most large-scale simulations have been performed on massively parallel clusters, such as the K computer. Recently, another type of architecture, which makes use of arithmetic accelerators such as GPUs, has become popular in high-performance computing. Although the accelerator device has an advantage in cost/performance, the code implementation becomes much more involved to achieve the desired performance. Furthermore, whether accelerators work efficiently depends strongly on the structure of the numerical algorithms.

Presumably for these reasons, the application of GPUs to CCSN simulations has been restricted. As for the simulation code including the neutrino transport, the VERTEX code was ported to GPUs by employing CUDA [388]. In the VERTEX code, the most time-consuming part is the calculation of the collision term of the Boltzmann equation, which exhausts almost half the simulation time. Offloading one dominant reaction process to GPUs achieved 1.8 times acceleration of the whole simulation time.

We developed an efficient scheme to exploit accelerator devices such as GPUs in numerical CCSN simulations [389,390]. As the first step, we applied the offloading of simulation bottlenecks to the computation of neutrino radiation hydrodynamics under spherical symmetry [371]. By adopting the implicit scheme for the evolution equation, an iterative linear equation solver for the coefficient matrix is the most time-consuming part. To offload this part to GPU devices, we employed OpenACC as an implementation framework as well as making use of the cuBLAS library that is available in NVIDIA's CUDA environment. We changed the data layout to maximize the efficiency of data transfer between the device memory and cores, in accordance with so-called coalesced access. With both OpenACC and cuBLAS, significant acceleration was achieved so that the linear equation solver is no longer a primary bottleneck [389].

The secondary bottlenecks of the original code were the computation of the collision term in the Boltzmann equation and the inversion of the block diagonal part of the coefficient matrix. The latter is required in the weighted Jacobi-type preconditioner for the iterative linear equation solver [391]. Offloading to GPU devices successfully accelerated these tasks [390]. For the inversion of block matrices, we employed a blocked version of the Gauss–Jordan algorithms [392] that is suitable for a many-core architecture. With these improvements, systematic simulations with better resolution have become feasible. Further optimization, as well as extension to 2D and 3D simulations, is underway. We are also implementing code for the PEZY-SC processor, another kind of accelerator device, by applying techniques developed for GPUs.

5.   Probes of new physics

5.1.   Test of gravity theories using gravitational wave data

5.1.1.   Varieties of gravitational waveform within general relativity

The GW signals from coalescing binaries can be decomposed into inspiral, merger, and ringdown waveforms.

Here we focus on the inspiral phase, in which the orbital frequency, and hence the GW frequency, gradually increases as the binary separation decreases. In the case that a binary with aligned spins evolves along a sequence of quasi-circular orbits, the inspiral waveform in the frequency domain can be approximately represented as

$$\tilde{h}(f) = \mathcal{A} f^{-7/6} e^{i\psi(f)}, \tag{12}$$

where the overall amplitude $\mathcal{A}$ is $\propto \mathcal{M}^{5/6}$, and

$$\psi(f) = 2\pi f t_c - \phi_c + \frac{3}{128} (\pi \mathcal{M} f)^{-5/3} \left[1 + \frac{20}{9} \left(\frac{743}{336} + \frac{11}{4}\eta \right) v^2 - 4 (4\pi - \beta) v^3 + \cdots \right] \tag{13}$$

in the post-Newtonian (PN) approximation [152]. Here, $\eta = \mu/M$ is the symmetric mass ratio, $v = (\pi M f)^{1/3}$ is the orbital velocity, and

$$\beta = \left(\frac{113}{12} - \frac{19}{3}\eta \right) \chi_{\text{eff}} + \frac{19}{6}\eta\sqrt{1 - 4\eta} \left(\frac{S_1}{m_1^2} - \frac{S_2}{m_2^2} \right) \cdot \hat{L}. \tag{14}$$

The second term on the right-hand side of the above equation becomes a small contribution because $\eta\sqrt{1 - 4\eta} \leq \sqrt{3}/18 = 0.096\ldots$, but we should note that this term can be dominant for spins antialigned with each other.

The first term in the square brackets of Eq. (13) is the term obtained by using Newtonian dynamics and the quadrupole energy loss formula due to GW emission. So, when we discuss the phase evolution, we count the PN order relative to this leading term. The second term is relatively $O(v^2)$, which we refer to as 1 PN order. In the following we summarize additional effects which should be carefully discriminated from modifications due to extensions of general relativity.

The effect of spins   The lowest PN effect of spins on the phase evolution appears at the 1.5 PN order. The effect depends only on the spin components projected in the direction parallel to the orbital angular momentum at this order, which is encapsulated in the coefficient β. When the spins are not aligned with the direction of the orbital angular momentum, spin precession occurs. As a result, amplitude modulation occurs, which helps to solve the degeneracy between spins and other

parameters [393]. The GW templates for precessing binaries are ready (see, e.g., Ref. [394] and references therein).

Eccentric binaries The orbital eccentricity decays like $e \propto a^{19/12}$ at the late stage of binary evolution, where a is the orbital semi-major axis [395]. Therefore, binaries are circularized well before they merge unless they are born with a close separation and a large eccentricity. One possible scenario to form binaries that maintain a sufficiently large eccentricity at the coalescence time is binary formation by capture in star clusters. Hence, detection of eccentricity would be useful to distinguish the formation channels of binaries that become GW sources. In the GW waveform, the effect appears most significantly in the phase evolution, unless the eccentricity is not extremely large. The correction appears in the phase evolution at $-19/6$ PN order. The minus sign of the PN order reflects the fact that the orbital eccentricity decays rapidly.

Dark matter cloud In the presence of dark matter, the waveform of GWs can be affected [396]. In the scenario of the existence of the dark matter mini-spike around an intermediate-mass black hole [397,398], the waveform of the GWs from an extreme mass ratio or intermediate mass ratio inspiral system is modified due to the effects of the gravitational pull, the dynamical friction, and the accretion of dark matter [399–401]. The possibility of measuring the power-law index of the dark matter mini-spike radial profile with space-borne GW detectors such as LISA has been shown (see also Ref. [402]). On the other hand, when the mass ratio is around $O(10^3) \sim O(10^4)$, energy dissipation due to the dynamical friction is comparable to the total binding energy of dark matter. If one considers a modification of the dark matter distribution due to the energy dissipation, the differences of the waveform from the vacuum case become much smaller, and even the spike has a large power-law index [403].

5.1.2. Model-independent test of waveform consistency with general relativity

From the inspiral waveform, we can determine the binary parameters. At the same time, we can test if there is no deviation from the standard waveform predicted for non-spinning quasi-circular binaries in GR. We can test the presence of spin and eccentricity of each binary component BH. At the same time, we can also test the deviation from the prediction of GR.

Here we summarize the test of GR performed by the LIGO/Virgo collaborations [35]. The first test was whether the residual data obtained by subtracting the best-fit template is consistent with the Gaussian noise. No inconsistency was observed.

They also performed a consistency test between the estimations of parameters obtained from the inspiral part and from the merger–ringdown part. Small-perturbation modes of a BH have their own frequencies and damping rates determined by its mass and spin. Those damped oscillation modes, called quasinormal modes (QNMs), are excited at the epoch of formation of the remnant BH after coalescence. See, e.g., Ref. [404] for a review of QNMs, including the history. Among various QNMs, the dominant mode is the fundamental ($n = 0$) mode with the harmonic $(\ell, m) = (2, 2)$, and the GW waveform is written as

$$h(t) = A e^{-(t-t_0)/\tau} \cos(2\pi f_R(t - t_0) - \phi_0), \tag{15}$$

where f_R is the oscillation frequency, τ is the damping time, and t_0 and ϕ_0 are the starting time and phase, respectively. A is the amplitude at the starting time. We can find information on f_R and τ, which are related to the mass $M_{\rm rem}$ and spin $a_{\rm rem}$ of the remnant BH, in Refs. [405,406].

As for the initial phase, we can maximize the SNR with an analytical method presented in Refs. [407,408], which is based on Ref. [409]. Since it is difficult to determine the starting time (e.g., see Ref. [410] for the estimation), the fractional differences

$$\frac{\Delta M_{\rm rem}}{\bar{M}_{\rm rem}} = \frac{2\left(M_{\rm rem}^{\rm insp} - M_{\rm rem}^{\rm post-insp}\right)}{M_{\rm rem}^{\rm insp} + M_{\rm rem}^{\rm post-insp}}, \qquad \frac{\Delta a_{\rm rem}}{\bar{a}_{\rm rem}} = \frac{2\left(a_{\rm rem}^{\rm insp} - a_{\rm rem}^{\rm post-insp}\right)}{a_{\rm rem}^{\rm insp} + a_{\rm rem}^{\rm post-insp}} \qquad (16)$$

between the quantities for the inspiral and the post-inspiral phases were used as an inspiral–merger–ringdown consistency test for BBHs in Ref. [35]. In the GR case, we will have

$$\frac{\Delta M_{\rm rem}}{\bar{M}_{\rm rem}} = 0, \qquad \frac{\Delta a_{\rm rem}}{\bar{a}_{\rm rem}} = 0 \qquad (17)$$

within the measurement error range. The analysis result for GW events in the LIGO-Virgo Catalog GWTC-1 is shown in Fig. 2 and Table III of Ref. [35]. Here, we should also note that the SNR for the ringdown phase is not so high in the current observations. Therefore, the merger–ringdown phase with a combination of phenomenological and analytical BH perturbation theory parameters [411] is treated in the parameterized test of GWs. This analysis result for GW events in the LIGO-Virgo Catalog GWTC-1 is also shown in Fig. 3 of Ref. [35]. On the other hand, when we estimate the mass and spin of the remnant BH (e.g., the right panel of Fig. 4 in Ref. [5]) without testing gravity, we use the inspiral–merger–ringdown waveform from numerical relativity [412–414].

Using only the ringdown phase, one of the best ways to test gravity is "black hole spectroscopy" by observing multiple QNMs [415] (see also Refs. [416,417] for testing the no-hair theorem with black hole ringdowns; another simple method is proposed by Ref. [418]). For example, we may consider Eq. (16) with the substitution

$$M_{\rm rem}^{\rm insp} = M_{\rm rem}^{(\ell=2,m=2)}, \qquad M_{\rm rem}^{\rm post-insp} = M_{\rm rem}^{(\ell=3,m=3)},$$
$$a_{\rm rem}^{\rm insp} = a_{\rm rem}^{(\ell=2,m=2)}, \qquad a_{\rm rem}^{\rm post-insp} = a_{\rm rem}^{(\ell=3,m=3)} \qquad (18)$$

if the $(\ell = 3, m = 3)$ QNM is the next dominant mode. In order to do so, it is necessary to extract $f_{\rm R}$ and τ of the weak ringdown signal from the noisy data accurately for each QNM. In Ref. [419], as the first step, mock data of GWs including some deviation from the GR prediction was prepared, and it was applied to the following five methods to extract the dominant QNM: (i) plain matched filtering with ringdown part, (ii) matched filtering with both merger and ringdown parts, (iii) Hilbert–Huang transformation, (iv) autoregressive modeling, and (v) neural network. It was found that determination of $f_{\rm R}$ is much easier than τ, although the accuracy depends on the analysis methods. Interestingly, it turned out that the standard matched filtering does not give the optimal inference in this problem.

As a unified framework to test possible modifications of gravity, one can use the parametrized post-Einstein (PPE) approach [420]. In this approach, we consider the modification of the functions that appear in the GW waveform in GR, Eq. (12), without specifying the model as

$$A(f) \rightarrow \left(1 + \sum_i \alpha_i v^{2a_i}\right) A_{\rm GR}(f), \qquad \psi(f) \rightarrow \psi_{\rm GR}(f) + \sum_i \beta_i v^{2b_i - 5/2}, \qquad (19)$$

where α_i and β_i specify the amplitude of the modification, while a_i and b_i specify the PN order of the modification. The point is that the leading-order correction tends to be given by a particular PN order. In many cases the leading-order effects appear in the phase evolution. Of course, tests targeting a particular modification can be more sensitive.

The LIGO/Virgo collaborations did not give the constraints on the PPE parameters directly. Instead, they examined the constraint on the modification to the model parameters contained in the waveform model IMRPHENOMPv2, following the method proposed in Ref. [421] and implemented in Ref. [422]. For the inspiral part, they tested the modification to the existing PN coefficients in the phase evolution up to 3.5 PN order in GR as well as the -1 PN and 0.5 PN coefficients which are not present in GR templates. Modification of the parameters that characterize the merger and ringdown phases was also tested.

For the modification of GW propagation, what they did was similar to PPE, but the constraints were derived for the amplitude of modification per propagation distance by stacking the data. In all the cases mentioned above, no significant deviation from GR prediction has been obtained.

5.1.3. Model-independent test of extra polarizations

The GW interferometers basically detect the tidal deformation of the physical distances among nearby test masses, which can be described by the geodesic deviation equation for slowly moving objects,

$$\ddot{x}^i \approx -R^i{}_{0j0}x^j. \tag{20}$$

Namely, what we can observe is the rank-2 tidal tensor $E_{ij} = R_{i0j0}$. The absolute distance cannot be measured by current GW interferometers, and they measure the difference of the distance changes in different directions. Hence, the trace part of E_{ij} is irrelevant. In generic dynamics of geometry, therefore, there are five components that can be decomposed into three-dimensional (one scalar, two transverse vector, two transverse traceless) tensor components.

It is not easy to think of gravity models in which scalar or vector components of the tidal waves are emitted without modifying the GW waveform significantly. For example, in the case of scalar-tensor theories, the effect of scalar wave emission, which also contributes to the excitation of the scalar component of the tidal tensor, appears most significantly in the orbital evolution of the binary due to the radiation reaction that it causes. If we consider such models that can excite larger magnitudes of tidal tensor in the scalar or vector mode without losing much energy, the coupling of the matter field to those modes tends to be too large to hide the influence on the tests of gravity in the Solar System.

For the reason mentioned above, sensible models would be conversion of the excitation energy from the tensor modes, i.e. standard GW modes, to the other exotic modes during the propagation. In that case, the waveform can be identical to the original GW waveform, although the phase velocity of the scalar and vector waves can be different from the speed of light. In that case, it is difficult to put a constraint on the conversion of the energy during the propagation. So far, only comparison of likeliness between pure tensor modes and pure scalar modes or between pure tensor modes and pure vector modes has been done, finding that pure tensor modes are largely preferred [35,423,424].

In a general framework, a GW signal can be a superposition of scalar and/or vector modes in addition to the ordinary tensor modes:

$$S_a(t, \hat{\Omega}) = \sum_a F_a^P(t, \hat{\Omega}) h^P(t). \tag{21}$$

Here, F_a^P is the antenna pattern function of the ath detector for the polarization P, and h_P is the GW waveform for the polarization P, where $P = +, \times, V, W, S$, and L [425–427]. The V and W modes are vector modes, and S and L modes are scalar modes that satisfy $F_a^S = -F_a^L$ [425]. The
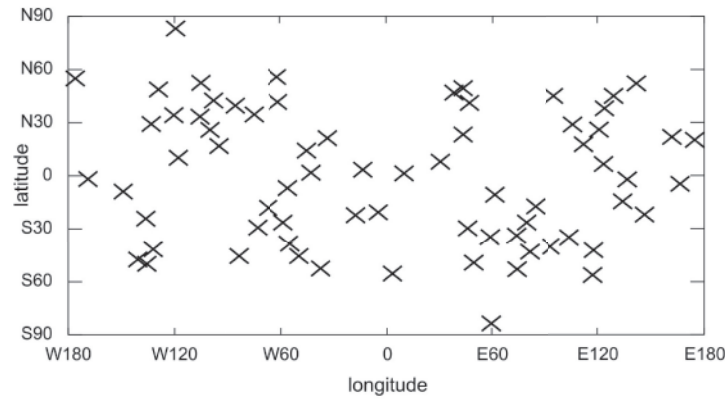
Fig. 35. Seventy sky positions in Earth-centered coordinates. At these points for a GW source, the spin-1 test can be done in principle, because the spin-0 and spin-2 modes can be perfectly eliminated. The numerical calculations were oerformed in Ref. [433].

antenna pattern functions are dependent on a GW source location θ and ϕ, which are the latitude and longitude, respectively. The separability of the polarization modes of GWs from a point source has been investigated by solving an inverse problem for the first time in Ref. [428]. It has been shown that in a non-tensorial polarization search, the necessary number of detectors is at least the same as the number of polarization modes to be searched, e.g. at least three detectors are necessary to search for a superposition of two tensor and one scalar modes. The mode separability in the case of compact binary coalescences is subtle because their GW waveforms are well modeled with multiple source parameters. It is shown in Ref. [429] that even with correlations and degeneracies among the parameters, a mixture of the polarization modes is separable with the same number of detectors as the number of modes. Then, the scalar or vector modes with similar amplitudes to the tensor modes can be detected. For BNSs observed with third-generation detectors such as the Einstein telescope [430] or Cosmic Explorer [431], mode separation with a smaller number of detectors is possible due to the long duration of a signal ($\gtrsim$ 1 hr) and the time-evolving detector antenna patterns [432].

With the help of an electromagnetic counterpart, more polarization modes than mentioned above can be searched once the sky location is fixed. We will discuss this possibility next.

Direct polarization test with the help of an electromagnetic counterpart   We consider the analysis of data from a GW source, $S_a(t, \hat{\Omega}) + n_a(t)$, where n_a is the detector noise. Equation (21) means that tests of all polarization modes with a network of interferometers require at least five detectors. However, Ref. [433] pointed out that there exist particular sky positions that allow for a vector mode test, because scalar modes, even if they exist, can be perfectly eliminated from a certain combination of strain outputs at the four detectors only for these sky directions (see Fig. 35). They also found that a vector mode test can be performed using four detectors [434]. They put a direct upper bound on a vector component from the GW170817 event, since the scalar modes can be largely suppressed for this event [434,435].

Very recently, they proposed a general formulation for directly testing extra GW polarization and a certain condition that allows for a scalar test. First, we focus on the network composed of the four ground-based interferometers. For a given source, we know its sky position, as is the case of GW events with an electromagnetic counterpart such as GW170817. Then, one knows exactly how to shift the arrival time of the GW from detector to detector.
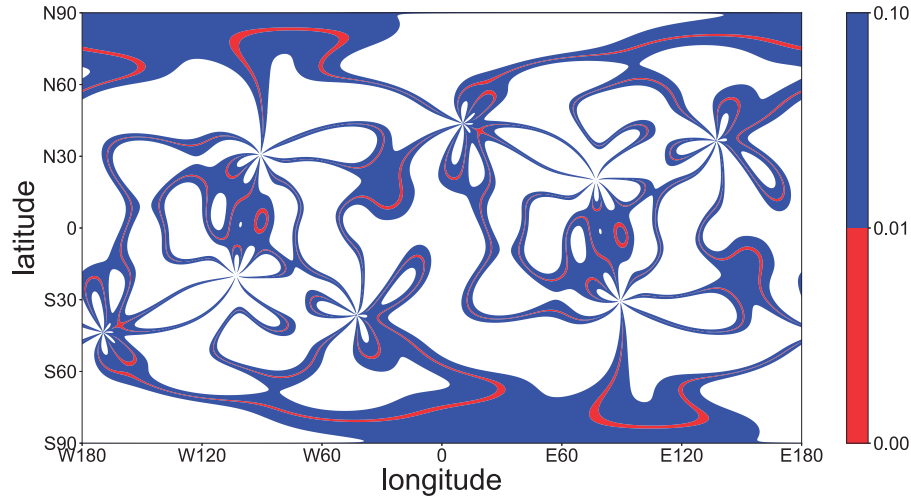
Fig. 36. Contour plot of D_4 in Earth-centered coordinates. The numerical calculations were performed in Ref. [435].

For example, the projection operator is defined to eliminate the W, $+$, and $\times$ modes. It is denoted as $\Pi^{aW+\times}$. For this example, h_W, h_+, and $h_\times$ in the strain outputs $\{S_a\}$ are eliminated as

$$\Pi^{aW+\times} S_a = \left(\varepsilon^{abcd} F_a^S F_b^W F_c^+ F_d^\times \right) (h_S - h_L) + \left(\varepsilon^{abcd} F_a^V F_b^W F_c^+ F_d^\times \right) h_V + \Pi^{aW+\times} n_a. \qquad (22)$$

If the coefficient of h_V in Eq. (22) vanishes in a certain sky region, there remains only the spin-0 part in the null stream. Therefore, the spin-0 polarization test is possible if a GW source is found in this sky region. The vanishing coefficient condition is

$$D_4 \equiv \begin{vmatrix} F_1^V & F_1^W & F_1^+ & F_1^\times \\ F_2^V & F_2^W & F_2^+ & F_2^\times \\ F_3^V & F_3^W & F_3^+ & F_3^\times \\ F_4^V & F_4^W & F_4^+ & F_4^\times \end{vmatrix} = 0. \qquad (23)$$

Note that this is invariant for choosing a reference axis for the polarization angle. $D_4 = 0$ (or a sufficiently small D_4, practically) is a condition for directly testing scalar modes separately from the other modes with only four detectors [435] (see Fig. 36).

A possible straightforward procedure for GW data analysis along this direction is as follows. First, we determine the sky location of the GW/EM source from multi-messenger astronomy, in particular by optical and VLBI observations. Second, by using the sky location, the arrival time shift for each GW detector is taken into account. Next, the (time-shifted) strain output at each detector is substituted into S_a on the left-hand side of Eq. (22). If the left-hand side of Eq. (22) is above the noise level (the last term on the right-hand side), then the existence of extra GW polarizations could be suggested. If it is comparable to (or lower than) the noise level, a certain *direct* upper bound can be placed on extra GW polarizations (through the first and second terms on the right-hand side). In this procedure, explicit templates of GW waveforms are not needed. In this sense, this test of extra GW polarizations is *robust*. Further study along this course is left for the future. For instance, sophisticated algorithms and pipelines would be important for real data analysis, because the nature of detector noise is quite complicated.

With four detectors, GR consistency tests can be performed by examining if the wave in the fourth detector, say KAGRA, is consistent with the three-detector network. Equation (21) for strain outputs

($a = 1, \ldots, 5$) from the five detectors, including LIGO-India, can always be solved for $h_S - h_L$, h_V, h_W, h_+, and $h_\times$. In principle, adding the fifth detector will thus allow for a direct search of extra GW polarizations for *any* sky region. This will be interesting in probing new gravitational physics beyond GR.

5.1.4. *Gravitational waveforms corresponding to various modifications of gravity*

The sources of GWs are composed of objects of extremely strong gravity in the sense that the deviation from the Minkowski spacetime is significant. The spacetime curvature radius is comparable to the size of the system in the case of BH and/or NS binaries.

In the case of BBHs, emission of an electromagnetic counterpart is not expected much. In fact, no detection of an electromagnetic counterpart has been reported so far. In the case of binaries that include an NS, we have a chance to detect the electromagnetic counterpart. In fact, various follow-up observations succeeded in finding the counterpart for GW170817, the first coalescing BNS event detected by GWs [9] (see Sect. 3). However, even in that case the emission of the electromagnetic counterpart in the region of truly strong gravity cannot be observed directly because of the large opacity of the high-density matter.

In contrast, GWs are emitted from the bulk motion of objects where the strong gravity is really at work. Hence, GWs are thought to be an indispensable probe of strong gravity. Here, we summarize various modifications of the GW waveform by considering representative extended theories of gravity.

Scalar-tensor gravity As the most typical modification of gravity, one can consider scalar-tensor theories. A representative theory is Brans–Dicke theory [436], defined by the action

$$S = \frac{1}{16\pi} \int d^4x \sqrt{-g} \left(\phi R - \omega_{\mathrm{BD}} \phi^{-1} \phi_{,\alpha} \phi^{,\alpha} \right) - \sum_a \int d\tau_a m_a(\phi), \qquad (24)$$

where ω_{BD} is the so-called Brans–Dicke parameter. When we send ω_{BD} to ∞, Einstein gravity is recovered. $m_a(\phi)$ is the effective mass of a star labeled by a, and it depends on the local value of the scalar field around the star. The effective gravitational coupling depends on ω_{BD} as $G_{\mathrm{eff}} = (4+2\omega_{\mathrm{BD}})/(\phi(3+2\omega_{\mathrm{BD}}))$, and the dimensionless scalar charge is defined by $s_a := \partial \ln m_a(\phi)/\partial \ln \phi$, which can be interpreted as the dependence of the gravitational binding energy of the star on G_{eff}.

The modification to the GW waveform appears at $-1\,\mathrm{PN}$ order like $\psi(f) = \cdots + (3/128)(\pi \mathcal{M} f)^{5/3} \left[\alpha v^{-2/3} + 1 + \cdots \right]$ in Eq. (13), where the coefficient α is given by $\alpha = -5(s_1 - s_2)^2/(64\omega_{\mathrm{BD}})$ [437]. This is caused by dipole radiation of the scalar field. If the scalar charge of two stars is proportional to their mass, i.e. if the dimensionless scalar charges are identical, dipole radiation does not occur. Hence, dipole radiation is not expected from equal-mass BNSs.

In this model, a numerical approach is also possible, but the effect is larger for lower frequencies. Therefore, the template based on the PN approach mentioned above would be sufficient, unless positive detection of the presence of a scalar charge is reported.

One scenario leading to a scalar charge to compact stars is spontaneous scalarization in the context of the generalized Brans–Dicke model, in which ω_{BD} is promoted to a function of ϕ [438]. A rather intuitive understanding of this process can be obtained by introducing the canonically normalized field $\varphi = \int \sqrt{2\omega_{\mathrm{BD}}(\phi)/\phi}\, d\phi$. In terms of this new field, the gravitational action would be rewritten

as

$$S = \frac{1}{16\pi} \int d^4x \sqrt{-g} \left(\phi(\varphi)R - \frac{1}{2}\varphi_{,\alpha}\varphi^{,\alpha} \right). \tag{25}$$

From this expression, one can find that the φ-dependent part of the energy of a static body would be given approximately by

$$\int d^3x \left(\varphi_{,i}\varphi^{,i} - 8\pi\phi(\varphi)\rho \right) \approx R^3 \left(\varphi/R^2 - 8\pi\rho\phi(\varphi) \right), \tag{26}$$

where, after the curvature is replaced with the energy density ρ using the Einstein equation as an approximation, the deviation from the Minkowski metric is neglected. In the last line, the size of the system is set to R and φ is assumed to vanish outside the compact object. If the function $\phi(\varphi)$ is convex upward at the origin and the density becomes high enough or the size of the compact object is large enough, a non-trivial configuration of the scalar field develops inside the star, which leads to giving a scalar charge to the star. The point is that this happens only in the situation where $\rho R^2 \approx M/R$ is sufficiently large.

Within the category of scalar-tensor theory, more generalization is possible. The Horndeski theory [439] is the most general scalar tensor theory having second-order equations of motion. This theory can, however, be generalized further in a healthy way to the so-called degenerate higher-order scalar tensor (DHOST) theories [440–442], which inevitably have higher-order equations of motion, but still propagate the same number of degrees of freedom as the Horndeski theory does (i.e. one scalar and two tensor modes). The Horndeski and DHOST theories offer us a powerful unifying framework to study the physics of dark energy and modified gravity (see, e.g., Ref. [443] for a review).

Measuring the speed of GWs can constrain the Horndeski and DHOST theories. The Lagrangian for the DHOST theories satisfying $c_{\mathrm{GW}} = 1$ is given by [37–40]

$$\mathcal{L} = G_2(\phi, X) - G_3(\phi, X)\Box\phi + f(\phi, X)R + A_3(\phi, X)\Box\phi\phi^\mu\phi_{\mu\nu}\phi^\nu$$
$$+ A_4\phi^\mu\phi_{\mu\rho}\phi^{\rho\nu}\phi_\nu + A_5(\phi^\mu\phi_{\mu\nu}\phi^\nu)^2, \tag{27}$$

where $X := -\phi^\mu\phi_\mu/2$ and

$$A_4 = -\frac{1}{2f}\left(2A_3 f - 3f_X^2 - 2A_3 f_X X + A_3^2 X^2 \right), \qquad A_5 = -\frac{A_3}{f}\left(f_X + A_3 X \right). \tag{28}$$

We thus have four free functions of ϕ and X. For $A_3 = 0$ and $f = f(\phi)$, this reduces to a subclass of the Horndeski theory. Solar System and astrophysical experiments/observations are potentially able to put further bounds on the functions in the above Lagrangian.

For Solar System and astrophysical tests of the Horndeski and DHOST theories, it is important to understand the Vainshtein screening mechanism [455], which suppresses the scalar-mediated force and is typically implemented in scalar tensor theories whose Lagrangian depends on the second derivatives of the scalar field. In the Horndeski subclass with $A_3 = 0$ and $f = f(\phi)$, the Vainshtein mechanism is known to work perfectly for a static spherically symmetric body, $\Phi = \Psi = -G_{\mathrm{N}}M/r$, inside a certain radius (which is sufficiently larger than the size of stars and the Solar System), where Φ and Ψ are two metric potentials defined by $\delta g_{00} = -2\Phi$ and $\delta g_{ij} = -2\Psi\delta_{ij}$, $G_{\mathrm{N}} := 1/16\pi f$ is the effective Newton constant, and M is the mass contained within r. Therefore, it would be difficult to place Solar System/astrophysical constraints on this subclass.

In generic DHOST theories, the behavior of weak gravitational fields is more interesting. It was found in Refs. [41–43] that

$$\Phi' = G_{\mathrm{N}}\left(\frac{M}{r^2} + \frac{\Upsilon_1}{4}M''\right), \qquad \Psi' = G_{\mathrm{N}}\left(\frac{M}{r^2} - \frac{5\Upsilon_2}{4}\frac{M'}{r} + \Upsilon_3 M''\right), \qquad (29)$$

where G_{N} and Υ_i are written in terms of f and A_3, and the prime denotes differentiation with respect to r. Since $M = \text{constant}$ outside the source body, Eq. (29) shows that gravity is modified only inside astrophysical bodies in generic DHOST theories. (In other words, Vainshtein screening operates nicely in the vacuum exterior region.) This partial breaking of Vainshtein screening was first discovered in Ref. [444]. A number of astrophysical tests of Vainshtein-breaking theories have been proposed so far. Going beyond the weak gravity regime, it was shown in Ref. [445] that the structure of relativistic stars is quite sensitive to the Vainshtein-breaking effect, which would potentially give tight constraints on DHOST theories in the strong gravity regime.

It was pointed out in Refs. [446,447] that gravitons can decay into ϕ in DHOST theories. To avoid this, it is required that $A_3 = 0$. Otherwise, GWs would not be observed. Upon imposing this constraint we have $A_4 = 3f_X^2/2f$ and $A_5 = 0$. This yields a special subclass of DHOST theories characterized by three free functions, in which the behavior of weak gravitational fields is completely different from Eq. (29), as shown in Refs. [448,449]. (In fact, Eq. (29) is derived assuming $A_3 \neq 0$.) The main result of Refs. [448,449] is summarized as follows: (i) a kind of fine-tuning is required even in the vacuum exterior region so that Solar System tests are evaded; (ii) in the interior region the metric potentials Φ and Ψ obey the standard inverse power law, but the two do not coincide; (iii) the interior and exterior values of the effective Newton constant are different,

$$G_{\mathrm{in}} = \frac{G_{\mathrm{ext}}}{1 - Xf_X/f}, \qquad G_{\mathrm{ext}} = \frac{1}{16\pi f\,(1 - Xf_X/f)}. \qquad (30)$$

All of these features are in sharp contrast with the case of generic DHOST theories.

A stringent bound on this particular class of DHOST theories with $A_3 = 0$ comes from the fact that the measured value of the Newton constant (which is supposed to be G_{ext}) is different from the gravitational coupling of GWs by a factor of $1 - Xf_X/f$. This can be seen from the quadratic Lagrangian for GWs,

$$\mathcal{L}_{\mathrm{GW}}^{(2)} = \frac{1}{16\pi\,G_{\mathrm{GW}}}\left(h^{\mu\nu}\Box h_{\mu\nu} + \cdots\right) + \frac{1}{2}h^{\mu\nu}T_{\mu\nu}, \qquad G_{\mathrm{GW}} = \frac{1}{16\pi f}. \qquad (31)$$

Assuming that the scalar radiation does not take part in the energy loss, one may naively replace the Newton constant in the standard quadrupole formula with G_{GW}. Then, from the orbital decay of the Hulse–Taylor pulsar we find that $|Xf_X/f| \lesssim 10^{-3}$. It would be interesting to explore other astrophysical constraints on this special class of Vainshtein-breaking modified gravity.

Quadratic gravity   As a low-energy effective theory of the dynamics of the metric, the term in the Lagrangian at the lowest order of the mass dimension is the cosmological constant, and the next to leading order is the Einstein–Hilbert action. In this sense, a possible natural extension of gravity is to consider adding terms quadratic in curvature to the Lagrangian.

There are three parity-preserving terms, R^2, $R_{\mu\nu}R^{\mu\nu}$, and $R_{\mu\nu\rho\sigma}R^{\mu\nu\rho\sigma}$. The R^2 term is classified as an alternative representation of scalar tensor theories [450]. One combination, $R_{\mathrm{GB}} = R^2 - 4R_{\mu\nu}R^{\mu\nu} + R_{\mu\nu\rho\sigma}R^{\mu\nu\rho\sigma}$, is know as the Gauss–Bonnet term, which does not contribute to the

equations of motion as it can be written as a total divergence. Hence, the truly remaining new possibility is, e.g., adding $R_{\mu\nu}R^{\mu\nu}$. However, this theory has a ghost degree of freedom, i.e. it contains infinitely many negative norm/energy states, which leads to an absence of stable vacua. This is caused by the presence of higher-derivative terms in $R_{\mu\nu}R^{\mu\nu}$. Hence, we need to treat such a model simply as a low-energy effective theory. Then, the higher-derivative terms can be replaced by using the lower-order equations of motion, which is now the Einstein equations, up to an appropriate field redefinition [451]. Once we apply this procedure to replace $R_{\mu\nu}R^{\mu\nu}$ with $T_{\mu\nu}T^{\mu\nu}$, the model is reduced to just Einstein gravity with matter fields described by a slightly complicated Lagrangian.

As a parity-violating term quadratic in the curvature, we can think of the Chern–Simons term, $R\tilde{R} := \epsilon^{\alpha\beta}{}_{\sigma\chi}R^{\sigma\chi}{}_{\mu\nu}R^{\mu\nu}{}_{\alpha\beta}/2$, where $\varepsilon^{\mu\nu\rho\sigma}$ is the Levi–Cività tensor. However, this term is also written as a total divergence, and hence it does not contribute to the equations of motion.

One interesting extension is to introduce a scalar field coupled to these higher-order curvature terms. The two cases with a scalar field coupling to the Gauss–Bonnet term and the Chern–Simons term have been extensively studied. The Lagrangian is given by

$$L = \frac{1}{16\pi G_{\mathrm{N}}}\left[R + \frac{\ell^2}{4}\phi(R_{\mathrm{GB}}\text{ or }R\tilde{R}) - \frac{1}{2}(\partial\phi)^2 - V(\phi)\right], \tag{32}$$

where ℓ is the length scale that characterizes the coupling of the axion field to the Chern–Simons term. The deviation from GR in such theories can be easily hidden in the weak gravity regime. An interesting phenomenon in this setup is that BHs can have scalar hairs. The constraint coming from the GW observations is discussed in Sect. 5.1.5.

Massive gravity If we simply add a mass to the graviton, the equations for the GW propagation in flat spacetime $\Box h_{\mu\nu} = 0$ would be expected to be modified to $(\Box - m^2)h_{\mu\nu} = 0$. However, this simple-minded extension is not theoretically very attractive. One consistent way that preserves the Lorentz symmetry on the Minkowski background is dRGT ghost-free massive gravity [452]. However, it turned out to be difficult to construct even the homogeneous isotropic universe model in this framework, and hence various generalizations were proposed. In any case, the dRGT ghost-free massive gravity model requires an auxiliary metric or tetrad that does not transform as dynamical fields. As a result, the general covariance is not maintained.

In this class of models of massive gravity, linear perturbation predicts a large excitation of a scalar graviton around a star, even if we send the graviton mass to a small value, which is known as the van Dam–Veltman–Zakharov discontinuity [453,454]. However, in this limit, linear analysis cannot be trusted any further and the non-linear effects become large, strongly suppressing the excitation of the scalar graviton. This is the very same mechanism as the Vainshtein mechanism introduced above [455]. As a result, gravity around massive objects is thought to behave very similarly to GR.

Bigravity A natural way to recover the general covariance in the theory with a massive graviton is to promote the auxiliary metric field in the dRGT ghost-free massive gravity to a dynamical one. Such a model is know as dRGT bi-gravity theory, which was also shown to be ghost free in Ref. [456]. However, the general covariance guarantees the presence of a massless graviton. In this model the field that becomes massive is the second graviton, which corresponds to the difference of two metrics, roughly speaking.

The generation and propagation of GWs from binaries was studied in Ref. [457], in which the possibility of graviton oscillation between two graviton modes, one massless and the other massive,

was pointed out. In the ordinary situation, only the metric directly coupled to the matter field is curved, while the other remains almost flat. In a particular choice of the model parameters, however, the massive graviton becomes very heavy around a star, and hence the difference between the two metrics is suppressed. In this case, graviton oscillation becomes possible without violating the test of gravity, say, in the Solar System.

Einstein-aether theory   The Einstein-aether theory, which for hypersurface-orthogonal configurations of the aether vector can be considered as the low-energy limit of a candidate theory of quantum gravity called non-projectable Hořava–Lifshitz gravity, also serves as a testing ground of GR. We thus review the theoretical and observational constraints on the Einstein-aether theory.

The basic variables of the gravity sector are [458] the four-dimensional metric $g_{\mu\nu}$, the aether vector u^{μ}, and a Lagrange multiplier λ, where $\mu, \nu = 0, \ldots, 3$ and we adopt the signatures $(-, +, +, +)$ for the metric. The total action is $S = S_{\text{æ}} + S_m$ [459], where

$$S_{\text{æ}} = \frac{1}{16\pi G_{\text{æ}}} \int \sqrt{-g}\, d^4x \left[R(g_{\mu\nu}) + \mathcal{L}_{\text{æ}}\left(g_{\mu\nu}, u^{\lambda}\right) \right], \quad S_m = \int \sqrt{-g}\, d^4x \left[\mathcal{L}_m\left(g_{\mu\nu}, \psi\right) \right]. \quad (33)$$

Here, ψ denotes matter fields, R and g are the Ricci scalar and the determinant of $g_{\mu\nu}$, and

$$\mathcal{L}_{\text{æ}} \equiv -M^{\alpha\beta}{}_{\mu\nu}\left(D_{\alpha}u^{\mu}\right)\left(D_{\beta}u^{\nu}\right) + \lambda\left(g_{\alpha\beta}u^{\alpha}u^{\beta} + 1\right), \quad (34)$$

where D_{μ} denotes the covariant derivative compatible with $g_{\mu\nu}$, and

$$M^{\alpha\beta}{}_{\mu\nu} = c_1 g^{\alpha\beta}g_{\mu\nu} + c_2\delta^{\alpha}_{\mu}\delta^{\beta}_{\nu} + c_3\delta^{\alpha}_{\nu}\delta^{\beta}_{\mu} - c_4 u^{\alpha}u^{\beta}g_{\mu\nu}. \quad (35)$$

It is convenient to introduce linear combinations of the c_i $(i = 1, \ldots, 4)$ as $c_{ij} \equiv c_i + c_j$ and $c_{ijk} = c_i + c_j + c_k$. The Newton constant G_N is related to $G_{\text{æ}}$ as $G_N = G_{\text{æ}}/(1 - \frac{1}{2}c_{14})$ [460].

The Minkowski spacetime with $u_{\mu} = \delta^0_{\mu}$ is a solution of the Einstein-aether theory. It is then straightforward to analyze linear perturbations around the Minkowski background and investigate properties of the spin-0, -1, and -2 modes. The coefficients of the time kinetic term of each excitation must be positive,

$$q_{S,V,T} > 0; \qquad q_S = \frac{(1 - c_{13})(2 + c_{13} + 3c_2)}{c_{123}}, \quad q_V = c_{14}, \quad q_T = 1 - c_{13}. \quad (36)$$

In addition to the ghost-free condition, we must also require the absence of gradient instabilities by demanding that the squared speeds of propagation be non-negative. Moreover, the almost simultaneous detection of GW170817 [9] and GRB 170817A [36] sets a stringent constraint on the speed of the spin-2 mode as $-3 \times 10^{-15} < c_T - 1 < 7 \times 10^{-16}$, where $c_T^2 = 1/(1 - c_{13})$. This implies

$$|c_{13}| < 10^{-15}. \quad (37)$$

As for the spin-0 and -1 modes, the squared speeds must be greater than $1 - \mathcal{O}(1) \times 10^{-15}$ in order to avoid vacuum gravi-Čerenkov radiation [461]. We thus impose

$$c_{S,V}^2 \gtrsim 1; \qquad c_S^2 = \frac{c_{123}(2 - c_{14})}{c_{14}(1 - c_{13})(2 + c_{13} + 3c_2)}, \quad c_V^2 = \frac{2c_1 - c_{13}(2c_1 - c_{13})}{2c_{14}(1 - c_{13})} \quad (38)$$

in addition to Eq. (37).

Applying the theory to cosmology, one can find that the gravitational constant appearing in the effective Friedman equation is given by [460]

$$G_{\rm cos} = \frac{G_{\ae}}{1 + \frac{1}{2}(c_{13} + 3c_2)} = \frac{1 - \frac{1}{2}c_{14}}{1 + \frac{1}{2}(c_{13} + 3c_2)}G_{\rm N}. \tag{39}$$

One then needs to impose the nucleosynthesis bound as

$$\left| \frac{G_{\rm cos}}{G_{\rm N}} - 1 \right| \lesssim \frac{1}{8}. \tag{40}$$

Among the 10 parameterized post-Newtonian (PPN) parameters [462], the only two parameters that deviate from GR in this context are

$$\alpha_1 = -\frac{8(c_3^2 + c_1 c_4)}{2c_1 - c_1^2 + c_3^2}, \qquad \alpha_2 = \frac{1}{2}\alpha_1 - \frac{(c_1 + 2c_3 - c_4)(2c_1 + 3c_2 + c_3 + c_4)}{c_{123}(2 - c_{14})}. \tag{41}$$

In the weak-field regime, Solar System observations set the constraints [462]

$$|\alpha_1| \leq 10^{-4}, \qquad |\alpha_2| \leq 10^{-7}. \tag{42}$$

In the strong-field regime, the isolated millisecond pulsars PSR B1937+21 [463] and PSR J17441134 [464] set the constraint [465,466] as

$$\left| \hat{\alpha}_1 \right| \leq 10^{-5}, \qquad \left| \hat{\alpha}_2 \right| \leq 10^{-9} \quad (95\% \text{ confidence}), \tag{43}$$

where $(\hat{\alpha}_1, \hat{\alpha}_2)$ denotes the strong-field generalization of (α_1, α_2) [467] given by [468]

$$\hat{\alpha}_1 = \alpha_1 + \frac{c_-(8 + \alpha_1)\sigma_{\ae}}{2c_1}, \qquad \hat{\alpha}_2 = \alpha_2 + \frac{\hat{\alpha}_1 - \alpha_1}{2} - \frac{(c_{14} - 2)(\alpha_1 - 2\alpha_2)\sigma_{\ae}}{2(c_{14} - 2c_{13})}. \tag{44}$$

Here, $\sigma_{\ae}$ is the sensitivity. Unfortunately, the sensitivities $\sigma_{\ae}$ of a neutron star, which depend on the c_i and the EOS of nuclear matter [468], are not known for the new ranges of the parameters. We thus leave the analysis of these two constraints for future work.

Putting all theoretical and observational constraints together, we have Eq. (37), as well as

$$0 < c_{14} \leq 2.5 \times 10^{-5}, \qquad c_{14} \lesssim c_1 \tag{45}$$

in the (c_1, c_{14})-plane and

$$0 < c_{14} \lesssim c_2 \lesssim 0.095, \qquad -10^{-7} \leq \frac{c_{14}(c_{14} + 2c_2 c_{14} - c_2)}{c_2(2 - c_{14})} \leq 10^{-7} \tag{46}$$

in the (c_2, c_{14})-plane. In Fig. 37, we show the constraints in Eq. (46). All the constraints except Eq. (37) are divided into two classes, those in the (c_1, c_{14})-plane and those in the (c_2, c_{14})-plane. For further discussions about the constraints, such as a comparison with those on the hypersurface-orthogonal theory [469], see Ref. [470].

5.1.5. *Dedicated tests for particular models*
To optimally constrain particular models, it would be better to employ a dedicated test. One can imagine various extensions of the simple GW waveform adopted in the PPE framework.
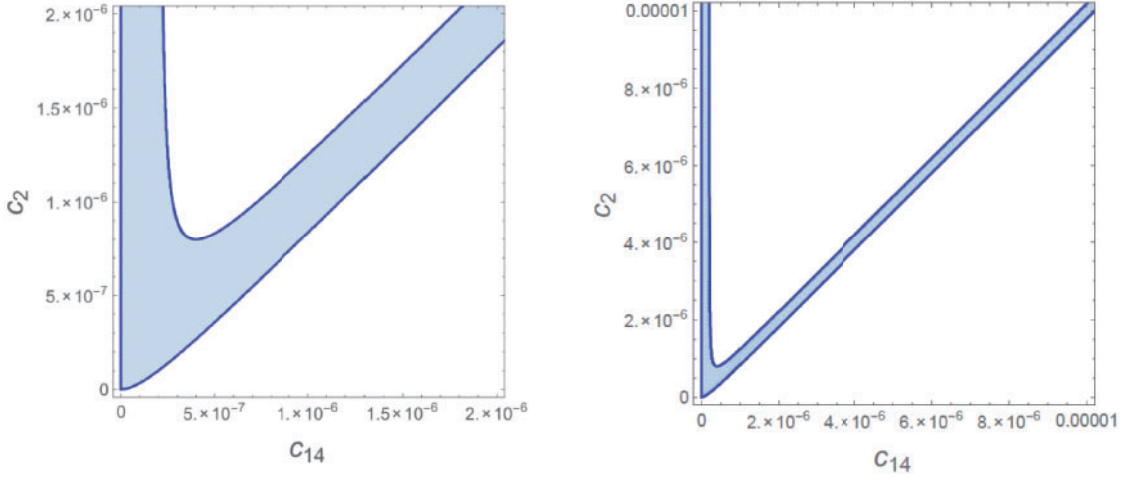
Fig. 37. The constraints in the (c_2, c_{14})-plane summarized in Eq. (46) with two different scales. Adopted from Ref. [470].

Massive dipolar radiation   One simple example is to add a mass to the field that extracts energy from the system through dipole radiation. Since the radiation is emitted only in the frequency range above the mass scale, the modifications in the orbital evolution, and hence in the GW phase evolution, show up only at high frequencies [471,472]. Therefore, even if an NS has a scalar hair, such scalar-tensor theories can evade the constraint from pulsar observations due to the mass of the scalar field. A simple model of scalar-tensor theories with a massive scalar field has been constrained by several observations: (i) $m \lesssim 10^{-27}$ eV for stability on cosmological scales [473], (ii) $m \lesssim 10^{-16}$ eV from the observations of a pulsar–white dwarf binary [474], and (iii) 10^{-13} eV $\lesssim m \lesssim 10^{-11}$ eV [475,476], which relies on measurements of the high spins of stellar-mass BHs [477].

As mentioned earlier, Einstein–dilaton–Gauss–Bonnet (EdGB) theory is an interesting candidate modification of gravity obtained by adding a quadratic term in curvature. We need to introduce a scalar field, which we call the dilaton here, to make the Gauss–Bonnet term relevant. In this model a BH can possess a scalar charge and hence dipole radiation is expected. The constraint from observed GW data on the model in which the scalar field is massive was examined in Ref. [478]. In the massless limit, on the other hand, the current constraint on EdGB theory is $\sqrt{\alpha_{\mathrm{EdGB}}} \lesssim 1.9$ km, which is obtained by using low-mass X-ray binaries [479].

Activation of dipole radiation due to massive fields and modifications to the GW waveform have been analyzed for the GW events in the GWTC-1 catalog [480] to constrain the magnitude of the modification [478]. Since the ground-based detectors, LIGO, Virgo, and KAGRA, are sensitive at frequencies around 10–1000 Hz, GW signals for those are useful to test the dipole radiation of the massive field in the range 10^{-14} eV $\lesssim m \lesssim 10^{-13}$ eV. For $m \lesssim 10^{-14}$ eV the modification of GWs effectively reduces to the massless limit.

Taking into account the dominant correction to the energy flux due to the dipole radiation, which appears at -1 PN order, the GW waveform in the frequency domain, $\tilde{h}(f)$, can be expressed as [481,482]

$$\tilde{h}(f) = \tilde{h}_{\mathrm{GR}}(1 + \delta\mathcal{A})\, e^{i\delta\Psi}. \tag{47}$$

The corrections to the amplitude and the phase are, respectively, expressed as [478]

$$\delta \mathcal{A} = -\frac{1}{2} A \frac{(\hat{\omega}^2 - 1)^{3/2}}{\hat{\omega}^3} u^{-2} \, \Theta(\hat{\omega}^2 - 1), \tag{48}$$

$$\delta \Psi = \frac{5}{48} A \left(\frac{1}{m \, \mathcal{M}} \right)^{7/3} F(\hat{\omega}) \, \Theta(\hat{\omega}^2 - 1), \tag{49}$$

with

$$F(\hat{\omega}) \equiv - \int_{\hat{\omega}}^{\infty} d\hat{\omega}' \, \frac{\hat{\omega} - \hat{\omega}'}{\hat{\omega}'^{22/3}} \left[\hat{\omega}'^2 - 1 \right]^{3/2}, \tag{50}$$

where $\hat{\omega} = \pi f / m$, m is the mass of the field, Θ is the Heaviside step function, and A is a parameter denoting the amplitude of the dipole radiation relative to the quadrupole one. The modified waveform, Eq. (47) with Eqs. (48) and (49), can model the modification due to the vector field as well as the scalar one. In this parametrization, there are two free parameters: the mass of the field m and the relative amplitude of dipole radiation A. Note that A is a function of the system parameters, such as the masses and spins, and the parameters of the modified gravity theory under consideration.

Using the above waveform as a template, 90% C.L. constraints on A for each LIGO/Virgo collaboration GW event has been derived [478]. Since the modified waveform is valid only for the inspiral phase, the calculations were terminated when the mass scale reached an appropriately chosen threshold frequency for each event. We should recall that in general a strong constraint on A does not always imply a strong constraint on the modification to theory. This is because A is proportional to the squared difference of the scalar charges of the constituents of the binary, as we will see in Eq. (51). Therefore, GW events where this difference vanishes are not sensitive to the modification, even for quite a large coupling constant.

The constraints on A can be translated to a constraint on the coupling strength, using the relation [483–485]

$$A = \frac{5\pi}{6} \frac{\alpha_{\mathrm{EdGB}}^2}{M^4} \frac{\left(m_1^2 s_2^{\mathrm{EdGB}} - m_2^2 s_1^{\mathrm{EdGB}} \right)^2}{M^4 \eta^{18/5}}, \tag{51}$$

where

$$s_i^{\mathrm{EdGB}} = \frac{2\sqrt{1 - \chi_i^2}}{1 + \sqrt{1 - \chi_i^2}}, \qquad i = 1, 2, \tag{52}$$

describes the spin dependence of the BH's scalar charges. After combining five BBH events possessing relatively high SNR (GW150914, GW170814, GW170608, GW170104, and GW151226), $\sqrt{\alpha_{\mathrm{EdGB}}}$ is constrained as $\sqrt{\alpha_{\mathrm{EdGB}}} \lesssim 2.47$ km for all masses below 6×10^{-14} eV for the first time with 90% C.L., including $\sqrt{\alpha_{\mathrm{EdGB}}} \lesssim 1.85$ km in the massless limit. This constraint in the massless limit is much stronger than the results in Refs. [486,487], while it is accidentally almost the same as with low-mass X-ray binaries [479].

Since the number of events with a lighter chirp mass, such as BNSs, must increase in the near future, it will be interesting to stack those events by assuming various theories in which charged NSs are allowed consistently. Furthermore, NS–BH binaries will also be interesting [488], because, in addition to their light chirp mass, A can be large in a theory such that only either the NS or the BH has a charge, as in the case of EdGB theory. Moreover, future multiband observations will improve the current upper bounds of various modified theories [489].

Propagation of GWs in parity-violating gravity   The nearly simultaneous detection of GWs and gamma-ray burst from the merger of neutron stars, GW170817/GRB170817A [9,36], offered an unprecedented opportunity to measure the speed of GWs, $c_{\rm GW}$, to the level of one part in 10^{15}. This puts a tight constraint on modified gravity as an alternative to dark energy. We now discuss the impact of this constraint on the parity-violating sector of gravity [490].

Let us consider parity-violating gravity whose action is of the form

$$S = \frac{1}{16\pi G} \int d^4x \sqrt{-g} \left[R + \mathcal{L}_{\rm PV} + \mathcal{L}_\phi \right],$$
(53)

where $\mathcal{L}_{\rm PV}$ is the parity-violating Lagrangian and $\mathcal{L}_\phi$ is the Lagrangian for a scalar field ϕ which may be coupled non-minimally to gravity. The most frequently studied example is Chern–Simons (CS) gravity, for which $\mathcal{L}_{\rm PV}$ is given by

$$\mathcal{L}_{\rm PV} = \mathcal{L}_{\rm CS} := f(\phi) R\tilde{R}.$$
(54)

It was recently found that one can construct other parity-violating Lagrangians for the gravity sector such as [491]

$$\mathcal{L}_{\rm PV} = \sum_{I=1}^{4} a_I(\phi, \phi_\mu \phi^\mu) L_A,$$
(55)

with $L_1 := \varepsilon^{\mu\nu\alpha\beta} R_{\alpha\beta\rho\sigma} R_{\mu\nu}{}^\rho{}_\lambda \phi^\sigma \phi^\lambda$, $L_2 := \varepsilon^{\mu\nu\alpha\beta} R_{\alpha\beta\rho\sigma} R_{\mu\lambda}{}^{\rho\sigma} \phi_\nu \phi^\lambda$, $L_3 := \varepsilon^{\mu\nu\alpha\beta} R_{\alpha\beta\rho\sigma} R^\sigma{}_\nu \phi^\rho \phi_\mu$, $L_4 := \phi_\lambda \phi^\lambda P$, and $\phi_\mu := \nabla_\mu \phi$. If $4a_1 + 2a_2 + a_3 + 8a_4 = 0$ is satisfied, the dangerous Ostrogradsky ghosts are removed in the unitary gauge.[2]

We consider GWs $h_{ij}(t, \vec{x})$ propagating on a cosmological background. The above examples yield a quadratic Lagrangian of the form

$$\mathcal{L}_{\rm PV}^{(2)} = \frac{1}{4} \left[\frac{\alpha(t)}{a\Lambda} \epsilon^{ijk} \partial_t h_{il} \partial_j \partial_t h_{kl} + \frac{\beta(t)}{a^3 \Lambda} \epsilon^{ijk} \partial^2 h_{il} \partial_j h_{kl} \right],$$
(56)

where ϵ^{ijk} is the antisymmetric symbol, Λ is some energy scale, and α and β are dimensionless functions of time determined essentially by the cosmological evolution of the scalar field. In the most familiar case of CS gravity, we identically have $\alpha = \beta$. However, we may have $\alpha \neq \beta$ in general. The Lagrangian in Eq. (56) can thus be used to describe GW propagation in parity-violating gravity in a unifying way [490] (see also Ref. [493] for an effective-field-theory approach to arrive at the same Lagrangian).

In the presence of the parity-violating interactions in Eq. (56), the $+$ and $\times$ polarization modes are coupled in the equations of motion, but one can obtain two decoupled equations by employing the circular polarization basis. In general parity-violating gravity, the equations of motion for GWs in Fourier space can be written as

$$\left(h_{\vec{k}}^A \right)'' + (2 + \nu_A)\mathcal{H}\left(h_{\vec{k}}^A \right)' + (c_{\rm GW}^A)^2 k^2 h_{\vec{k}}^A = 0,$$
(57)

---

[2] The ghost degrees of freedom might not be problematic if the theory is treated as a low-energy truncation of a fundamental theory. Although these ghost modes do cause instabilities if the theory is regarded as a complete theory, it is argued in Ref. [492] that the would-be ghost mode that is not manifest in the unitary gauge may be an instantaneous mode which does not in fact propagate and hence is not dangerous.

where the prime denotes differentiation with respect to the conformal time, $\mathcal{H} := a'/a$, and

$$\nu_A = \frac{\lambda_A(\alpha - \alpha'\mathcal{H}^{-1})}{1 - \lambda_A\alpha k/a\Lambda}\frac{k}{a\Lambda}, \qquad (c_{\mathrm{GW}}^A)^2 = \frac{1 - \lambda_A\beta k/a\Lambda}{1 - \lambda_A\alpha k/a\Lambda}. \tag{58}$$

Here, A labels left and right circular polarization modes, and $\lambda_A = \pm 1$. It can be seen that CS gravity corresponds to the special case with $(c_{\mathrm{GW}}^A)^2 = 1$. Therefore, from the propagation speed of gravity no constraint can be imposed on CS gravity. However, parity violation in the gravity sector in general leads to $(c_{\mathrm{GW}}^A)^2 \neq 1$ and thus is tightly constrained by GW170817. For $k/a \sim 100\,\mathrm{Hz}$, one has

$$\Lambda^{-1}|\alpha - \beta| \lesssim 10^{-11}\,\mathrm{km}. \tag{59}$$

This is the new limit on parity violation in the gravity sector derived in Ref. [490].

By parametrizing the modification of GW waveforms during propagation in this theory, the data in the O1/O2 catalog has been reanalyzed by a grid search with the matched filtering method [494]. The results imply that the above constraint improves by seven digits, since the matched filtering is sensitive to the phase modifications, while the constraints on the amplitude modification are similar to the previous result [495].

For a face-on binary, the effects of parity violation of gravity cannot be constrained because only one of the circular polarization modes can be observed. Therefore, obtaining a more stringent constraint or finding the signature of parity-violating gravity requires the detection of GW signals from a nearly edge-on binary.

Echoes from merger remnant black holes   Exotic compact objects are proposed as alternative models to BHs. They are assumed to be compact enough to possess the light ring, but without the event horizon. In such models, the features of GWs after the ringdown phase of compact binary coalescences are considered to be different from the BH case. The infalling waves generated during the merger–ringdown phase might be reflected at the surface of the object, which would just be absorbed if the horizon exists. The reflected waves will be partly reflected back again at the angular momentum barrier but partly transmitted. This process occurs repeatedly, which phenomenon is dubbed GW "echoes" [496,497] (see also Ref. [498] for a simple explanation with the causal structure of the Green's function of the wave equation with two potentials having disjoint bounded support). Therefore, the detection of echoes implies the existence of exotic compact objects. The simplest model of the compact objects is that the horizon is replaced by a reflecting membrane at around the Planck proper length from the horizon radius in Kerr spacetime. Reference [499] analyzed three O1 BBH events and reported echo signals at $3\,\sigma$ significance level (*p*-value 0.011). In their study, they assumed the GW waveform in the frequency domain as

$$\tilde{h}(f) = \tilde{h}_0(f)\sum_{n=1}^{N}\gamma^{n-1}e^{-i[2\pi f \Delta t_{\mathrm{echo}} + \phi(f)](n-1)}, \tag{60}$$

where γ is the overall reflection rate, Δt_{echo} is the interval between neighboring echoes, N is the number of echoes, and $\phi(f)$ is the phase shift. The function $\tilde{h}_0(f)$ is a merger–ringdown waveform extracted by cutting off the inspiral part smoothly from the inspiral–merger–ringdown waveform. The parameters γ and Δt_{echo} are the most relevant parameters to characterize the echo waveforms on which the significance of the signal depends most. Since Ref. [499] used only 32 s for the background estimation, Ref. [500] improved the background estimation using 4096 s and showed

lower significance, *p*-value 0.032, with the same template used in Ref. [499]. Bayesian analysis was also performed with the same template and small Bayes factors reported [501,502]. The spacetime considered in Ref. [499] is exactly Kerr spacetime outside the surface, while the assumption of a reflection rate in their study is not physically reasonable. Reference [503] derived the reflection rate at the angular momentum potential barrier numerically, and calculated a fitting formula for the reflection rate $R(f)$. The reflection rate becomes frequency dependent, unlike in the assumption of Ref. [499], and behaves as a high-pass filter, i.e. $R(f) \to 0$ ($R(f) \to 1$) for larger (smaller) f. As a result, the lower-frequency part of the waveform is strongly suppressed in the template given by Ref. [503] compared to that given by Ref. [499]. The modified template becomes

$$\tilde{h}(f) = \sqrt{1 - R^2(f)}\, \tilde{h}_0(f) \sum_{n=1}^{N} R(f)^{n-1} e^{-i[2\pi f \Delta t_{\text{echo}} + \phi(f)](n-1)}. \tag{61}$$

In this setup, Ref. [504] showed that the significance of echo signals becomes much lower, *p*-value larger than 0.9 for eight BBH events in O1 and O2, although neither a reduction nor an increase of the significance was observed by increasing the number of samples when the original waveform proposed in Ref. [499] was employed.

So far, we have focused on a model-dependent search. A morphology-independent search was performed in Refs. [505,506], which assumed that echo waveforms for any model can be effectively described as superpositions of sine-Gaussian waveforms. In their study, no significant echo signal was found in O1 and O2 events, including the BNS merger event. The reflection rate at the surface can also vary due to the model of the object. In the analytical template proposed by Refs. [507,508], the reflection rate at the object's surface was also assumed as a parameter. The reflection rate at the potential barrier was given from BH perturbations. Further details of testing exotic compact objects that include the echo phenomenon are reviewed in Ref. [509].

5.2. *Dark matter*

Arguably one of the most important questions in science is to elucidate the nature of dark matter. Identifying the nature of dark matter would have a huge impact on cosmology, particle physics, and astronomy. Many dark matter candidates have been proposed in the literature. Since different dark matter candidates yield different types of observational signals, various experiments targeted at particular dark matter have been conducted. In this subsection we give a brief overview of how GW experiments can shed light on some dark matter candidates.

5.2.1. *Axion*

An axion is a strong candidate for dark matter [510]. To probe axion dark matter, it is important to study electromagnetic waves [511] and GWs propagating in axion dark matter [512,513]. In particular, the gravitational Chern–Simons term allows us to probe the parity violation in the gravity sector. We consider the model specified by the Lagrangian in Eq. (32) with $V = m^2 \phi^2 / 2$.

It is instructive to write down the quadratic action deduced from Eq. (56) using the circular polarization modes as

$$S^{(2)} = \frac{M_p^2}{4} \int d^3k\, dt \, \left(1 - \frac{k\lambda_A}{M_p} \ell^2 \dot{\phi}\right) \left[\dot{h}_{\mathbf{k}}^A \dot{h}_{-\mathbf{k}}^A - k^2 h_{\mathbf{k}}^A h_{-\mathbf{k}}^A\right]. \tag{62}$$

To avoid a ghost, due to the signature flip of the factor $\left(1 - k\lambda_A \ell^2 \dot{\phi}/M_p\right)$, we need the cutoff scale below which we can use this effective action,

$$k < k_{\mathrm{g}} = 6.7 \times 10^9 \,\mathrm{Hz} \left(\frac{10^8 \,\mathrm{km}}{\ell}\right)^2 \sqrt{\frac{0.3 \,\mathrm{GeV} \,\mathrm{cm}^{-3}}{\rho}}. \tag{63}$$

The axion is coherently oscillating as $\phi = \phi_0 \cos(mt)$, with the amplitude determined by

$$\phi_0 \simeq 2.1 \times 10^7 \,\mathrm{eV} \left(\frac{10^{-10} \,\mathrm{eV}}{m}\right) \sqrt{\frac{\rho}{0.3 \,\mathrm{GeV} \,\mathrm{cm}^{-3}}}. \tag{64}$$

Here, we used the observed local dark matter density ρ. The coherent oscillation induces a parametric resonance of GWs with a frequency corresponding to the axion mass. Using the current upper bound $\ell \leq 10^8 \,\mathrm{km}$ [514], we can estimate the length scale $R_{\times 10}$ at which the GW grows 10 times larger as

$$R_{\times 10} = 5.2 \times 10^{-8} \,\mathrm{pc} \left(\frac{10^{-10} \,\mathrm{eV}}{m}\right)^2 \left(\frac{10^8 \,\mathrm{km}}{\ell}\right)^2 \sqrt{\frac{0.3 \,\mathrm{GeV} \,\mathrm{cm}^{-3}}{\rho}}. \tag{65}$$

Since the Jeans length r_{J} of the axion dark matter (the coherence length of the axion oscillation),

$$r_{\mathrm{J}} = 4.3 \times 10^{-3} \,\mathrm{pc} \left(\frac{m}{10^{-10} \,\mathrm{eV}}\right)^{-\frac{1}{2}} \left(\frac{\rho}{0.3 \,\mathrm{GeV} \,\mathrm{cm}^{-3}}\right)^{-\frac{1}{4}}, \tag{66}$$

is much larger than the growth length, a huge enhancement of the GW amplitude occurs, which gives rise to a strong constraint on the Chern–Simons coupling constant or the abundance of axion dark matter. We refer the reader to the original paper, Ref. [512], for the details. The detection strategy to probe this effect is under investigation.

5.2.2. *Primordial black holes*

Primordial black holes (PBHs) are a dark matter candidate that is not an elementary particle. The idea of PBHs dates back to 1971 when Hawking proposed the possibility that BHs are produced directly by the gravitational collapse of an overdense region in the primordial universe much earlier than the recombination era. PBHs heavier than about 10^{15} g do not lose their mass significantly due to Hawking radiation over the age of the universe. Since such PBHs are non-relativistic objects, interact with baryonic matter only gravitationally, and do not emit light, they have been considered as a dark matter candidate. Since the original proposal of PBHs, various observational searches for PBHs have been continuously conducted for a wide PBH mass range. So far, there is no observational evidence of PBHs, and upper limits on PBH abundance have been placed which, for some mass ranges, exclude the possibility that PBHs comprise all dark matter under the assumption that all PBHs have the same mass. Yet, there is still an open window where PBHs can provide all dark matter (see Ref. [515] for the most recent summary).

The LIGO/Virgo detection of binary BHs provoked explosive research activities on PBHs (see Ref. [8] for a review in this respect). An exciting possibility is that these BHs (or some of them) are PBHs. Indeed, features of the LIGO BHs such as comparatively large masses and small spins do not contradict PBHs. It is known that a dominant formation channel of PBH binaries is by the tidal force of the surrounding PBHs in the radiation-dominated era [516]. This channel can explain the merger rate of BH binaries derived by the LIGO/Virgo observations if the PBHs constitute a fraction of about 10^{-3} of the dark matter. Alternatively, a conservative assumption that LIGO BHs were produced by

the standard astrophysical processes yields an upper limit on the abundance of stellar-mass PBHs. Irrespective of whether LIGO BHs are PBHs or not, that PBHs can comprise at most $\sim 10^{-3}$ of dark matter is the most severe constraint for PBHs in the stellar mass range. This vividly demonstrates the power of GW observations to test PBHs as dark matter. It is worth mentioning that LIGO/Virgo Collaborations has extended searches for PBH mergers to the sub-solar-mass range [517].

Although stellar-mass PBHs are unlikely to explain all the dark matter, a question still remains as to whether such PBHs constitute a tiny fraction of dark matter. Answering that question would definitely have profound consequences for cosmology. To this end, it is essential to discriminate between PBHs and astrophysical BHs from GW observations. In what follows, we give a short review of several ideas in this direction proposed in the literature.

Mergers at high redshifts Contrary to astrophysical BH binaries, which formed long after the Big Bang, PBH binaries have existed since the universe was still dominated by radiation. Due to the broad distribution of orbital radius and eccentricity of PBH binaries, the merger rate of PBH binaries continuously extends to high redshift even beyond $z \sim 100$. On the other hand, the merger rate of astrophysical BHs drops sharply beyond $z \sim 10$. Thus, searches for mergers beyond $z \sim 10$ provide a clean test of the existence of PBHs. Reference [518] has shown that the proposed space interferometer called B-DECIGO is able to achieve this goal.

Mass distribution Mass distribution is another observable that can be used to test PBHs. Let m_1 and m_2 be the masses of the individual BHs in a binary, and $\mathcal{R}(m_1, m_2, t)$ the distribution of the merger rate of BH binaries at cosmic time t. Notice that $\mathcal{R}$ includes all the mergers, and the observational bias, which depends on the detectors, should be taken into account in translating $\mathcal{R}$ to a directly measurable merger distribution. Since this bias can be handled, we regard $\mathcal{R}$ as an observable quantity here.

Reference [519] showed that PBH binaries formed in the radiation-dominated era give a characteristic mass dependence to $\mathcal{R}$ as

$$\mathcal{R} = C\psi(m_1)\psi(m_2)(m_1 + m_2)^{\alpha}. \tag{67}$$

Here, C is a constant independent of m_1, m_2, $\psi(m)$ is a function which depends on the PBH mass function, and $\alpha \approx 1$. Quite interestingly, $\mathcal{R}$ depends almost linearly on the total mass $m_1 + m_2$ irrespective of the PBH mass function, which differs for each inflation model and is unknown.[3] It is worth mentioning that other physical mechanisms leading to BH mergers predict different α values. For instance, PBH binaries formed by two-body encounters in the low-redshift universe yield $\alpha \approx 1.43$ [521]. Astrophysical BH binaries formed in dense star clusters give $\alpha \sim 4$ [522]. BH binaries formed in mass-segregated environments such as galactic nuclei give α that varies with the total binary mass m_t [523]. Thus measurement of α provides a unique test of the PBH scenario which is independent of the assumption for the PBH mass function.

An alternative approach is to directly compare the observed mass distribution with the theoretical ones in the PBH hypothesis computed for several representative PBH mass functions. This program has already been applied to the observational data, and some PBH functions have been excluded [524].

---

[3] A recent study generalized the original work and found that α takes a value different from unity if dark matter perturbation provides the dominant torque to produce the angular momentum of the PBH binaries [520].

Spin of PBHs Another potentially powerful GW observable to test the PBH scenario is spin distribution. GW observations are primarily sensitive to the quantity defined by Eq. (2). PBHs form binaries dynamically and there is no correlation between the spins of individual PBHs and the orbital angular momentum. Thus, the probability density of $\chi_{\rm eff}$ is an even function, which is a robust prediction of the PBH scenario. The concrete shape of the probability density of $\chi_{\rm eff}$ is determined by the spin distribution of the individual PBHs, $W(J)$. Formally, the spin distribution of PBHs at cosmic time t is given by

$$W(J,t) = \int dJ' \, Q(J,J',t) \int_{\delta_{\rm th}(J')} P(\delta_M, J') d\delta_M, \tag{68}$$

where $P(\delta_M, J)$ is the probability distribution of the density contrast δ_M and the angular momentum J of an overdense region that collapses to a PBH if $\delta_M \geq \delta_{\rm th}$. $Q(J,J',t)$ represents the evolution of the PBH spin from its initial value J' to J at time t. $P(\delta_M, J)$ is determined once the statistical properties of the primordial density perturbations are specified. All these quantities must be determined in order to derive $W(J,t)$. In Refs. [525–527], analyses related to $P(\delta_M, J)$ and $Q(J,J',t)$ were performed. For the Gaussian primordial density perturbation, the angular momentum of PBHs coming from $P(\delta_M, J)$ is estimated to be at most a few percent [526,527]. In Ref. [528], $\delta_{\rm th}(J)$ for PBHs formed in the radiation-dominated epoch was obtained as

$$\delta_{\rm th} \approx 0.62 + 0.015 a_{\rm K}^2, \tag{69}$$

where $a_{\rm K}$ is the Kerr parameter. This result shows that the threshold increases as the angular momentum is increased, and the formation of highly spinning PBHs is suppressed compared to slowly spinning PBHs. On the other hand, PBHs formed in the matter-dominated phase, which could happen prior to the radiation-dominated epoch, are likely to have significant spin [529].

Different GW frequency bands So far, we have considered GWs from PBHs in the LIGO frequency band. This band corresponds to the merger phase of stellar-mass PBH binaries. However, GWs in different frequency bands could also be generated. PBH binaries in the inspiral phase, due to their enormous number and weak signals, constitute a low-frequency stochastic GW background. Furthermore, primordial density perturbations as a seed of PBHs provide another stochastic GW background by the non-linear mode couplings. These low-frequency GWs are not probed by the LIGO-like detectors, but could be detected by future detectors such as LISA.

In what follows we introduce possible constraints on the abundance of PBHs expected in future experiments by evaluating energy-density spectra of stochastic GW backgrounds in two independent ways. We show that the experiments are sensitive to constraining the fraction to cold dark matter (CDM) for $10^{-5} \lesssim f_{\rm PBH} \lesssim 1$ ($10^{-13} \lesssim f_{\rm PBH} \lesssim 1$) in the case of GWs from coalescing events (curvature perturbations) [530].

By using the merger rate of PBH binaries [531], we can calculate the energy-density spectrum of the stochastic gravitational wave background (SGWG), which is discussed in Ref. [532] to be

$$\Omega_{\rm GW}(\nu) = \frac{\nu}{\rho_{\rm c}} \int_0^{\frac{\nu_{\rm cut}}{\nu} - 1} \frac{R_{\rm PBH}(z)}{(1+z)H(z)} \frac{dE_{\rm GW}}{d\nu_{\rm s}}(\nu_{\rm s}) dz, \tag{70}$$

where $\frac{dE_{\rm GW}}{d\nu_{\rm s}}(\nu_{\rm s})$ is the energy spectrum of GWs produced by a BBH coalescence [533,534], $\nu_{\rm s} = (1+z)\nu$, and $\nu_{\rm cut}$ is the cutoff frequency.
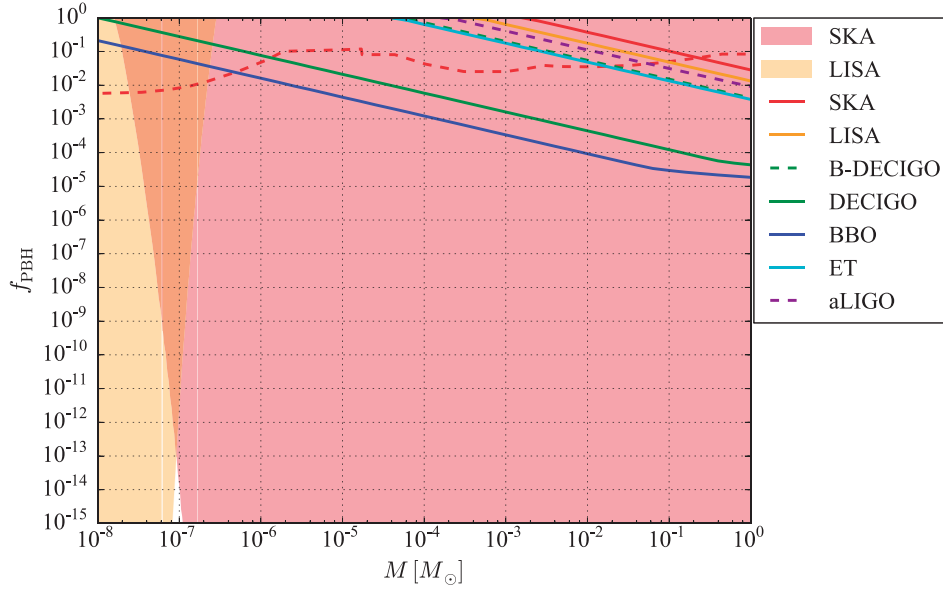
Fig. 38. Expected constraints on PBH abundance versus PBH mass from the null detection of the two kinds of SGWB. The existing observational constraint (red dashed) is plotted for comparison [535]. This figure is taken from Fig. 7 of Ref. [530].

On the other hand, according to Appendix D of Ref. [530], we obtain the dimensionless energy-density spectrum of the induced SGWB to be

$$
\Omega_{\mathrm{IGW}}\left(\nu = \frac{k}{2\pi}\right) = \Omega_{\mathrm{r},0}\left(\frac{g_*(T(k))}{g_*\left(T_{\mathrm{eq}}\right)}\right)\left(\frac{g_{*,s}(T(k))}{g_{*,s}\left(T_{\mathrm{eq}}\right)}\right)^{-4/3}
$$

$$
\times \frac{3A^2}{64}\left(\frac{4 - \tilde{k}^2}{4}\right)^2 \tilde{k}^2\left(3\tilde{k}^2 - 2\right)^2
$$

$$
\times \left[\pi^2\left(3\tilde{k}^2 - 2\right)^2 \Theta(2 - \sqrt{3}\tilde{k}) + \left(4 + \left(3\tilde{k}^2 - 2\right)\ln\left|1 - \frac{4}{3\tilde{k}^2}\right|\right)^2\right]
$$

$$
\times \Theta(2 - \tilde{k}), \tag{71}
$$

where $\nu = k/2\pi$ denotes the GW frequency, and the dimensionless wavenumber $\tilde{k} = k/k_0$ is introduced for simplicity. We used the notations of physical quantities from Ref. [530].

Assuming a null detection of GW signals from coalescing events in Eq. (70) or curvature perturbations in Eq. (71), we can constrain the abundance of PBHs, which is plotted in Fig. 38. The solid lines give the expected upper limits on the abundance by the non-detection of GW signals from coalescing events, and the shaded regions mean the parameter space excluded by the non-detection of GW signals from curvature perturbations.

6. Conclusion

Gravitational wave physics and astronomy have finally become science that can be compared with actual observational data after a long period of preparation. In this paper we have introduced important findings such as the discovery of massive binary black holes and binary neutron stars, which bring us new implications about the physical properties of nuclear matter, heavy element synthesis in the

universe, and the origin of short gamma-ray bursts. It is expected that this trend will be further accelerated as the international network of gravitational wave detectors on the ground expands and space gravitational wave antennas proliferate. Further improvements in sensitivity are planned for ground-based gravitational wave interferometers, including the construction of the third-generation detectors [430,431]. An increase in sensitivity by an order of magnitude increases the chances of detecting an event with a very high signal-to-noise ratio, and at the same time increases the event rate by a factor of 1000 or more, which enables highly statistically accurate analyses of gravitational waves. It is certain that future gravitational wave observations will revolutionize our understanding of the physical universe, powered by improvements in the accuracy of gravitational wave source position and multi-messenger follow-up observations for gravitational wave events. It is clear that we have not yet seen the full potential of this new probe of physics.

As the observation technology advances, it becomes more important to analyze and interpret the accumulated data correctly. The real benefit from gravitational wave observations can be extracted only when we can construct an appropriate physical picture to explain the observed signals, by combining data from other observational means to follow up gravitational wave detections. To that end, we need to further promote multi-messenger astronomy, and advance the theoretical research to understand gravitational wave sources. In addition, in order to detect gravitational wave signals that have not been discovered yet to open up a new paradigm, it is necessary to further develop gravitational wave data analysis methods, making full use of the accumulated theoretical knowledge.

References

[1] B. P. Abbott et al. [LIGO Scientific and Virgo Collaborations], Phys. Rev. Lett. **116**, 061102 (2016).
[2] W. M. Farr, N. Sravan, A. Cantrell, L. Kreidberg, C. D. Bailyn, I. Mandel, and V. Kalogera, Astrophys. J. **741**, 103 (2011).
[3] S. Rosswog, U. Feindt, O. Korobkin, M.-R. Wu, J. Sollerman, A. Goobar, and G. Martinez-Pinedo, Class. Quantum Grav. **34**, 104001 (2017).
[4] K. Hotokezaka, P. Beniamini, and T. Piran, Int. J. Mod. Phys. D **27**, 1842005 (2018).
[5] B. P. Abbott et al. [LIGO Scientific and Virgo Collaborations], Phys. Rev. X **9**, 031040 (2019).
[6] B. P. Abbott et al., Astrophys. J. Lett. **818**, L22 (2016).
[7] C. L. Rodriguez, M. Morscher, B. Pattabiraman, S. Chatterjee, C.-J. Haster, and F. A. Rasio, Phys. Rev. Lett. **115**, 051101 (2015); **116**, 029901 (2016) [erratum].
[8] M. Sasaki, T. Suyama, T. Tanaka, and S. Yokoyama, Class. Quantum Grav. **35**, 063001 (2018).
[9] B. P. Abbott et al. [LIGO Scientific and Virgo Collaborations], Phys. Rev. Lett. **119**, 161101 (2017).
[10] B. P. Abbott et al., Astrophys. J. Lett. **848**, L12 (2017).
[11] K. Mooley, A. T. Deller, O. Gottlieb, E. Nakar, G. Hallinan, S. Bourke, D. A. Frail, A. Horesh, A. Corsi, and K. Hotokezaka, Nature **561**, 355 (2018).
[12] G. Ghirlanda et al., Science **363**, 968 (2019).
[13] K. Ioka and T. Nakamura, Prog. Theor. Exp. Phys. **2018**, 043E02 (2018).
[14] K. Ioka and T. Nakamura, Mon. Not. R. Astron. Soc. **487**, 4884 (2019).
[15] H. Abdalla et al., Astrophys. J. Lett. **850**, L22 (2017).
[16] A. Albert et al., Astrophys. J. Lett. **850**, L35 (2017).
[17] M. Ajello et al., Astrophys. J. **861**, 85 (2018).
[18] K. Abe et al., Astrophys. J. Lett. **857**, L4 (2018).
[19] K. Murase, M. W. Toomey, K. Fang, F. Oikonomou, S. S. Kimura, K. Hotokezaka, K. Kashiyama, K. Ioka, and P. Mészáros, Astrophys. J. **854**, 60 (2018).

[20] S. S. Kimura, K. Murase, I. Bartos, K. Ioka, I. S. Heng, and P. Mészáros, Phys. Rev. D **98**, 043020 (2018).

[21] D. Biehl, J. Heinze, and W. Winter, Mon. Not. R. Astron. Soc. **476**, 1191 (2018).

[22] K. Kyutoku and K. Ioka, Astrophys. J. **827**, 83 (2016).

[23] S. A. Colgate and R. H. White, Astrophys. J. **143**, 626 (1966).

[24] H. A. Bethe, Rev. Mod. Phys. **62**, 801 (1990).

[25] H.-T. Janka, T. Melson, and A. Summa, Ann. Rev. Nucl. Part. Sci. **66**, 341 (2016).

[26] A. Burrows, Rev. Mod. Phys. **85**, 245 (2013).

[27] K. Kotake, K. Sumiyoshi, S. Yamada, T. Takiwaki, T. Kuroda, Y. Suwa, and H. Nagakura, Prog. Theor. Exp. Phys. **2012**, 01A301 (2012).

[28] B. Müller, Pub. Astron. Soc. Aus. **33**, e048 (2016).

[29] B. W. Grefenstette et al., Astrophys. J. **802**, 15 (2015).

[30] M. Tanaka, K. Maeda, P. A. Mazzali, K. S. Kawabata, and K. Nomoto, Astrophys. J. **837**, 105 (2017).

[31] K. Nakamura, S. Horiuchi, M. Tanaka, K. Hayama, T. Takiwaki, and K. Kotake, Mon. Not. R. Astron. Soc. **461**, 3296 (2016).

[32] A. Mirizzi, I. Tamborra, H.-Th. Janka, N. Saviano, K. Scholberg, R. Bollig, L. Hüdepohl, and S. Chakraborty, Nuovo Cim. **39**, 1, (2016).

[33] S. Horiuchi and J. P. Kneller, J. Phys. G: Nucl. Part. Phys. **45**, 043002 (2018).

[34] N. Gehrels, M. Leventhal, and C. J. MacCallum, Astrophys. J. **322**, 215 (1987).

[35] B. P. Abbott et al. [LIGO Scientific and Virgo Collaborations, Fermi Gamma-ray Burst Monitor, INTEGRAL], Phys. Rev. D **100**, 104036 (2019) [arXiv:1903.04467 [gr-qc]] [Search INSPIRE].

[36] B. P. Abbott et al. [LIGO Scientific, Virgo, Fermi-GBM, and INTEGRAL Collaborations], Astrophys. J. Lett. **848**, L13 (2017).

[37] P. Creminelli and F. Vernizzi, Phys. Rev. Lett. **119**, 251302 (2017).

[38] J. Sakstein and B. Jain, Phys. Rev. Lett. **119**, 251303 (2017).

[39] J. M. Ezquiaga and M. Zumalácarregui, Phys. Rev. Lett. **119**, 251304 (2017).

[40] T. Baker, E. Bellini, P. G. Ferreira, M. Lagos, J. Noller, and I. Sawicki, Phys. Rev. Lett. **119**, 251301 (2017).

[41] D. Langlois, R. Saito, D. Yamauchi, and K. Noui, Phys. Rev. D **97**, 061501(R) (2018).

[42] M. Crisostomi and K. Koyama, Phys. Rev. D **97**, 021301(R) (2018).

[43] A. Dima and F. Vernizzi, Phys. Rev. D **97**, 101302(R) (2018).

[44] B. F. Schutz, Nature **323**, 310 (1986).

[45] B. P. Abbott et al. [LIGO Scientific, Virgo, 1M2H, Dark Energy Camera GW-E, DES, DLT40, Las Cumbres Observatory, VINROUGE, MASTER Collaborations], Nature **551**, 85 (2017).

[46] K. Hotokezaka, E. Nakar, O. Gottlieb, S. Nissanke, K. Masuda, G. Hallinan, K. P. Mooley, and A. T. Deller, Nature Astron. **3**, 940 (2019).

[47] T. Venumadhav, B. Zackay, J. Roulet, L. Dai, and M. Zaldarriaga, Phys. Rev. D **101**, 083030 (2020) [arXiv:1904.07214 [astro-ph.HE]] [Search INSPIRE].

[48] K. Sugimura, T. Matsumoto, T. Hosokawa, S. Hirano, and K. Omukai, Astrophys. J. Lett. **892**, 14 (2020).

[49] C. F. McKee and J. C. Tan, Astrophys. J. **681**, 771 (2008).

[50] T. Hosokawa, K. Omukai, N. Yoshida, and H. W. Yorke, Science **334**, 1250 (2011).

[51] T. Hosokawa, S. Hirano, R. Kuiper, H. W. Yorke, K. Omukai, and N. Yoshida, Astrophys. J. **824**, 119 (2016).

[52] G. Duchêne and A. Kraus, Ann. Rev. Astron. Astrophys. **51**, 269 (2013).

[53] H. Sana, S. E. de Mink, A. de Koter, N. Langer, C. J. Evans, M. Gieles, E. Gosset, R. G. Izzard, J.-B. Le Bouquin, and F. R. N. Schneider, Science **337**, 444 (2012).

[54] T. Matsumoto and T. Hanawa, Astrophys. J. **595**, 913 (2003).

[55] S. M. Miyama, C. Hayashi, and S. Narita, Astrophys. J. **279**, 621 (1984).

[56] T. Tsuribe and S.-i. Inutsuka, Astrophys. J. Lett. **523**, L155 (1999).

[57] M. N. Machida, K. Tomisaka, T. Matsumoto, and S.-i. Inutsuka, Astrophys. J. **677**, 327 (2008).

[58] J. J. Tobin, T. L. Bourke, S. Mader, L. Kristensen, H. Arce, F. Gueth, A. Gusdorf, C. Codella, S. Leurini, and X. Chen, Astrophys. J. **870**, 81 (2019).

[59] H. Susa, Astrophys. J. **877**, 99 (2019).

[60] P. C. Clark, S. C. O. Glover, R. J. Smith, T. H. Greif, R. S. Klessen, and V. Bromm, Science **331**, 1040 (2011).

[61] T. H. Greif, V. Springel, S. D. M. White, S. C. O. Glover, P. C. Clark, R. J. Smith, R. S. Klessen, and V. Bromm, Astrophys. J. **737**, 75 (2011).

[62] T. H. Greif, V. Bromm, P. C. Clark, S. C. O. Glover, R. J. Smith, R. S. Klessen, N. Yoshida, and V. Springel, Mon. Not. R. Astron. Soc. **424**, 399 (2012).

[63] T. Hartwig, V. Bromm, R. S. Klessen, and S. C. O. Glover, Mon. Not. R. Astron. Soc. **447**, 3892 (2015).

[64] S. Hirano and V. Bromm, Mon. Not. R. Astron. Soc. **470**, 898 (2017).

[65] M. N. Machida and T. Nakamura, Mon. Not. R. Astron. Soc. **448**, 1405 (2015).

[66] R. J. Smith, S. C. O. Glover, P. C. Clark, T. Greif, and R. S. Klessen, Mon. Not. R. Astron. Soc. **414**, 3633 (2011).

[67] A. Stacy, T. H. Greif, and V. Bromm, Mon. Not. R. Astron. Soc. **422**, 290 (2012).

[68] A. Stacy, V. Bromm, and A. T. Lee, Mon. Not. R. Astron. Soc. **462**, 1307 (2016).

[69] H. Susa, Astrophys. J. **773**, 185 (2013).

[70] E. I. Vorobyov, A. L. DeSouza, and S. Basu, Astrophys. J. **768**, 131 (2013).

[71] M. N. Machida and K. Doi, Mon. Not. R. Astron. Soc. **435**, 3283 (2013).

[72] A. Askar, M. Szkudlarek, D. Gondek-Rosńska, M. Giersz, and T. Bulik, Mon. Not. R. Astron. Soc. **464**, L36 (2017).

[73] C. L. Rodriguez, S. Chatterjee, and F. A. Rasio, Phys. Rev. D **93**, 084029 (2016).

[74] C. L. Rodriguez, M. Zevin, C. Pankow, V. Kalogera, and F. A. Rasio, Astrophys. J. Lett. **832**, L2 (2016).

[75] C. L. Rodriguez, M. Zevin, P. Amaro-Seoane, S. Chatterjee, K. Kremer, F. A. Rasio, and C. S. Ye, Phys. Rev. D **100**, 043027 (2019).

[76] C. L. Rodriguez, P. Amaro-Seoane, S. Chatterjee, and F. A. Rasio, Phys. Rev. Lett. **120**, 151101 (2018).

[77] J. Samsing, A. Askar, and M. Giersz, Astrophys. J. **855**, 124 (2018).

[78] M. Giersz, D. C. Haggie, J. R. Hurley, and A. Hypki, Mon. Not. R. Astron. Soc. **431**, 2184 (2013).

[79] C. L. Rodriguez, M. Morscher, L. Wang, S. Chatterjee, F. A. Rasio, and R. Spurzem, Mon. Not. R. Astron. Soc. **463**, 2109 (2016).

[80] L. Wang, R. Spurzem, S. Aarseth, M. Giersz, A. Askar, P. Berczik, T. Naab, R. Schadow, and M. B. N. Kouwenhoven, Mon. Not. R. Astron. Soc. **458**, 1450 (2016).

[81] M. Iwasawa, S. P. Zwart, and J. Makino, Comp. Astrophys. Cosmol. **2**, 6 (2015).

[82] S. Oshino, Y. Funato, and J. Makino, Pub. Astron. Soc. Japan **63**, 881 (2011).

[83] L. Wang, K. Nitadori, and J. Makino, Mon. Not. R. Astron. Soc. **493**, 3398 (2020).

[84] L. Wang, R. Spurzem, S. Aarseth, K. Nitadori, P. Berczik, M. B. N. Kouwenhoven, and T. Naab, Mon. Not. R. Astron. Soc. **450**, 4070 (2015).

[85] H. C. Plummer, Mon. Not. R. Astron. Soc. **71**, 460 (1911).

[86] P. C. Peters and J. Mathews, Phys. Rev. **131**, 435 (1963).

[87] J. Kumamoto, M. S. Fujii, and A. Tanikawa, Mon. Not. R. Astron. Soc. **486**, 3942 (2019).

[88] M. Chruslinska and G. Nelemans, Mon. Not. R. Astron. Soc. **488**, 5300 (2019).

[89] P. Madau and T. Fragos, Astrophys. J. **840**, 39 (2017).

[90] J. Kumamoto, M. S. Fujii, and A. Tanikawa, Mon. Not. R. Astron. Soc. **495**, 4268 (2020) [arXiv:2001.10690 [astro-ph.HE]] [Search INSPIRE].

[91] B. P. Abbott et al., Astrophys. J. Lett. **882**, L24 (2019).

[92] T. Prusti et al. [Gaia Collaboration], Astron. Astrophys. **595**, A1 (2016).

[93] M. Shikauchi, J. Kumamoto, A. Tanikawa, and M. S. Fujii, Publ. Astron. Soc. Jap. **72**, 45 (2020) [arXiv:2001.11199 [astro-ph.HE]] [Search INSPIRE].

[94] M. S. Yamaguchi, N. Kawanaka, T. Bulik, and T. Piran, Astrophys. J. **86**, 21 (2018).

[95] K. Belczynski, D. E. Holz, T. Bulik, and R. O'Shaughnessy, Nature **534**, 512 (2016).

[96] T. Kinugawa, K. Inayoshi, K. Hotokezaka, D. Nakauchi, and T. Nakamura, Mon. Not. R. Astron. Soc. **456**, 1093 (2014).

[97] S. J. Aarseth, Gravitational N-Body Simulations (Cambridge University Press, Cambridge, 2003).

[98] J. R. Hurley, C. A. Tout, and O. R. Pols, Mon. Not. R. Astron. Soc. **329**, 897 (2002).

[99] Y. B. Bae, Ch. Kim, and H. M. Lee, Mon. Not. R. Astron. Soc. **440**, 2714 (2014).

[100] S. Banerjee, H. Baumgardt, and P. Kroupa, Mon. Not. R. Astron. Soc. **402**, 371 (2010).

[101] M. S. Fujii, A. Tanikawa, and J. Makino, Pub. Astron. Soc. Japan **69**, 94 (2017).

[102] J. Hong, E. Vesperini, A. Askar, M. Giersz, M. Szkudlarek, and T. Bulik, Mon. Not. R. Astron. Soc. **480**, 5645 (2018).
[103] D. Park, C. Kim, H. M. Lee, Y.-B. Bae, and K. Belczynski, Mon. Not. R. Astron. Soc. **469**, 4665 (2017).
[104] A. Tanikawa, Mon. Not. R. Astron. Soc. **435**, 1358 (2013).
[105] A. Tanikawa, T. Yoshida, T. Kinugawa, K. Takahashi, and H. Umeda, Mon. Not. R. Astron. Soc. **495**, 4170 (2020) [arXiv:1906.06641 [astro-ph.HE]] [Search INSPIRE].
[106] K. Takahashi, T. Yoshida, H. Umeda, K. Sumiyoshi, and S. Yamada, Mon. Not. R. Astron. Soc. **456**, 1320 (2016).
[107] K. Takahashi, T. Yoshida, and H. Umeda, Astrophys. J. **857**, 111 (2018).
[108] K. Takahashi, K. Sumiyoshi, S. Yamada, H. Umeda, and T. Yoshida, Astrophys. J. **871**, 153 (2019).
[109] T. Yoshida, T. Takiwaki, K. Kotake, K. Takahashi, K. Nakamura, and H. Umeda, Astrophys. J. **881**, 16 (2019).
[110] S. Bernuzzi, A. Nagar, T. Dietrich, and T. Damour, Phys. Rev. Lett. **114**, 161103 (2015).
[111] D. Bini and T. Damour, Phys. Rev. D **90**, 124037 (2014).
[112] D. Bini, T. Damour, and G. Faye, Phys. Rev. D **85**, 124034 (2012).
[113] T. Damour and A. Nagar, Phys. Rev. D **81**, 084016 (2010).
[114] T. Damour, A. Nagar, and L. Villain, Phys. Rev. D **85**, 123007 (2012).
[115] M. Favata, Phys. Rev. Lett. **112**, 101101 (2014).
[116] É. É. Flanagan and T. Hinderer, Phys. Rev. D **77**, 021502(R) (2008).
[117] T. Hinderer, B. D. Lackey, R. N. Lang, and J. S. Read, Phys. Rev. D **81**, 123016 (2010).
[118] B. D. Lackey and L. Wade, Phys. Rev. D **91**, 043002 (2015).
[119] D. Lai, F. A. Rasio, and S. L. Shapiro, Astrophys. J. **420**, 811 (1994).
[120] T. Mora and C. M. Will, Phys. Rev. D **69**, 104021 (2004); **71**, 129901 (2005) [erratum].
[121] J. S. Read, L. Baiotti, J. D. E. Creighton, J. L. Friedman, B. Giacomazzo, K. Kyutoku, C. Markakis, L. Rezzolla, M. Shibata, and K. Taniguchi, Phys. Rev. D **88**, 044042 (2013).
[122] J. S. Read, C. Markakis, M. Shibata, K. Uryū, J. D. E. Creighton, and J. L. Friedman, Phys. Rev. D **79**, 124033 (2009).
[123] J. Vines, É. É. Flanagan, and T. Hinderer, Phys. Rev. D **83**, 084051 (2011).
[124] L. Wade, J. D. E. Creighton, E. Ochsner, B. D. Lackey, B. F. Farr, T. B. Littenberg, and V. Raymond, Phys. Rev. D **89**, 103012 (2014).
[125] K. Yagi and N. Yunes, Phys. Rev. D **89**, 021303(R) (2014).
[126] J. M. Lattimer, Ann. Rev. Nucl. Part. Sci. **62**, 485 (2012).
[127] T. Dietrich and T. Hinderer, Phys. Rev. D **95**, 124006 (2017).
[128] T. Hinderer et al., Phys. Rev. Lett. **116**, 181101 (2016).
[129] F. Messina, R. Dudi, A. Nagar, and S. Bernuzzi, Phys. Rev. D **99**, 124051 (2019).
[130] A. Nagar et al., Phys. Rev. D **98**, 104052 (2018).
[131] J. Steinho, T. Hinderer, A. Buonanno, and A. Taracchini Phys. Rev. D **94**, 104028 (2016).
[132] L. Baiotti, T. Damour, B. Giacomazzo, A. Nagar, and L. Rezzolla, Phys. Rev. D **84**, 024017 (2011).
[133] S. Bernuzzi, A. Nagar, M. Thierfelder, and B. Brügmann, Phys. Rev. D **86**, 044030 (2012).
[134] T. Dietrich, S. Bernuzzi, and W. Tichy, Phys. Rev. D **96**, 121501(R) (2017).
[135] T. Dietrich, A. Samajdar, S. Khan, N. K. Johnson-McDaniel, R. Dudi, and W. Tichy, Phys. Rev. D **100**, 044003 (2019).
[136] R. Haas et al., Phys. Rev. D **93**, 124062 (2016).
[137] K. Hotokezaka, K. Kyutoku, H. Okawa, and M. Shibata, Phys. Rev. D **91**, 064060 (2015).
[138] K. Hotokezaka, K. Kyutoku, Y.-i. Sekiguchi, and M. Shibata, Phys. Rev. D **93**, 064082 (2016).
[139] K. Kiuchi, K. Kawaguchi, K. Kyutoku, Y. Sekiguchi, M. Shibata, and K. Taniguchi, Phys. Rev. D **96**, 084060 (2017).
[140] D. Radice, L. Rezzolla, and F. Galeazzi, Mon. Not. R. Astron. Soc. Lett. **437**, L46 (2014).
[141] M. Thierfelder, S. Bernuzzi, and B. Brügmann, Phys. Rev. D **84**, 044012 (2011).
[142] K. Kawaguchi, K. Kiuchi, K. Kyutoku, Y. Sekiguchi, M. Shibata, and K. Taniguchi, Phys. Rev. D **97**, 044044 (2018).
[143] K. Kiuchi, K. Kawaguchi, K. Kyutoku, Y. Sekiguchi, and M. Shibata, Phys. Rev. D **101**, 084006 (2020).
[144] S. Khan, S. Husa, M. Hannam, F. Ohme, M. Pürrer, X. Jiménez Fortez, and A. Bohé, Phys. Rev. D **93**, 044007 (2016).

[145] A. Taracchini et al., Phys. Rev. D **89**, 061502(R) (2014).
[146] D. Shoemaker, Advanced LIGO anticipated sensitivity curves (available at: https://dcc.ligo.org/ LIGO-T0900288/public, date last accessed April 17, 2021).
[147] T. Narikawa, N. Uchikata, K. Kawaguchi, K. Kiuchi, K. Kyotoku, M. Shibata, and H. Tagoshi, Phys. Rev. Res. **2**, 043039 (2020).
[148] J. M. Lattimer and M. Prakash, Phys. Rep. **621**, 127 (2016).
[149] T. Hinderer, Astrophys. J. **677**, 1216 (2008).
[150] K. Hotokezaka, K. Kyotoku, H. Okawa, M. Shibata, and K. Kiuchi, Phys. Rev. D **83**, 124008 (2011).
[151] B. S. Sathyaprakash and S. V. Dhurandhar, Phys. Rev. D **44**, 3819 (1991).
[152] L. Blanchet, Liv. Rev. Rel. **17**, 2 (2014).
[153] A. Buonanno, B. R. Iyer, E. Ochsner, Y. Pan, and B. S. Sathyaprakash, Phys. Rev. D **80**, 084043 (2009).
[154] A. Bohé, S. Marsat, and L. Blanchet, Class. Quantum Grav. **30**, 135009 (2013).
[155] K. G. Arun, A. Buonanno, G. Faye, and E. Ochsner, Phys. Rev. D **79**, 104023 (2009); **84**, 049901 (2011) [erratum].
[156] B. Mikóczi, M. Vasúth, and L. Á. Gergely, Phys. Rev. D **71**, 124043 (2005).
[157] M. Pürrer, Phys. Rev. D **93**, 064041 (2016).
[158] B. Margalit and B. D. Metzger, Astrophys. J. Lett. **850**, L19 (2017).
[159] A. Bauswein, O. Just, H.-T. Janka, and N. Stergioulas, Astrophys. J. Lett. **850**, L34 (2017).
[160] M. Ruiz, S. L. Shapiro, and A. Tsokaros, Phys. Rev. D **97**, 021501(R) (2018).
[161] E. Annala, T. Gorda, A. Kurkela, and A. Vuorinen, Phys. Rev. Lett. **120**, 172703 (2018).
[162] E.-P. Zhou, X. Zhou, and A. Li, Phys. Rev. D **97**, 083015 (2018).
[163] F. J. Fattoyev, J. Piekarewicz, and C. J. Horowitz, Phys. Rev. Lett. **120**, 172702 (2018).
[164] V. Paschalidis, K. Yagi, D. Alvarez-Castillo, D. B. Blaschke, and A. Sedrakian, Phys. Rev. D **97**, 084038 (2018).
[165] R. Nandi and P. Char, Astrophys. J. **857**, 12 (2018).
[166] E. R. Most, L. R. Weih, L. Rezzolla, and J. Schaner-Bielich, Phys. Rev. Lett. **120**, 261103 (2018).
[167] C. A. Raithel, F. Özel and D. Psaltis, Astrophys. J. Lett. **857**, L23 (2018).
[168] P. Landry and R. Essick, Phys. Rev. D **99**, 084049 (2019).
[169] T. Narikawa, N. Uchikata, K. Kawaguchi, K. Kiuchi, K. Kyotoku, M. Shibata, and H. Tagoshi, Phys. Rev. Research **1**, 033055 (2019).
[170] B. P. Abbott et al. [LIGO Scientific and Virgo Collaborations], Astrophys. J. Lett. **892**, L3 (2020).
[171] C. Meegan et al., Astrophys. J. **702**, 791 (2009).
[172] A. Goldstein et al., Astrophys. J. Lett. **848**, L14 (2017).
[173] V. Savchenko et al., Astrophys. J. Lett. **848**, L15 (2017).
[174] W. B. Atwood et al., Astrophys. J. **697**, 1071 (2009).
[175] E. Burns et al., Astrophys. J. Lett. **863**, L34 (2018).
[176] E. Troja et al., Nature Commun. **9**, 4089 (2018).
[177] A. von Kienlin et al., Astrophys. J. **876**, 89 (2019).
[178] T. Matsumoto and T. Piran, Mon. Not. R. Astron. Soc. **492**, 4283 (2020).
[179] A. J. Levan, J. Hjorth, K. Wiersema, and N. R. Tanvir GCN Circ. 17281 (2015).
[180] M. Matsuoka et al., Pub. Astron. Soc. Japan **61**, 999 (2009).
[181] T. Mihara et al., Pub. Astron. Soc. Japan **63**, S623 (2011).
[182] M. Sugizaki et al., Pub. Astron. Soc. Japan **63**, 635 (2011).
[183] S. Sugita, N. Kawai, S. Nakahira, H. Negoro, M. Serino, T. Mihara, K. Yamaoka, and M. Nakajima, Pub. Astron. Soc. Japan **70**, 81 (2018).
[184] P. A. Evans et al., Science **9580**, 1 (2017).
[185] A. Hajela et al., Astrophys. J. Lett. **886**, L17 (2019).
[186] N. Gehrels et al., Astrophys. J. **611**, 1005 (2004).
[187] S. D. Barthelmy et al., Space Sci. Rev. **120**, 143 (2005).
[188] D. N. Burrows et al., Space Sci. Rev. **120**, 165 (2005).
[189] P. W. A. Roming et al., Space Sci. Rev. **120**, 95 (2005).
[190] S. D. Barthelmy et al., GCN Circ. 21931 (2017).
[191] S. Torii [CALET Collaboration], PoS **ICRC2017**, 1092 (2017).
[192] Y. Asaoka et al., Astropart. Phys. **100**, 29 (2018).
[193] K. Yamaoka et al., Proc. 7th Huntsville Gamma-Ray Burst Symp. (2013).

[194] O. Adriani et al., Astrophys. J. **863**, 160 (2018).
[195] E. Troja et al., Nature **551**, 71 (2017).
[196] A. Hajela et al., Astrophys. J. Lett. **886**, L17 (2019).
[197] E. Troja, H. van Eerten, G. Ryan, R. Ricci, J. M. Burgess, M. H. Wieringa, L. Piro, S. B. Cenko, and T. Sakamoto, Mon. Not. R. Astron. Soc. **489**, 1919 (2019).
[198] L. Piro et al., Mon. Not. R. Astron. Soc. **483**, 1912 (2019).
[199] K. P. Mooley et al., Astrophys. J. Lett. **868**, L11 (2018).
[200] G. P. Lamb et al., Astrophys. J. Lett. **870**, L15 (2019).
[201] M. M. Kasliwal et al., Science **358**, 1559 (2017).
[202] O. Gottlieb, E. Nakar, T. Piran, and K. Hotokezaka, Mon. Not. R. Astron. Soc. **479**, 588 (2018).
[203] E. Nakar, O. Gottlieb, T. Piran, M. M. Kasliwal, and G. Hallinan, Astrophys. J. **867**, 18 (2018).
[204] H. Nagakura, K. Hotokezaka, Y. Sekiguchi, M. Shibata, and K. Ioka, Astrophys. J. Lett. **784**, L28 (2014).
[205] A. Murguia-Berthier, G. Montes, E. Ramirez-Ruiz, F. De Colle, and W. H. Lee, Astrophys. J. **788**, L8 (2014).
[206] H. Hamidani, K. Kiuchi, and K. Ioka, Mon. Not. R. Astron. Soc. **491**, 3192 (2020).
[207] K. P. Mooley et al., Nature **554**, 207 (2018).
[208] P. D'Avanzo et al., Astron. Astrophys. **613**, L1 (2018).
[209] D. Lazzati, R. Perna, B. J. Morsony, D. Lopez-Camara, M. Cantiello, R. Ciolfi, B. Giacomazzo, and J. C. Workman, Phys. Rev. Lett. **120**, 241103 (2018).
[210] J. D. Lyman et al., Nature Astron. **2**, 751 (2018).
[211] R. Margutti et al., Astrophys. J. Lett. **856**, L18 (2018).
[212] J. J. Ruan, M. Nynka, D. Haggard, V. Kalogera, and P. Evans, Astrophys. J. Lett. **853**, L4 (2018).
[213] E. Troja, L. Piro, G. Ryan, H. van Eerten, R. Ricci, M. H. Wieringa, S. Lotti, T. Sakamoto, and S. B. Cenko, Mon. Not. R. Astron. Soc. **478**, L18 (2018).
[214] P. Mészáros, M. J. Rees, and R. A. M. J. Wijers, Astrophys. J. **499**, 301 (1998).
[215] B. Zhang and P. Mészáros, Astrophys. J. **571**, 876 (2002).
[216] K. Takahashi and K. Ioka, Mon. Not. Roy. Astron. Soc. **497**, 1217 (2020) [arXiv:1912.01871 [astro-ph.HE]] [Search INSPIRE].
[217] L. Amati et al., Astron. Astrophys. **390**, 81 (2002).
[218] D. Yonetoku, T. Murakami, T. Nakamura, R. Yamazaki, A. K. Inoue, and K. Ioka, Astrophys. J. **609**, 935 (2004).
[219] T. Matsumoto, E. Nakar, and T. Piran, Mon. Not. R. Astron. Soc. **483**, 1247 (2019).
[220] T. Matsumoto, E. Nakar, and T. Piran, Mon. Not. R. Astron. Soc. **486**, 1563 (2019).
[221] S. Kisaka, K. Ioka, K. Kashiyama, and T. Nakamura, Astrophys. J. **867**, 39 (2018).
[222] J. M. Lattimer and D. N. Schramm, Astrophys. J. **192**, 145 (1974).
[223] J. M. Lattimer and D. N. Schramm, Astrophys. J. **210**, 549 (1976).
[224] D. Eichler, M. Livio, T. Piran, and D. N. Schramm, Nature **340**, 126 (1989).
[225] C. Freiburghaus, S. Rosswog, and F.-K. Thielemann, Astrophys. J. **525**, L121 (1999).
[226] L. F. Roberts, D. Kasen, W. H. Lee, and E. Ramirez-Ruiz, Astrophys. J. Lett. **736**, L21 (2011).
[227] S. Goriely, A. Bauswein, and H.-T. Janka, Astrophys. J. Lett. **738**, L32 (2011).
[228] O. Korobkin, S. Rosswog, A. Arcones, and C. Winteler, Mon. Not. R. Astron. Soc. **426**, 1940 (2012).
[229] A. Bauswein, S. Goriely, and H.-T. Janka, Astrophys. J. **773**, 78 (2013).
[230] S. Wanajo, Y. Sekiguchi, N. Nishimura, K. Kiuchi, K. Kyotoku, and M. Shibata, Astrophys. J. Lett. **789**, L39 (2014).
[231] S. Rosswog, M. Liebendörfer, F.-K. Thielemann, M. B. Davies, W. Benz, and T. Piran, Astron. Astrophys. **341**, 499 (1999).
[232] S. Rosswog, Astrophys. J. **634**, 1202 (2005).
[233] S. Rosswog, R. Soc. Lon. Phil. Trans. A **371**, 20272 (2013).
[234] K Hotokezaka, K. Kiuchi, K. Kyotoku, H. Okawa, Y.-i. Sekiguchi, M. Shibata, and K. Taniguchi, Phys. Rev. D **87**, 024001 (2013).
[235] L.-X. Li and B. Paczyński, Astrophys. J. Lett. **507**, 59 (1998).
[236] S. R. Kulkarni, arXiv:astro-ph/0510256 [Search INSPIRE].
[237] B. D. Metzger, G. Martínez-Pinedo, S. Darbha, E. Quataert, A. Arcones, D. Kasen, R. Thomas, P. Nugent, I. V. Panov, and N. T. Zinner, Mon. Not. R. Astron. Soc. **406**, 2650 (2010).
[238] D. Kasen, N. R. Badnell, and J. Barnes, Astrophys. J. **774**, 25 (2013).

[239] J. Barnes and D. Kasen, Astrophys. J. **775**, 18 (2013).
[240] M. Tanaka and K. Hotokezaka, Astrophys. J. **775**, 113 (2013).
[241] T. Morokuma et al., Pub. Astron. Soc. Japan **68**, 40 (2016).
[242] B. P. Abbott et al. [LIGO Scientific and Virgo Collaborations], Phys. Rev. Lett. **116**, 241103 (2016) [arXiv:1606.04855 [gr-qc]] [Search INSPIRE].
[243] M. Yoshida et al., Pub. Astron. Soc. Japan **69**, 9 (2017).
[244] Y. Ustumi et al., Pub. Astron. Soc. Japan **70**, 1 (2018).
[245] I. Andreoni et al., Pub. Astron. Soc. Aus. **34**, e069 (2017).
[246] I. Arcavi et al., Nature **551**, 64 (2017).
[247] R. Chornock et al., Astrophys. J. Lett. **848**, L19 (2017).
[248] D. A. Coulter et al., Science **358**, 1556 (2017).
[249] P. S. Cowperthwaite et al., Astrophys. J. Lett. **848**, L17 (2017).
[250] M. C. Díaz et al., Astrophys. J. Lett. **848**, L29 (2017).
[251] M. R. Drout et al., Science **358**, 1570 (2017).
[252] P. A. Evans et al., Science **358**, 1565 (2017).
[253] M. M. Kasliwal et al., Science **358**, 1559 (2017).
[254] C. D. Kilpatrick et al., Science **358**, 1583 (2017).
[255] V. M. Lipunov et al., Astrophys. J. Lett. **850**, L1 (2017).
[256] C. McCully et al., Astrophys. J. Lett. **848**, L32 (2017).
[257] M. Nicholl et al., Astrophys. J. Lett. **848**, L18 (2017).
[258] E. Pian et al., Nature **551**, 67 (2017).
[259] B. J. Shappee et al., Science **358**, 1574 (2017).
[260] M. R. Siebert et al., Astrophys. J. Lett. **848**, L26 (2017).
[261] S. J. Smartt et al., Nature **551**, 75 (2017).
[262] M. Soares-Santos et al., Astrophys. J. Lett. **848**, L16 (2017).
[263] N. R. Tanvir et al., Astrophys. J. Lett. **848**, L27 (2017).
[264] N. Tominaga et al., Pub. Astron. Soc. Japan **70**, 28 (2018).
[265] E. Troja et al., Nature **551**, 71 (2017).
[266] Y. Utsumi et al., Pub. Astron. Soc. Japan **69**, 101 (2017).
[267] S. Valenti et al., Astrophys. J. Lett. **848**, L24 (2017).
[268] M. Tanaka et al., Pub. Astron. Soc. Japan **69**, 102 (2017).
[269] M Shibata, S. Fujibayashi K. Hotokezaka, K. Kiuchi, K Kyutoku, Y Sekiguchi, and M Tanaka, Phys. Rev. D **96**, 123012 (2017).
[270] S. Fujibayashi, K. Kiuchi, N. Nishimura, Y. Sekiguchi, and M. Shibata, Astrophys. J. **860**, 64 (2018).
[271] K. Kawaguchi, M. Shibata, and M. Tanaka, Astrophys. J. Lett. **865**, L21 (2018).
[272] M. Tanaka, D. Kato, G. Gaigalas, and K. Kawaguchi, Mon. Not. R. Astron. Soc. **496**, 1369 (2020).
[273] K. Kawaguchi, M. Shibata, and M. Tanaka, Astrophys. J. **889**, 171 (2020).
[274] T. Ohgami et al., Pub. Astron. Soc. Japan **73**, 350 (2021).
[275] S. M. Gaebel and J. Veitch, Class. Quantum Grav. **34**, 174003 (2017).
[276] M. Doi et al., Proc. SPIE **10700**, 107000W (2018).
[277] F. A. Rasio and S. L. Shapiro Class. Quantum Grav. **16**, R1 (1999).
[278] H. Dimmelmeier, C. D. Ott, A. Marek, and H.-T. Janka, Phys. Rev. D **78**, 064056 (2008).
[279] S. Scheidegger, R. Käppeli, S. C. Whitehouse, T. Fischer, and M. Liebendörfer, Astron. Astrophys. **514**, A51 (2010).
[280] P. Cerdá-Durán, N. DeBrye, M. A. Aloy, J. A. Font, and M. Obergaulinger, Astrophys. J. Lett. **779**, L18 (2013).
[281] C. D. Ott, E. Abdikamalov, P. Mösta, R. Haas, S. Drasco, E. P. O'Connor, C. Reisswig, C. A. Meakin, and E. Schnetter, Astrophys. J. **768**, 115 (2013).
[282] K. N. Yakunin et al., Phys. Rev. D **92**, 084040 (2015).
[283] T. Kuroda, T. Takiwaki, and K. Kotake, Phys. Rev. D **89**, 044011 (2014).
[284] K.-C. Pan, M. Liebendörfer, S. M. Couch, and F.-K. Thielemann, Astrophys. J. **857**, 13 (2018).
[285] V. Morozova, D. Radice, A. Burrows, and D. Vartanyan, Astrophys. J. **861**, 10 (2018).
[286] K. Kotake, C. R. Phys. **14**, 318 (2013).
[287] A. Heger, S. E. Woosley, and H. C. Spruit, Astrophys. J. **626**, 350 (2005).
[288] T. Takiwaki, K. Kotake, and Y. Suwa, Mon. Not. R. Astron. Soc. **461**, L112 (2016).
[289] A. Summa, H.-T. Janka, T. Melson, and A Marek, Astrophys. J. **852**, 28 (2018).

[290] T. Foglizzo et al., Pub. Astron. Soc. Aus. **32**, e009 (2015).
[291] E. Muller and H.-T. Janka, Astron. Astrophys. **317**, 140 (1997).
[292] E. Muller, M. Rampp, R. Buras, H.-T. Janka, and D. H. Shoemaker, Astrophys. J. **603**, 221 (2004).
[293] J. W. Murphy, C. D. Ott, and A. Burrows, Astrophys. J. **707**, 1173 (2009).
[294] K. Kotake, W. Iwakami, N. Ohnishi, and S. Yamada, Astrophys. J. **697**, L133 (2009).
[295] B. Müller, H.-T. Janka, and A. Marek, Astrophys. J. **766**, 43 (2013).
[296] A. Torres-Forné, P. Cerdá-Duran, M. Obergaulinger, B. Müller, and J. A. Font, Phys. Rev. Lett. **123**, 051102 (2019).
[297] H. Andresen, B. Müller, E. Müller, and H.-T. Janka, Mon. Not. R. Astron. Soc. **468**, 2032 (2017).
[298] T. Kuroda, K. Kotake, and T. Takiwaki, Astrophys. J. Lett. **829**, L14 (2016).
[299] D. Radice, V. Morozova, A. Burrows, D. Vartanyan, and H. Nagakura, Astrophys. J. Lett. **876**, L9 (2019).
[300] H. Andresen, E. Müller, H.-T. Janka, A. Summa, K. Gill, and M. Zanolin, Mon. Not. R. Astron. Soc. **486**, 2238 (2019).
[301] S. E. Woosley and T. A. Weaver, Astrophys. J. Supp. **101**, 181 (1995).
[302] H. Kawahara, T. Kuroda, T. Takiwaki, K. Hayama, and K. Kotake, Astrophys. J. **867**, 126 (2018).
[303] L. Cohen, Time Frequency Analysis: Theory and Applications (Prentice-Hall, Inc., Upper Saddle River, NJ, 1995).
[304] L. Stankovic, M. Dakovic, and T. Thayaparan, TimeFrequency Signal Analysis with Applications (Artech House Publishers, Boston, MA, 2013).
[305] B. Boashash, TimeFrequency Signal Analysis and Processing, 2nd ed. (Elsevier, Amsterdam, 2015).
[306] A. Torres-Forné, P. Cerdá-Durán, A. Passamonti, M. Obergaulinger, and J. A. Font, Mon. Not. R. Astron. Soc. **482**, 3967 (2019).
[307] K. Hayama, T. Kuroda, K. Nakamura, and S. Yamada, Phys. Rev. Lett. **116**, 151102 (2016).
[308] K. Hayama, T. Kuroda, K. Kotake, and T. Takiwaki, Mon. Not. R. Astron. Soc. Lett. **477**, L96 (2018).
[309] A. W. Steiner, M. Hempel, and T. Fischer, Astrophys. J. **774**, 17 (2013).
[310] K. Hayama, T. Kuroda, K. Kotake, and T. Takiwaki, Phys. Rev. D **92**, 122001 (2015).
[311] C. D. Ott, Class. Quantum Grav. **26**, 063001 (2009).
[312] S. E. Woosley and A. Heger, Astrophys. J. **637**, 914 (2006).
[313] S. Suvorova, J. Powell, and A. Melatos, Phys. Rev. D **99**, 123012 (2019).
[314] S. E. Gossan, P. Sutton, A. Stuver, M. Zanolin, K. Gill, and C.D. Ott, Phys. Rev. D **93**, 042002 (2016).
[315] T. Takiwaki and K. Kotake, Mon. Not. R. Astron. Soc. **475**, L91 (2018).
[316] S. Hild, A. Freise, M. Mantovani, S. Chelkowski, J. Degallaix, and R. Schilling, Class. Quantum Grav. **26**, 025005 (2009).
[317] Y. Aso, Y. Michimura, K. Somiya, M. Ando, O. Miyakawa, T. Sekiguchi, D. Tatsumi, and H. Yamamoto [KAGRA Collaboration], Phys. Rev. D **88**, 043007 (2013).
[318] L. Walk, I. Tamborra, H.-T. Janka, and A. Summa, Phys. Rev. D **98**, 123001 (2018).
[319] L. Walk, I. Tamborra, H.-T. Janka, and A. Summa, Phys. Rev. D **100**, 063018 (2019).
[320] K. Belczynski, M. Dominik, T. Bulik, R. O'Shaughnessy, C. Fryer, and D. E. Holz, Astrophys. J. Lett. **715**, L138 (2010).
[321] N. Langer, Ann. Rev. Astron. Astrophys. **50**, 107 (2012).
[322] T. Kinugawa, H. Nakano, and T. Nakamura, Prog. Theor. Exp. Phys. 103E01 (2015).
[323] C. L. Fryer, S. E. Woosley, and D. H. Hartmann, Astrophys. J. **526**, 152 (1999).
[324] K.-C. Pan, M. Liebendörfer, S. M. Couch, and F.-K. Thielemann, Astrophys. J. **857**, 13 (2018).
[325] M. Liebendörfer, S. C. Whitehouse, and T. Fischer, Astrophys. J. **698**, 1174 (2009).
[326] C. Chan, B. Müller, A. Heger, R. Pakmor, and V. Springel, Astrophys. J. Lett. **852**, L19 (2018).
[327] K. Takahashi, H. Umeda, and T. Yoshida Astrophys. J. **794**, 40 (2014).
[328] M. Shibata, K. Kiuchi, Y.-i. Sekiguchi, and Y. Suwa, Prog. Theor. Phys. **125**, 1255 (2011).
[329] T. Kuroda, K. Kotake, T. Takiwaki, and F.-K. Thielemann, Mon. Not. R. Astron. Soc. **477**, L80 (2018).
[330] M. Shibata and T. Nakamura, Phys. Rev. D **52**, 5428 (1995).
[331] T. W. Baumgarte and S. L. Shapiro, Phys. Rev. D **59**, 024007 (1998).
[332] J. Thornburg, Class. Quantum Grav. **21**, 743 (2004).
[333] J. M. Lattimer and F. Swesty, Nucl. Phys. A **535**, 331 (1991).
[334] M. Liebendörfer, O. E. B. Messer, A. Mezzacappa, S. W. Bruenn, C. Y. Cardall, and F.-K. Thielemann, Astrophys. J. Supp. **150**, 263 (2004).

[335] T. Fischer, S. C. Whitehouse, A. Mezzacappa, F. K. Thielemann, and M. Liebendörfer, Astron. Astrophys. **499**, 1 (2009).
[336] K. Sumiyoshi, S. Yamada, and H. Suzuki, Astrophys. J. **667**, 382 (2007).
[337] C. Lunardini, Phys. Rev. Lett. **102**, 231101 (2009).
[338] S. Horiuchi, K. Sumiyoshi, K. Nakamura, T. Fischer, A. Summa, T. Takiwaki, H.-T. Janka, and K. Kotake, Mon. Not. R. Astron. Soc. **475**, 1363 (2018).
[339] B. Müller, H.-T. Janka, and A. Marek, Astrophys. J. **766**, 43 (2013).
[340] A. Torres-Forné, P. Cerdá-Durán, A. Passamonti, M. Obergaulinger, and J. A. Font, Mon. Not. R. Astron. Soc. **482**, 3967 (2019).
[341] V. Morozova, D. Radice, A. Burrows, and D. Vartanyan, Astrophys. J. **861**, 10 (2018).
[342] H. Sotani, T. Kuroda, T. Takiwaki, and K. Kotake, Phys. Rev. D **96**, 063005 (2017).
[343] E. Abdikamalov, G. Pagliaroli, and D. Radice, arXiv:2010.04356 [astro-ph.SR] [Search INSPIRE].
[344] K. Sumiyoshi and S. Yamada, Astrophys. J. Supp. **199**, 17 (2012).
[345] A. Harada, H. Nagakura, W. Iwakami, H. Okawa, S. Furusawa, H. Matsufuru, K. Sumiyoshi, and S. Yamada, Astrophys. J. **872**, 181 (2019).
[346] H. Nagakura, K. Sumiyoshi, and S. Yamada, Astrophys. J. **878**, 160 (2019).
[347] H. T. Janka, in Handbook of Supernovae, eds. A. W. Alsabti and P. Murdin (Springer, Cham, 2017), p. 1575.
[348] B. Müller, Ann. Rev. Nucl. Part. Sci. **69**, 253 (2019).
[349] A. Marek, H.-T. Janka, and E. Müller, Astron. Astrophys. **496**, 475 (2009).
[350] T. Yokozawa, M. Asano, T. Kayano, Y. Suwa, N. Kanda, Y. Koshio, and M. R. Vagins, Astrophys. J. **811**, 86 (2015).
[351] K. Abe et al. [Hyper-Kamiokande Proto-Collaboration], arXiv:1805.04163 [physics.ins-det] [Search INSPIRE].
[352] K. Abe et al. [Hyper-Kamiokande Collaboration], arXiv:2101.05269 [astro-ph.IM] [Search INSPIRE].
[353] S. Al Kharusi et al., New J. Phys. **23**, 031201 (2021) [arXiv:2011.00035 [astro-ph.HE]] [Search INSPIRE].
[354] J. F. Beacom and M. R. Vagins, Phys. Rev. Lett. **93**, 171101 (2004).
[355] L. Marti et al., Nucl. Instrum. Meth. A **959**, 163549 (2020) [arXiv:1908.11532 [physics.ins-det]] [Search INSPIRE].
[356] K. Sumiyoshi and S. Yamada, Astrophys. J. Supp. **199**, 17 (2012).
[357] H. Nagakura, K. Sumiyoshi, and S. Yamada, Astrophys. J. Supp. **214**, 16 (2014).
[358] H. Nagakura, W. Iwakami, S. Furusawa, K. Sumiyoshi, S. Yamada, H. Matsufuru, and A. Imakura, Astrophys. J. Supp. **229**, 42 (2017).
[359] H. Nagakura, W. Iwakami, S. Furusawa, H. Okawa, A. Harada, K. Sumiyoshi, S. Yamada, H. Matsufuru, and A. Imakura, Astrophys. J. **854**, 136 (2018).
[360] J. M. Lattimer and F. D. Swesty, Nucl. Phys. A **535**, 331 (1991).
[361] S. Furusawa, K. Sumiyoshi, S. Yamada, and H. Suzuki, Astrophys. J. **772**, 95 (2013).
[362] S. E. Woosley, A. Heger, and T. A. Weaver, Rev. Mod. Phys. **74**, 1015 (2002).
[363] A. Harada, H. Nagakura, W. Iwakami, H. Okawa, S. Furusawa, H. Matsufuru, K. Sumiyoshi, and S. Yamada, Astrophys. J. **872**, 181 (2019).
[364] A. Heger, N. Langer, and S. E. Woosley, Astrophys. J. **528**, 368 (2000).
[365] H. Nagakura, K. Sumiyoshi, and S. Yamada, Astrophys. J. Lett. **880**, L28 (2019).
[366] H. Togashi, K. Nakazato, Y. Takehara, S. Yamamuro, H. Suzuki, and M. Takano, Nucl. Phys. A **961**, 78 (2017).
[367] L. Scheck, K. Kifonidis, H.-Th. Janka, and E. Müeller, Astron. Astrophys. **457**, 963 (2006).
[368] K. Nakazato, K. Sumiyoshi, H. Suzuki, T. Totani, H. Umeda, and S. Yamada, Astrophys. J. Supp. **205**, 2 (2013).
[369] T. Totani, K. Sato, H. E. Dalhed, and J. R. Wilson, Astrophys. J. **496**, 216 (1998).
[370] K. Sumiyoshi, S. Yamada, S. Suzuki, H. Shen, S. Chiba, and H. Toki, Astrophys. J. **629**, 922 (2005).
[371] S. Yamada, Astrophys. J. **475**, 720 (1997).
[372] H. Suzuki, in Physics and Astrophysics of Neutrinos, eds. M. Fukugita and A. Suzuki (Springer, Tokyo, 1994), p. 763.
[373] K. Nakazato, H. Suzuki, and H. Togashi, Phys. Rev. C **97**, 035804 (2018).
[374] Y. Suwa, K. Sumiyoshi, K. Nakazato, Y. Takahira, Y. Koshio, M. Mori, and R. A. Wendell, Astrophys. J. **881**, 139 (2019).

[375] K. Sumiyoshi, S. Yamada, and H. Suzuki, Astrophys. J. **667**, 382 (2007).
[376] K. Sumiyoshi, S. Yamada, H. Suzuki, and S. Chiba, Phys. Rev. Lett. **97**, 091101 (2006).
[377] K. Nakazato, K. Sumiyoshi, H. Suzuki, and S. Yamada, Phys. Rev. D **81**, 083009 (2010).
[378] H. Sotani and K. Sumiyoshi, Phys. Rev. D **100**, 083008 (2019).
[379] S. Horiuchi, K. Sumiyoshi, K. Nakamura, T. Fischer, A. Summa, T. Takiwaki, H.-T. Janka, and K. Kotake, Mon. Not. R. Astron. Soc. **475**, 1363 (2018).
[380] H. Shen, H. Toki, K. Oyamatsu, and K. Sumiyoshi, Nucl. Phys. A **637**, 435 (1998).
[381] H. Shen, H. Toki, K. Oyamatsu, and K. Sumiyoshi, Prog. Theor. Phys. **100**, 1013 (1998).
[382] H. Shen, H. Toki, K. Oyamatsu, and K. Sumiyoshi, Astrophys. J. Supp. **197**, 20 (2011).
[383] M. Oertel, M. Hempel, T. Klähn, and S. Typel, Rev. Mod. Phys. **89**, 015007 (2017).
[384] H. Shen, F. Ji, J. Hu, and K. Sumiyoshi, Astrophys. J. **891**, 148 (2020) [arXiv:2001.10143 [nucl-th]] [Search INSPIRE].
[385] S. Furusawa, K. Sumiyoshi, S. Yamada, and H. Suzuki, Nucl. Phys. A **957**, 188 (2017).
[386] S. Furusawa, H. Togashi, H. Nagakura, K. Sumiyoshi, S. Yamada, H. Suzuki, and M. Takano, J. Phys. G: Nucl. Part. Phys. **44**, 094001 (2017).
[387] H. Togashi, K. Nakazato, Y. Takehara, S. Yamamuro, H. Suzuki, and M. Takano, Nucl. Phys. A **961**, 78 (2017).
[388] T. Dannert, A. Marek, and M. Rampp, Adv. Par. Comp. **25**, 305 (2014).
[389] H. Matsufuru and K. Sumiyoshi, Simulation of supernova explosion accelerated on GPU: Spherically symmetric neutrino-radiation hydrodynamics, in Computational Science and its Applications, eds. O. Gervasi et al. (Springer, New York, 2018).
[390] H. Matsufuru, and K. Sumiyoshi, Proc. 6th Int. Symp. Computing and Networking Workshops (2018).
[391] A. Imakura, T. Sakurai, K. Sumiyoshi, and H. Matsufuru, Japan Soc. Ind. Appl. Math. Lett. **4**, 41 (2012).
[392] E. S. Quintana, G. Quintana, X. Sun, and R. van de Geijn, SIAM J. Sci. Comput. **22**, 1762 (2001).
[393] K. Yagi and T. Tanaka, Phys. Rev. D **81**, 064008 (2010); **81**, 109902 (2010) [erratum] [arXiv:0906.4269 [gr-qc]] [Search INSPIRE].
[394] S. Khan, K. Chatziioannou, M. Hannam, and F. Ohme, Phys. Rev. D **100**, 024059 (2019) [arXiv:1809.10113 [gr-qc]] [Search INSPIRE].
[395] P. C. Peters, Phys. Rev. **136**, B1224 (1964).
[396] C. F. B. Macedo, P. Pani, V. Cardoso, and L. C. B. Crispino, Astrophys. J. **774**, 48 (2013).
[397] H. S. Zhao and J. Silk, Phys. Rev. Lett. **95**, 011301 (2005).
[398] G. Bertone, A. R. Zentner, and J. Silk, Phys. Rev. D **72**, 103517 (2005).
[399] K. Eda, Y. Itoh, S. Kuroyanagi, and J. Silk, Phys. Rev. Lett. **110**, 221101 (2013).
[400] K. Eda, Y. Itoh, S. Kuroyanagi, and J. Silk, Phys. Rev. D **91**, 044045 (2015).
[401] X.-J. Yue and W.-B. Han, Phys. Rev. D **97**, 064003 (2018).
[402] O. A Hannuksela, K. C. Y. Ng, and T. G. F. Li, Phys. Rev. D **102**, 103022 (2020) [arXiv:1906.11845 [astro-ph.CO]] [Search INSPIRE].
[403] B. J. Kavanagh, D. A. Nichols, G. Bertone, and D. Gaggero, Phys. Rev. D **102**, 083006 (2020) [arXiv:2002.12811 [gr-qc]] [Search INSPIRE].
[404] K. D. Kokkotas and B. G. Schmidt, Liv. Rev. Rel. **2**, 2 (1999).
[405] E. Berti, V. Cardoso, and C. M. Will, Phys. Rev. D **73**, 064030 (2006).
[406] E. Berti, Ringdown (Johns Hopkins University, Baltimore, MD, 2021) (available at: https://pages.jh.edu/eberti2/ringdown/, date last accessed April 17, 2021).
[407] H. Nakano, H. Takahashi, H. Tagoshi, and M. Sasaki, Phys. Rev. D **68**, 102003 (2003).
[408] H. Nakano, H. Takahashi, H. Tagoshi, and M. Sasaki, Prog. Theor. Phys. **111**, 781 (2004).
[409] S. D. Mohanty, Phys. Rev. D **57**, 630 (1998).
[410] K. Sakai, K.-i. Oohara, H. Nakano, M. Kaneyama, and H. Takahashi, Phys. Rev. D **96**, 044047 (2017).
[411] J. Meidam et al., Phys. Rev. D **97**, 044033 (2018).
[412] F. Pretorius, Phys. Rev. Lett. **95**, 121101 (2005).
[413] M. Campanelli, C. O. Lousto, P. Marronetti, and Y. Zlochower, Phys. Rev. Lett. **96**, 111101 (2006).
[414] J. G. Baker, J. Centrella, D.-I. Choi, M. Koppitz, and J. van Meter, Phys. Rev. Lett. **96**, 111102 (2006).
[415] O. Dreyer, B. Kelly, B. Krishnan, L. S. Finn, D. Garrison, and R. Lopez-Aleman, Class. Quantum Grav. **21**, 787 (2004).
[416] E. Berti, J. Cardoso, E. Cardoso, and M. Cavaglià, Phys. Rev. D **76**, 104044 (2007).
[417] S. Gossan, J. Veitch, and B. S. Sathyaprakash Phys. Rev. D **85**, 124056 (2012).

[418] H. Nakano, T. Tanaka, and T. Nakamura, Phys. Rev. D **92**, 064003 (2015).
[419] H. Nakano, T. Narikawa, K.-i. Oohara, K. Sakai, H.-a. Shinkai, H. Takahashi, T. Tanaka, N. Uchikata, S. Yamamoto, and T. S. Yamamoto, Phys. Rev. D **99**, 124032 (2019).
[420] N. Yunes and F. Pretorius, Phys. Rev. D **80**, 122003 (2009) [arXiv:0909.3328 [gr-qc]] [Search INSPIRE].
[421] C. K. Mishra, K. G. Arun, B. R. Iyer and B. S. Sathyaprakash, Phys. Rev. D **82**, 064010 (2010).
[422] M. Agathos, W. Del Pozzo, T. G. F. Li, C. Van Den Broeck, J. Veitch and S. Vitale, Phys. Rev. D **89**, 082001 (2014).
[423] B. P. Abbott et al. [LIGO Scientific and Virgo Collaborations], Phys. Rev. Lett. **123**, 011102 (2019).
[424] H. Takeda,, S. Morisaki, and A. Nishizawa, Phys. Rev. D **103**, 064037 (2021) [arXiv:2010.14538 [gr-qx]] [Search INSPIRE].
[425] A. Nishizawa A. Taruya K. Hayama S. Kawamura, and M.-a. Sakagami, Phys. Rev. D **79**, 082002 (2009).
[426] E. Poisson and C. M. Will, Gravity (Cambridge University Press, Cambridge, 2014).
[427] B. F. Schutz and M. Tinto, Mon. Not. R. Astron. Soc. **224**, 131 (1987).
[428] K. Hayama and A. Nishizawa, Phys. Rev. D **87**, 062003 (2013).
[429] H. Takeda, A. Nishizawa, Y. Michimura, K. Nagano, K. Komori, M. Ando, and K. Hayama, Phys. Rev. D **98**, 022008 (2018).
[430] S. Hild et al., Class. Quantum Grav. **28**, 094013 (2011).
[431] B. P. Abbott et al., Class. Quantum Grav. **34**, 044001 (2017).
[432] H. Takeda, A. Nishizawa, K. Nagano, Y. Michimura, K. Komori, M. Ando, and K. Hayama, Phys. Rev. D **100**, 042001 (2019).
[433] Y. Hagihara, N. Era, D. Iikawa, and H. Asada, Phys. Rev. D **98**, 064035 (2018).
[434] Y. Hagihara, N. Era, D. Iikawa, A. Nishizawa, and H. Asada, Phys. Rev. D **100**, 064010 (2019).
[435] Y. Hagihara, N. Era, D. Iikawa, N. Takeda, and H. Asada, Phys. Rev. D **101**, 041501(R) (2020).
[436] C. Brans and R. H. Dicke, Phys. Rev. **124**, 925 (1961).
[437] C. M. Will and H. W. Zaglauer, Astrophys. J. **346**, 366 (1989).
[438] T. Damour and G. Esposito-Farese, Class. Quantum Grav. **9**, 2093 (1992).
[439] G. W. Horndeski, Int. J. Theor. Phys. **10**, 363 (1974).
[440] D. Langlois and K. Noui, J. Cosmol. Astropart. Phys. **1602**, 034 (2016).
[441] M. Crisostomi, K. Koyama, and G. Tasinato, J. Cosmol. Astropart. Phys. **1604**, 044 (2016).
[442] J. Ben Achour, M. Crisostomi, K. Koyama, D. Langlois, K. Noui, and G. Tasinato, J. High Energy Phys. **1612**, 100 (2016).
[443] T. Kobayashi, Rept. Prog. Phys. **82**, 086901 (2019).
[444] T. Kobayashi, Y. Watanabe, and D. Yamauchi, Phys. Rev. D **91**, 064013 (2015).
[445] T. Kobayashi and T. Hiramatsu Phys. Rev. D **97**, 104012 (2018).
[446] P. Creminelli, M. Lewandowski, G. Tambalo, and F. Vernizzi, J. Cosmol. Astropart. Phys. **1812**, 025 (2018).
[447] P. Creminelli, G. Tambalo, F. Vernizzi, and V. Yingcharoenrat, J. Cosmol. Astropart. Phys. **1910**, 072 (2019).
[448] S. Hirano, T. Kobayashi, and D. Yamauchi, Phys. Rev. D **99**, 104073 (2019).
[449] M. Crisostomi, M. Lewandowski, and F. Vernizzi, Phys. Rev. D **100**, 024025 (2019).
[450] K.-i. Maeda, Phys. Rev. D **39**, 3159 (1989).
[451] S. Weinberg, Phys. Rev. D **77**, 123541 (2008) [arXiv:0804.4291 [hep-th]] [Search INSPIRE].
[452] C. de Rham, G. Gabadadze, and A. J. Tolley, Phys. Rev. Lett. **106**, 231101 (2011) [arXiv:1011.1232 [hep-th]] [Search INSPIRE].
[453] H. van Dam and M. Veltman, Nucl. Phys. B **22**, 397 (1970).
[454] V. I. Zakharov, JETP Lett. **12**, 312 (1970) [Pisma Zh. Eksp. Teor. Fiz. **12**, 447 (1970).
[455] A. I. Vainshtein, Phys. Lett. B **39**, 393 (1972).
[456] S. F. Hassan and R. A. Rosen, J. High Energy Phys. **1202**, 126 (2012) [arXiv:1109.3515 [hep-th]] [Search INSPIRE].
[457] A. De Felice, T. Nakamura, and T Tanaka, Prog. Theor. Exp. Phys. **2014**, 043E01 (2014) [arXiv:1304.3920 [gr-qc]] [Search INSPIRE].
[458] T. Jacobson and D. Mattingly, Phys. Rev. D **64**, 024028 (2001).
[459] T. Jacobson, PoS **QG-Ph**, 020 (2007).
[460] S. M. Carroll and E.A. Lim, Phys. Rev. D **70**, 123525 (2004).

[461] J. W. Elliott, G. D. Moore, and H. Stoica, J. High Energy Phys. **0508**, 066 (2005).
[462] C. M. Will, Liv. Rev. Rel. **17**, 4 (2014).
[463] R. E. Rutledge, D. W. Fox, S. R. Kulkarni, B. A. Jacoby, I. Cognard, D. C. Backer, and S. S. Murry, Astrophys. J. **613**, 522 (2004).
[464] M. Bailes, S. Johnston, J. F. Bell, B. W. Lorimer, D. R. Stappers, R. N. Manchester, A. G. Lyne, L. Nicastro, N. D'Amico, and B. M. Gaensler, Astrophys. J. **481**, 386 (1997).
[465] L. Shao and N. Wex, Class. Quantum Grav. **29**, 215018 (2012).
[466] L. Shao, R. N. Caballero, M. Kramer, N. Wex, D. J. Champion, and A. Jessner, Class. Quantum Grav. **30**, 165019 (2013).
[467] T. Damour and G. Esposito-Farése, Phys. Rev. D **46**, 4128 (1992).
[468] K. Yagi, D. Blas, E. Barausse, and N. Yunes, Phys. Rev. D **89**, 084067 (2014); **90**, 069902 (2014); **90**, 069901 (2014) [errata].
[469] A. E. Gümrükçüoğlu, M. Saravani, and T. P. Sotiriou, Phys. Rev. D **97**, 024032 (2018).
[470] J. Oost, S. Mukohyama, and A. Wang, Phys. Rev. D **97**, 124023 (2018).
[471] L. Sampson, N. Cornish, and N. Yunes, Phys. Rev. D **89**, 064037 (2014) [arXiv:1311.4898 [gr-qc]] [Search INSPIRE].
[472] L. Sampson, N. Yunes, N. Cornish, M. Ponce, E. Barausse, A. Klein, C. Palenzuela, and L. Lehner, Phys. Rev. D **90**, 124091 (2014) [arXiv:1407.7038 [gr-qc]] [Search INSPIRE].
[473] F. M. Ramazanoğlu and F. Pretorius, Phys. Rev. D **93**, 064005 (2016) [arXiv:1601.07475 [gr-qc]] [Search INSPIRE].
[474] J. Antoniadis et al., Science **340**, 1233232 (2013) [arXiv:1304.6875 [astro-ph.HE]] [Search INSPIRE].
[475] A Arvanitaki, M. Baryakhtar, and X. Huang, Phys. Rev. D **91**, 084011 (2015) [arXiv:1411.2263 [hep-ph]] [Search INSPIRE].
[476] R. Brito, S. Ghosh, E. Barausse, E. Berti, V. Cardoso, I. Dvorkin, A. Klein, and P. Pani, Phys. Rev. D **96**, 064050 (2017) [arXiv:1706.06311 [gr-qc]] [Search INSPIRE].
[477] R. Narayan and J. E. McClintock, arXiv:1312.6698 [astro-ph.HE] [Search INSPIRE].
[478] K. Yamada, T. Narikawa, and T. Tanaka, Prog. Theor. Exp. Phys. **2019**, 103E01 (2019) [arXiv:1905.11859 [gr-qc]] [Search INSPIRE].
[479] K. Yagi, Phys. Rev. D **86**, 081504(R) (2012) [arXiv:1204.4524 [gr-qc]] [Search INSPIRE].
[480] LIGO/Virgo, Gravitational Wave Open Science Center (available at: https://www.gw-openscience.org/about/, date last accessed April 18, 2021).
[481] N. Yunes, K. Yagi, and F. Pretorius, Phys. Rev. D **94**, 084002 (2016) [arXiv:1603.08955 [gr-qc]] [Search INSPIRE].
[482] L. C. Stein and K. Yagi, Phys. Rev. D **89**, 044026 (2014) [arXiv:1310.6743 [gr-qc]] [Search INSPIRE].
[483] K. Prabhu and L. C. Stein, Phys. Rev. D **98**, 021503 (2018) [arXiv:1805.02668 [gr-qc]] [Search INSPIRE].
[484] K. Yagi, L. C. Stein, N. Yunes, and T. Tanaka, Phys. Rev. D **85**, 064022 (2012); **93**, 029902 (2016) [erratum] [arXiv:1110.5950 [gr-qc]] [Search INSPIRE].
[485] E. Berti, K. Yagi, and N. Yunes, Gen. Rel. Grav. **50**, 46 (2018) [arXiv:1801.03208 [gr-qc]] [Search INSPIRE].
[486] R. Nair, S. Perkins, H. O. Silva, and N. Yunes, Phys. Rev. Lett. **123**, 191101 (2019); **124**, 169904 (2020) [erratum] [arXiv:1905.00870 [gr-qc]] [Search INSPIRE].
[487] S. Tahura, K. Yagi, and Z. Carson, Phys. Rev. D **100**, 104001 (2019) [arXiv:1907.10059 [gr-qc]] [Search INSPIRE].
[488] Z. Carson, B. C. Seymour, and K. Yagi, Class. Quantum Grav. **37**, 065008 (2020) [arXiv:1907.03897 [gr-qc]] [Search INSPIRE].
[489] G. Gnocchi, A. Maselli, T. Abdelsalhin, N. Giacobbo, and M. Mapelli, Phys. Rev. D **100**, 064024 (2019) [arXiv:1905.13460 [gr-qc]] [Search INSPIRE].
[490] A. Nishizawa and T. Kobayashi, Phys. Rev. D **98**, 124018 (2018).
[491] M. Crisostomi, K. Noui, C. Charmousis, and D. Langlois, Phys. Rev. D **97**, 044034 (2018).
[492] A. De Felice, D. Langlois, S. Mukohyama, K. Noui, and A. Wang, Phys. Rev. D **98**, 084024 (2018).
[493] P. Creminelli, J. Gleyzes, J. Noreña, and F. Vernizzi, Phys. Rev. Lett. **113**, 231301 (2014).
[494] K. Yamada and T. Tanaka, Prog. Theor. Exp. Phys. **2020**, 093E01 (2020) [arXiv:2006.11086 [gr-qc]] [Search INSPIRE].
[495] K. Yagi and H. Yang, Phys. Rev. D **97**, 104018 (2018) [arXiv:1712.00682 [gr-qc]] [Search INSPIRE].

[496] V. Cardoso, E. Franzin, and P. Pani, Phys. Rev. Lett. **116**, 171101 (2016); **117**, 089902 (2016) [erratum].

[497] V. Cardoso, S. Hopper, C. F. B. Macedo, C. Palenzuela, and P. Pani, Phys. Rev. D **94**, 084031 (2016).

[498] L. Hui, D. Kabat, and S. S. C. Wong, J. Cosmol. Astropart. Phys. **1912**, 020 (020).

[499] J. Abedi, H. Dykaar, and N. Afshordi, Phys. Rev. D **96**, 082004 (2017).

[500] J. Westerweck, A. B. Nielsen, O. Fischer-Birnholtz, M. Cabero, C. Capano, T. Dent, B. Krishnan, G. Meadors, and A. H. Nitz, Phys. Rev. D **97**, 124037 (2018).

[501] A. B. Nielsen, C. D. Capano, O. Birnholtz, and J. Westerweck, Phys. Rev. D **99**, 104012 (2019).

[502] R. K. L. Lo, T. G. F. Li, and A. J. Weinstein, Phys. Rev. D **99**, 084052 (2019).

[503] H. Nakano, H. Sago, H. Tagoshi, and T. Tanaka, Prog. Theor. Exp. Phys. **2017**, 071E01 (2017).

[504] N. Uchikata, H. Nakano, T. Narikawa, N. Sago, H. Tagoshi, and T. Tanaka, Phys. Rev. D **100**, 062006 (2019).

[505] K. W. Tsang, M. Rollier, A. Ghosh, A. Samajdar, M. Agathos, K. Chatziioannou, V. Cardoso, G. Khanna, and C. Van Den Broeck, Phys. Rev. D **98**, 024023 (2018).

[506] K. W. Tsang, A. Ghosh, A. Samajdar, K. Chatziioannou, S. Mastrogiovanni, M. Agathos, and C. Van Den Broeck, Phys. Rev. D **101**, 064012 (2020).

[507] A. Testa and P. Pani, Phys. Rev. D **98**, 044018 (2018).

[508] E. Maggio, A. Testa, S. Bhagwat, and P. Pani, Phys. Rev. D **100**, 064056 (2019).

[509] V. Cardoso and P. Pani, Liv. Rev. Rel. **22**, 4 (2019).

[510] D. J. E. Marsh, Phys. Rep. **643**, 1 (2016).

[511] D. Yoshida and J. Soda, Prog. Theor. Exp. Phys. **2018**, 041E01 (2018).

[512] D. Yoshida and J. Soda, Int. J. Mod. Phys. D **27**, 1850096 (2018).

[513] J. Soda and D. Yoshida, Galaxies **5**, 96 (2017).

[514] Y. Ali-Haïmoud and Y. Chen, Phys. Rev. D **84**, 124033 (2011).

[515] B. Carr, K. Kohri, Y. Sendouda, and J. Yokoyama, arXiv:2002.12778 [astro-ph.CO] [Search INSPIRE].

[516] T. Nakamura, M. Sasaki, T. Tanaka, and K. S. Thorne, Astrophys. J. Lett. **487**, L139 (1997)

[517] B. P. Abbott et al. [LIGO Scientific and Virgo Collaborations], Phys. Rev. Lett. **123**, 161102 (2019) [arXiv:1904.08976 [astro-ph.CO]] [Search INSPIRE].

[518] T. Nakamura et al., Prog. Theor. Exp. Phys. **2016**, 093E01 (2016).

[519] B. Kocsis, T. Suyama, T. Tanaka, and S. Yokoyama, Astrophys. J. **854**, 41 (2018).

[520] J. Garriga and N. Triantafyllou, J. Cosmol. Astropart. Phys. **1909**, 043 (2019).

[521] S. Bird, I. Cholis, J. B. Muñoz, Y. Ali-Haïmoud, M. Kamionkowski, E. D. Kovetz, A. Raccanelli, and A. G. Riess, Phys. Rev. Lett. **116**, 201301 (2016).

[522] R. M. O'Leary, Y. Meiron, and B. Kocsis, Astrophys. J. Lett. **824**, L12 (2016).

[523] L. Gondán, B. Kocsis, P. Raffai, and Z. Frei, Astrophys. J. **860**, 5 (2018).

[524] A. D. Gow, C. T. Byrnes, A. Hall, and J. A. Peacock, J. Cosmol. Astropart. Phys. **2001**, 031 (2020).

[525] T. Chiba and S. Yokoyama, Prog. Theor. Exp. Phys. **2017**, 083E01 (2017).

[526] M. Mirbabayi, A. Gruzinov, and J. Noreña, J. Cosmol. Astropart. Phys. **2003**, 017 (2020).

[527] V. De Luca, V. Desjacques, G. Franciolini, A. Malhotra, and A. Riotto, J. Cosmol. Astropart. Phys. **1905**, 018 (2019).

[528] M. He and T. Suyama, Phys. Rev. D **100**, 063520 (2019).

[529] T. Harada, C.-M. Yoo, K. Kohri, and K. I. Nakao, Phys. Rev. D **96**, 083517 (2017); **99**, 069904 (2019) [erratum].

[530] S. Wang, T. Terada, and K. Kohri, Phys. Rev. D **99**, 103531 (2019); **101**, 069901 (2020) [erratum].

[531] M. Sasaki, T. Suyama, T. Tanaka, and S. Yokoyama, Phys. Rev. Lett. **117**, 061101 (2016); **121**, 059901 (2018) [erratum].

[532] S. Wang, Y.-F. Wang, Q.-G. Huang, and T. G. F. Li, Phys. Rev. Lett. **120**, 191102 (2018).

[533] P. Ajith et al., Phys. Rev. Lett. **106**, 241101 (2011).

[534] P. Ajith et al., Phys. Rev. D **77**, 104017 (2008); **79**, 129901 (2009) [erratum].

[535] B. J. Carr, K. Kohri, Y. Sendouda, and J. Yokoyama, Phys. Rev. D **81**, 104019 (2010).